Universidade de São Paulo
Instituto de Geociências

Paramirim Aulacogen: finite strain analysis and tectonic shortening, implications for the São Francisco craton evolution and its marginal orogens

Raulindo Santana Silva Veloso

Dissertação apresentada ao Programa Geoquímica e Geotectônica para obtenção do título de Mestre em Ciências.

Área de concentração: Geotectônica

Orientador: Prof. Dr. Ginaldo Ademar da Cruz Campanha

São Paulo

2023

UNIVERSIDADE DE SÃO PAULO
INSTITUTO DE GEOCIÊNCIAS

Paramirim Aulacogen: finite strain analysis and tectonic shortening, implications for the São Francisco craton evolution and its marginal orogens

RAULINDO SANTANA SILVA VELOSO

Orientador: Prof. Dr. Ginaldo Ademar da Cruz Campanha

Dissertação de Mestrado

Nº 908

COMISSÃO JULGADORA

Dr. Ginaldo Ademar da Cruz Campanha

Dr. Guilherme Knauer

Dra. Geane Carolina Gonçalves Cavalcante

SÃO PAULO
2023

AGRADECIMENTOS

Também quero agradecer ao meu mestre de capoeira, Tio João, e ao nosso grupo Arte e Ginga, por me acolherem tão bem no início da minha prática. Agradeço aos meus colegas de treino e de roda, pelos momentos de aprendizado e empenho.

Laroyê, Èṣù!

RESUMO

Esta dissertação apresenta novas descobertas e investiga questões sobre a Geologia Estrutural da região do aulacógeno de Paramirim. A área de estudo é compreendida como um sistema de riftes intracontinentais desenvolvidos no cráton do São Francisco a partir do período estateriano e que inclui rochas sedimentares do Paleoproterozoico ao Neoproterozoico dos Supergrupos Espinhaço e São Francisco. Durante o ciclo orogênico Brasiliano, esse sistema de riftes e bacias sedimentares sofreu inversão tectônica, resultando no desenvolvimento de dois principais *fold-and-thrust belts* com vergências tectônicas opostas: a Serra do Espinhaço Setentrional e a Chapada Diamantina Ocidental. O estudo inclui a quantificação da deformação finita, modelagem de matrizes de deformação, modelagem geológica cinemática e estimativas do encurtamento tectônico para a área. Os resultados estimam um encurtamento tectônico para a Chapada Diamantina Ocidental de $17.0\% - 19.4\%$ e para a Serra do Espinhaço Setentrional de $13.5\% - 16.3\%$. Considerando os valores obtidos da relação X/Z dos elipsoides de deformação finita, ambos *fold-and-thrust belts* foram submetidos a uma magnitude similar de deformação. No entanto, as áreas se diferenciam quanto ao regime de deformação, orientação axial e forma dos elipsoides de deformação finita. A primeira exibe principalmente elipsoides oblados, enquanto a última apresenta elipsoides de forma prolata. O domínio da Chapada Diamantina Ocidental é caracterizado por um regime de empurrões e dobras associadas, enquanto a Serra do Espinhaço Setentrional exibe uma combinação de empurrões, dobras e tectônica transcorrente, com ocorrência de partição de deformação. Além disso, as estimativas de encurtamento tectônico para a área destacam a natureza da região como uma zona de deformação neoproterozoica, o que suporta a hipótese de uma zona de não rigidez entre os segmentos ocidentais e orientais do cráton do São Francisco.

Palavras-chave: aulacógeno de Paramirim, encurtamento tectônico, deformação finita, partição de deformação, cráton do São Francisco

ABSTRACT

This dissertation presents new findings and investigates issues regarding the Structural Geology of the Paramirim aulacogen region. The study area is understood as a system of intracontinental rifts developed in the São Francisco craton from the Statherian period onwards and includes Paleoproterozoic to Neoproterozoic metasedimentary rocks from the Espinhaço and São Francisco Supergroups. During the Brasiliano orogenic cycle, this system of rifts and sedimentary basins underwent tectonic inversion resulting in the development of two main fold-and-thrust belts with opposite tectonic vergences: the Northern Espinhaço Range and the Western Chapada Diamantina. The study includes quantification of finite deformation, modeling of deformation matrices, kinematic forward modeling and estimates of tectonic shortening for the area. The results estimate a tectonic shortening for the Western Chapada Diamantina of $17.0\% - 19.4\%$, and for the Northern Espinhaço Range of $13.5\% - 16.3\%$. Based on the finite strain ellipsoids X/Z ratios, both fold-and-thrust belts were subjected to a similar strain magnitude. However, the areas differ in their deformation regime, axial orientation and shape of the finite strain ellipsoids. The former displays mostly oblate ellipsoids, while the latter exhibits prolate-shaped ellipsoids. The Western Chapada Diamantina domain is compatible with a thrust regime and associated folding, while the Northern Espinhaço Range shows a combination of thrust and strike-slip tectonics, with the occurrence of strain partitioning. Furthermore, a numeric deformation matrix simulation suggests that a combination of sedimentary compaction followed by a thrust and strike-slip regime could explain the strain patterns obtained. Moreover, the estimates of tectonic shortening for the area highlight the nature of the region as a Neoproterozoic deformation zone, supporting the hypothesis of a zone of non-rigidity between the western and eastern segments of the São Francisco craton.

Keywords: Paramirim aulacogen, tectonic shortening, finite strain, strain partitioning, São Francisco craton

SUMÁRIO

DISSERTATION STRUCTURE OVERVIEW

This present masters dissertation is a comparative study, between the Northern Espinhaço Range and Western Chapada Diamantina fold-and-thrust belts, based on the quantification of the deformation suffered in the Paramirim aulacogen, by evaluating the computed finite strain ellipsoids for the region and by estimating the minimum tectonic shortening experienced by the area. In order to achieve these goals several analyses were carried, such as:

i. Evaluation of open access and collected structural field data;

ii. Recognition and description of structures and kinematics of the Paramirim aulacogen, from field-based and petrographic observations;

iii. Quantification of the finite strain using single quartz grains as strain markers;

iv. Construction of kinematic forward models to test different deformation scenarios and to validate possible interpretations.

After conducting research on the tectonic processes in the Western Chapada Diamantina region during my scientific initiation, which resulted in a paper published at the beginning of my M.Sc course (Silva Neto et al., 2022, included in the supplementary material), it was deemed necessary to expand the research area to also encompass the domain of the Northern Espinhaço Range, in order to assess and estimate the tectonic shortening for the Paramirim aulacogen region. Therefore, unprecedented finite strain ellipsoids and kinematic forward models are presented allowing comparison between these two geological domains within the Paramirim aulacogen.

Ultimately, this project allowed us to test deformation scenarios and validate possible interpretations. Future debates regarding tectonic evolutionary models for the region, could benefit from our findings.

1 INTRODUCTION

The Paramirim aulacogen corresponds to an intracontinental rift system located in the northern sector of the São Francisco craton. After the Statherian age rifting onset, the region developed an extensive sedimentary basin system, where Mesoproterozoic to Neoproterozoic thick sedimentary successions of siliciclastic and carbonate rocks, represented by the Espinhaço and São Francisco Supergroups, were deposited (Cruz & Alkmim, 2006, 2017; Pedrosa-Soares & Alkmim, 2011; Danderfer et al., 2009; Alkmim et al., 2001; Guimarães et al., 2005).

As a result of the Brasiliano orogenic cycle, this ancient sedimentary basin system experienced intracratonic deformation, as stress propagated from marginal belts into the craton interior in an inversion tectonics process, during the assembly of West Gondwana (Campos Neto, 2000; Almeida et al., 2000; Alkmim et al., 2006, 2001; Cruz & Alkmim, 2006). This event ultimately led to the formation of two major fold-and-thrust belts with opposite tectonic vergences, namely the Northern Espinhaço Range (NER) and the Western Chapada Diamantina (WCD), in the Paramirim corridor, where the effects of inversion tectonics are most pronounced in the aulacogen (Cruz & Alkmim, 2006, 2017; Cruz et al., 2015; Guimarães et al., 2019).

The regional geological context of the study area has been subject of debate, particularly regarding the oceanic or intracontinental nature of neighboring marginal orogens, such as the Araçuaí-West Congo Orogen (AWCO), and the integrity of the São Francisco craton (Fossen et al., 2020; Cavalcante et al., 2019; Cruz & Alkmim, 2006; Pedrosa-Soares et al., 2001; Alkmim et al., 2006; Konopásek et al., 2020; Meira et al., 2015, 2019).

The "nutcracker" model proposes that the aulacogens of the São Francisco craton, played a crucial role in accommodating rotational and translational movements associated with the Araçuaí-West Congo Orogen (AWCO) building process (Alkmim et al., 2006). Even more, the Paramirim aulacogen could represent the continental terminal portion of a V-shaped or scissor-shaped oceanic basin, which formed the foundation for the AWCO orogenic system (Caxito et al., 2022; François et al., 2022).

Despite numerous studies on the tectonic and geochronological evolution of the Paramirim aulacogen, quantitative knowledge of the magnitude and kinematics of deformation, as well as

the geometric implications for the internal mobility of the São Francisco craton, remains limited. Therefore, it is crucial to estimate the deformation and shortening that occurred in the region and to propose viable geometrical models.

This manuscript begins with a brief description of the geological settings surrounding the study area, followed by a explanation of the methodology used in the research. It then presents the results of the study and discusses their potential implications for evolutionary models of the São Francisco craton. The findings of this research may potentially contribute to future discussions about tectonic evolution models for the region.

2 OBJECTIVES

This study quantifies and compares the deformation of the Paramirim aulacogen in the Northern Espinhaço Range and Western Chapada Diamantina fold-and-thrust belts. The research evaluates the computed finite strain for the region and estimate the minimum tectonic shortening experienced by the area. To achieve these objectives, various analyses were conducted, such as evaluating open access and collected structural field data, recognizing and describing structures and kinematics of the Paramirim aulacogen, quantifying finite strain ellipsoids using single quartz grains as strain markers, numeric deformation matrix simulation and constructing kinematic models to test different deformation scenarios and validate previous interpretations.

The present research aims to enhance comprehension of the role played by the Paramirim aulacogen in accommodating deformation during Gondwana assembly. Unprecedented finite strain ellipsoids and kinematic forward models are presented in this work, enabling a comparison between the Western Chapada Diamantina and Northern Espinhaço Range fold-and-thrust belts. The goal of this research is to verify deformation scenarios and validate initial interpretations, leading to propose viable structural models that could represent the Paramirim corridor's geometry and kinematics.

3   GEOLOGICAL SETTINGS

The São Francisco craton (SFC) is a major continental block preserved during the Neoproterozoic Pan-African-Brasiliano orogeny (Almeida, 1977). The craton has a counterpart in Africa, and together they formed the São Francisco-Congo paleoplate, which assembled during Rhyacian-Orosirian accretionary processes (ca. 2.05 Ga) (Brito Neves et al., 1999, 1995). Therefore, the SFC's basement includes Archean and Paleoproterozoic (Siderian to Orosirian) continental fragments, mainly composed of medium to high grade metamorphic rocks such as TTG suites, associated granite-greenstone belts, K-rich metagranitoids, and orthogneisses (Teixeira et al. 2017 and all references therein).

The Paramirim aulacogen is recognized as an intracontinental rift system that originated in the central region of the São Francisco-Congo craton during the Statherian period (Pedrosa-Soares et al., 2001) (Figure 1). This rift system provided a space for sedimentary basin processes, which spanned from the Paleoproterozoic to the Neoproterozoic (Schobbenhaus, 1996). The sedimentary rocks of the Espinhaço Supergroup, consisting mainly of siliciclastics and metavolcanics, are deposited in this rift system and are overlaid by a package of glaciomarine sediments, carbonates and siliciclastic rocks intercalation from the São Francisco Supergroup (Cruz & Alkmim, 2017).

After the deposition of the major sedimentary units in the Paramirim aulacogen, the region experienced a positive tectonic inversion during the Brasiliano-Pan African orogenic cycle, involving the propagation of orogenic fronts from the marginal belts towards the interior of the craton (Alkmim et al., 2001, 2006; Cruz & Alkmim, 2006). This event ultimately led to the formation of two significant fold-and-thrust belts with opposite tectonic vergences, namely the Northern Espinhaço Range (NER) and Western Chapada Diamantina (WCD), which exhibit a combination of thick and thin-skinned structural styles (Cruz & Alkmim, 2006, 2017; Guimarães et al., 2005). The Paramirim corridor is bounded at east by the Barra do Mendes-João Correia lineament and it comprises these two marginal and oppositely verging fold-and-thrust belts with a central metamorphic high-grade uplifted block, known as the Paramirim valley (Figure 1).
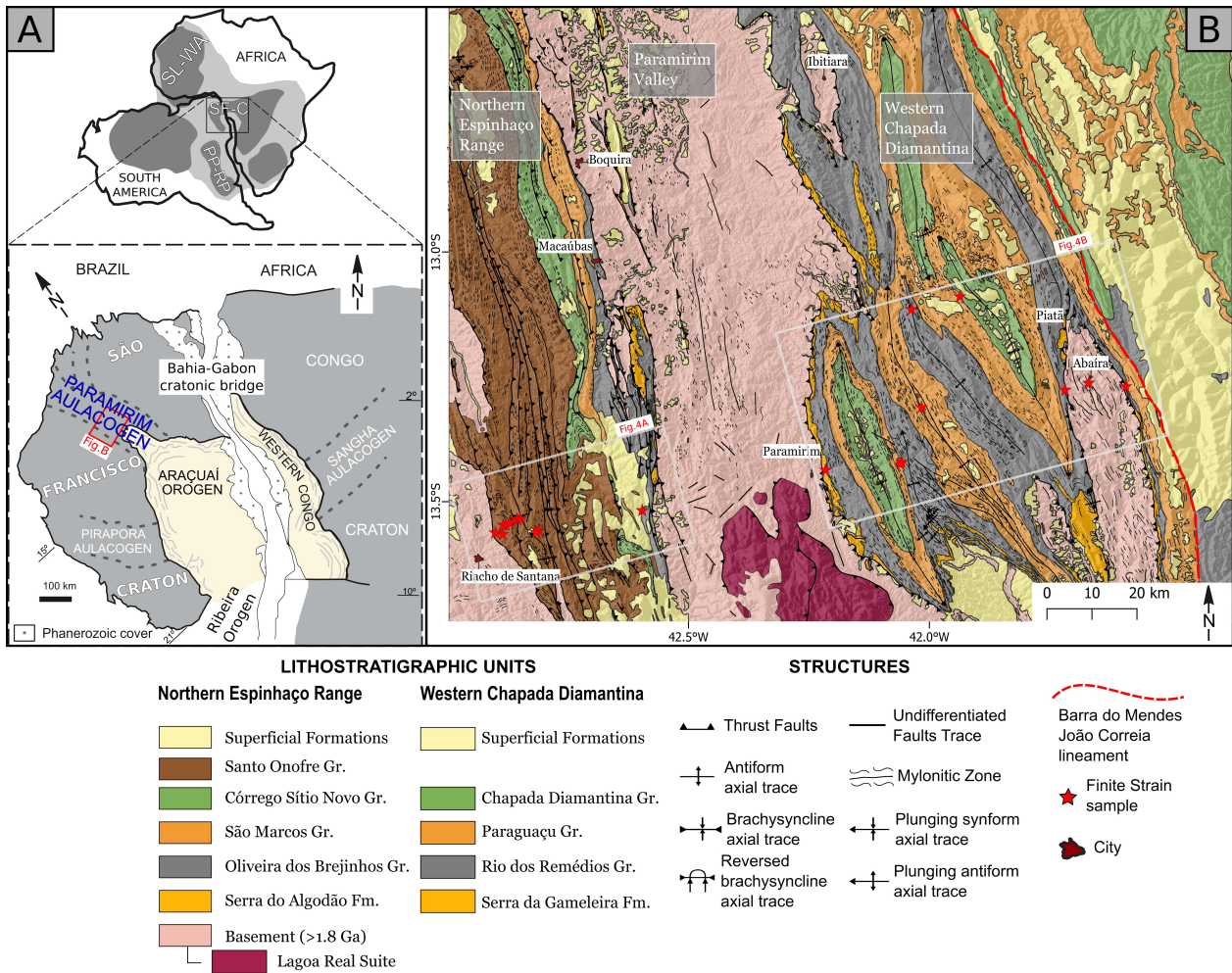
Figure 1: A: The tectonic position of the Paramirim aulacogen within the São Francisco-Congo craton and the adjacent Araçuaí-West Congo Orogen. Modified from Pedrosa-Soares et al. (2008); **B:** Simplified geological map of the Paramirim corridor, area of maximum tectonic inversion within the Paramirim aulacogen, including the Western Chapada Diamantina and Northern Espinhaço fold-and-thrust belts (after Guimarães et al. 2005, 2019; Arcanjo et al. 2000; Cruz et al. 2008).

3.1 *Stratigraphy*

During its evolutionary history, the São Francisco experienced numerous rifting episodes, leading to the formation of several sedimentary basins (Brito Neves et al., 1995). The Paramirim Aulacogen developed from a series of diachronous intracratonic basins, with ages spanning the Paleoproterozoic and Neoproterozoic (Figure 2) (Guimarães et al., 2019). During the Neoproterozoic, the two sub-basins of the Northern Espinhaço and Chapada Diamantina were converted into homonymous

fold-and-thrust belts after tectonic inversion phase (Schobbenhaus, 1996; Danderfer & Dardenne, 2002; Cruz & Alkmim, 2006, 2017).

The Espinhaço Supergroup is the main filling unit in the Western Chapada Diamantina region. It is a sequence of Paleoproterozoic (Statherian) to Mesoproterozoic siliciclastic rocks, including metasandstones, metaconglomerates, and metapelites, embedded with layers of volcanic and intrusive rocks. It is divided into three groups, ordered from bottom to top as the Rio dos Remédios, Paraguaçu, and the Chapada Diamantina homonymous group (Guimarães et al., 2005).

The Serra da Gameleira Formation is the bottommost layer of the sedimentary sequence, which is associated to a pre-rift sedimentation phase. It comprises aeolian sandstones and is situated above the basement, whose contact is characterized by a regional erosive and angular unconformity (Guimarães et al., 2005).

The pre-rift unit is overlaid by the Rio dos Remédios group, which is composed of a series of siliciclastic and epiclastic units such as sandstone, metapelites, and metaconglomerates. It records both mechanical and thermal subsidence events that occurred in the basin during the syn-rift phase (Guimarães et al., 2005). The Paraguaçu Group comprises shallow marine sediments and pelites and rests upon the lower Rio dos Remédios Group with an erosional or tectonic unconformity. This group marks a transition from tectonic influence to a passive subsidence sedimentation pattern, and is typically associated with a post-rift sag sequence during a phase of basin expansion (Guimarães et al., 2005; Loureiro et al., 2009; Cruz & Alkmim, 2017). Finally at the top, the Chapada Diamantina Group has a sag geometry that closely resembles the post-rift Paraguaçu Group. It is characterized by a shift from marine to continental sedimentation, which is marked by an erosive unconformity. This group consists of a sequence of fluvial and shallow marine sandstones, conglomerates, shallow marine pelites and with carbonate lenses (Guimarães et al., 2005; Cruz & Alkmim, 2017).

The Northern Espinhaço Range includes the Espinhaço Supergroup and the Tonian Santo Onofre Group. The NER exhibits distinct nomenclature for the units of the Espinhaço Supergroup in comparison to the Western Chapada Diamantina, but despite this variation, sedimentary similarities between the two domains have been recognized (Guimarães et al., 2019; Schobbenhaus, 1996;

6

Danderfer & Dardenne, 2002; Alkmim & Martins-Neto, 2012; Guadagnin & Chemale Jr, 2015; Cruz & Alkmim, 2017). The NER region comprises Paleoproterozoic to Neoproterozoic siliciclastic rocks, coupled with intrusive and volcanic bodies. The Espinhaço Supergroup stratigraphic package is subdivided into four groups, from bottom to top, namely Oliveira dos Brejinhos, São Marcos and Córrego do Sítio Novo, covered by the Santo Onofre Group (Guimarães et al., 2019) (Figure 2).
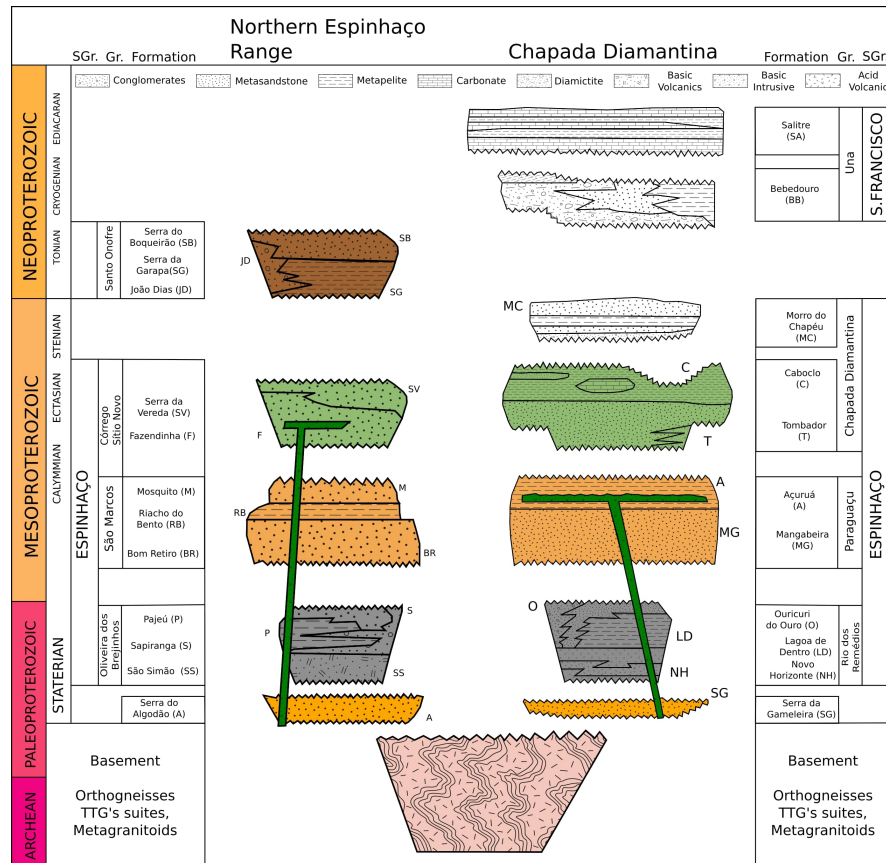
Figure 2: Stratigraphic chart of the Northern Espinhaço Range and the Western Chapada Diamantin. Based from Alkmim & Martins-Neto (2012), modified after Cruz & Alkmim (2017); Guimarães et al. (2005, 2019). The colors match the same color code by group of Figure 1.

The lowermost layer of the sedimentary sequence is the Serra do Algodão Formation, which is composed of pre-rift siliciclastic sediments (Guimarães et al., 2019). This layer is overlaid by the syn-rift Oliveira dos Brejinhos Group, which contains continental deposits interbedded with volcanic rocks. These volcanic rocks have been dated to a range of 1731 ± 5 Ma to 1775 ± 3 Ma, consistent with the statherian rifting onset age seen in other regions (Danderfer et al., 2009; Guadagnin & Chemale Jr, 2015; Danderfer Filho et al., 2015; Guimarães et al., 2019; Cruz et al., 2023).

It is followed upwards by the Mesoproterozoic eolian and shallow marine deposits of the São Marcos group, interpreted as the post-rift phase (Guimarães et al., 2019). On top of that, there is the 1500-1300 Ma sag sequence of the Córrego do Sítio Novo Group. Finally the tonian Santo Onofre Group (1000-720 Ma), which is interpreted as a superimposed rift, is the topmost unit of the approximately 9.000 meters thick sedimentary package (Bitencourt et al., 2019; Guimarães et al., 2019).

3.2 *Structural framework*

The Paramirim aulacogen structural framework comprises two primary fabric elements resulting from original extensional processes related to rifting and contractional structures associated with the basin inversion (Danderfer Filho, 1990; Cruz & Alkmim, 2006; Cruz et al., 2015).

The Northern Espinhaço Range and Western Chapada Diamantina fold-and-thrust belts together form a prominent and complex approximately 200 km wide NW-SE oriented double-vergent structural feature, resembling intracratonic orogen settings, which have been the subject of much research and investigation. The double-verging structure is due to the frontal movements directed towards ENE in the Western Chapada Diamantina and WSW-directed movements in the Northern Espinhaço (Guimarães et al., 2019; Cruz & Alkmim, 2017).

The main tectonic structures of the region consist of a collection of ductile and ductile-brittle shear zones, faulting and folding, developed during the collisional phase of the Brasiliano orogeny, where the stresses were propagated from marginal belts towards the craton interior (Cruz & Alkmim, 2006, 2017; Guimarães et al., 2019).

In the Western Chapada Diamantina region, it has been proposed that the structural inheritance features, related to the extensional phase of rift formation, were reactivated during the inversion phase. This reactivation controlled the localization of thrust ramps and exerted significant influence on the deformation of the sedimentary cover (Cruz & Alkmim, 2006; Cruz et al., 2015; D'Angelo et al., 2019; Guimarães et al., 2019; Silva Neto et al., 2022).

4 METHODOLOGY

4.1 *Database*

The dataset utilized in this study comprises field data and oriented samples collected from sections nearly orthogonal to the regional structures, along with published and unpublished structural data obtained from fieldwork and regional geological mapping conducted by the Geological Survey Company of State of Bahia (Companhia Baiana de Pesquisa Mineral - CBPM) and the Brazilian Geological Survey (CPRM), as well our own field data and oriented samples. Surface geometries are based on 1:200.000 and 1:100.000 scale geological maps of the Paramirim aulacogen region, as well as on a Digital Terrain Model derived from 30 m resolution SRTM images (USGS/NASA). As no seismic lines or boreholes are present within the study area, subsurface interpretation is constrained solely by kinematic forward models and surface geometrical relationships.

4.2 *Finite strain analysis*

This study conducted strain analysis on ten oriented samples of quartz grains-rich sandstones and siltstones in the Northern Espinhaço Range region and integrates with nine analysis previously carried out in the Western Chapada Diamantina region. Shape preferred orientation (SPO) analysis was carried out on each sample, using the Inertia Tensor Method (Launeau & Cruden, 1998), to analyze the orientation, shape and distribution of strain markers (quartz grains).

The methodology involves generating SPO ellipses for each individual grain in three or more non parallel sections of a sample and for each sample section by stacking all individual SPOs of the grain population on their gravity center (Launeau & Cruden, 1998). This analysis entails translating a subset window of 1/4 of the image of each sample section to nine different positions with a 50% overlap, which generates nine SPO subsets per image. The standard deviation between SPO subsets was then calculated for all parameters to evaluate the homogeneity of the data across the entire image and will attest of their unbiased quality (Launeau & Robin, 2005; Serra, 1982).

The software ELLIPSOID was used to determine the best-fit 3D ellipsoid for each sample based on the sectional ellipse data obtained (Robin, 2002; Launeau & Robin, 2005). The incompatibility

index parameter ($\sqrt{\tilde{F}}$) expresses the difference between the measured ellipses of any faces, with lower values indicating better fits (Robin, 2002). To test the invariance by translation, the given nine SPO subsets per sample were combined to produce 729 (3^6) finite strain ellipsoids for each location. For all parameters, 2σ is adopted as an estimation of the 95% confidence interval.

It is noteworthy that the tensor calculated characterizes only the object shape and may not correspond to the finite strain ellipsoid. However, when analyzing deformed objects that have an initial equidimensional geometry with spherical or elliptical shapes, such as quartz grains, and when there is no viscosity contrast between the clast and the matrix, the strain and shape ellipsoids can be considered equivalent (Launeau, 2004; Launeau & Robin, 2005; Faleiros, 2008). A more complete and detailed description of this methodology under the same application can be found in (Silva Neto et al., 2022).

4.3 *Strain integration*

Hossack (1978) proposed the strain integration technique, which involves calculating the undeformed length of a strain trajectory through integration of the reciprocal stretch along the trajectory in the current deformed state. This method is useful for estimating regional strain and determining the amount of shortening caused by penetrative strain (Woodward et al., 1986).

After determining the axial parameters of the ellipsoids as stretches (S), where $S = L/L_o$, being L_o the original undeformed length and L the final deformed length, the reciprocal stretch ($1/S$) is plotted against the distance (x) along a section crossing the ellipsoid's spatial distribution. The area under the resulting curve represents the original length (L_o):

$$L_o = \int_{x_1}^{x_2} \frac{1}{S}\,dx \tag{1}$$

The percentage of shortening in the section, represented by its elongation (e), can be obtained by comparing the original length (L_o) with the current deformed length (L):

$$e = \frac{L - L_o}{L_o} * 100 \tag{2}$$

10

4.4 *Forward modeling*

The limited availability of subsurface structural information in the study area poses challenges for accurately assessing its geometry and configuration. To overcome these limitations, we conducted kinematic forward modeling to incrementally simulate the geometry and structural evolution of the geological system, by applying well-established geometric principles that relate to stratigraphic units and faults (Vidal-Royo et al., 2022). By utilizing this approach, we can investigate geological models that are both kinematically and geometrically feasible. This also allows us to incorporate field-based observations and available surface information into our models, resulting in a more accurate representation of the subsurface geology.

The Simple Shear algorithm (White et al., 1986) was applied to simulate normal faulting during the extension phase and partial fault inversion in the forward models. In addition, the Trishear algorithm (Erslev, 1991) was utilized in the inversion phase to model compressional folding. In this study, we used the kinematic modeling algorithms available in the Petex MOVE™ suite (formerly Midland Valley MOVE) which allowed the construction of forward models.

4.5 *Finite strain matrix modeling*

In this study, we employed a deformation matrix modeling procedure to simulate the effects of a tectonic deformation superimposed over a diagenetic/compaction fabric in order to investigate the shape and orientation variation of the ellipsoids obtained (Ramsay & Lisle, 2000; Campanha, 2002; Moraes, 2016). This approach is similar to the one adopted by Ramsay & Wood (1973).

We utilized the Cauchy Deformation Tensor (Malvern, 1969; Means, 1978; Oertel, 1996) to calculate the strain ellipsoid parameters, after a sequence of deformational steps from initial uniaxial flattening followed by simple shear. A script in Python (3.8.10) was written in order to perform the calculations (available in the supplementary material).

Adopting a orthogonal cartesian coordinate system, we considered the x reference axis as East horizontal direction, the y reference axis as North horizontal direction, and the z reference axis as vertical down.

Initially, we modeled the initial sedimentary fabric using a uniaxial contraction matrix (UC), where the intensity of uniaxial contraction in the Z direction is indicated by the parameter $1/k$, meaning that higher values of $k > 1$ result in greater initial flattening.

$$UC = \begin{bmatrix} 1 & 0 & 0 \\ 0 & 1 & 0 \\ 0 & 0 & 1/k \end{bmatrix} \tag{3}$$

The tectonic superimposed deformation are represented by the simple shear matrices, defined as follows, where γ represents the shear strain, given by the tangent of the shear angle (ψ), i.e., $\gamma = tan(\psi)$.

$$SS_v = \begin{bmatrix} 1 & 0 & 0 \\ \gamma & 1 & 0 \\ 0 & 0 & 1 \end{bmatrix} \quad SS_h = \begin{bmatrix} 1 & 0 & \gamma \\ 0 & 1 & 0 \\ 0 & 0 & 1 \end{bmatrix} \tag{4}$$

To model a strike-slip deformation, we adopted a simple shear acting on a North-South vertical shear plane with a horizontal slip direction, represented by the SS_v matrix. Conversely, to model a thrust we adopted a simple shear acting on a horizontal shear plane with an East-West slip direction, represented by the SS_h matrix. Therefore, the final deformation matrix was calculated as the product of the initial uniaxial compressional matrix and either the SS_v or SS_h matrix, resulting in a final matrix F as follows:

$$F = UC \cdot SS_v \quad or \quad F = UC \cdot SS_h \tag{5}$$

To evaluate the finite strain matrix, we use the Cauchy deformation tensor (c), which is calculated by multiplying the transposed inverse matrix of F by the inverse matrix of F, as follows:

$$c = (F^{-1})^T * F^{-1} \tag{6}$$

The eigenvectors of $\boldsymbol{c}$ provide the orientations of the lines that make up the principal axes of deformation in the deformed state (finite strain), and their eigenvalues provide the reciprocal quadratic elongations (λ'_1, λ'_2, λ'_3) associated with these axes. It is important to note that $\lambda' = \frac{1}{\lambda} = \frac{1}{S^2}$, where S represents the stretch. Therefore, the finite strain ellipsoid axes can be expressed by its principal stretches by calculating $S = \sqrt{\frac{1}{\lambda'}}$. The calculations were done using Python scripts (available in the supplementary material).

5   RESULTS

5.1   *The study area*

Field work was carried out in the southwestern border of the Northern Espinhaço Range and samples were collected along a SW-NE section, at east of Riacho de Santana city (Figure 1B). In this region, the mountain range is composed of the metasedimentary units of the Espinhaço Supergroup and the Tonian Santo Onofre Group is the most prominent geomorphological feature.

The metasedimentary rocks in this area display well-preserved primary sedimentary structures. A slaty cleavage is developed, characterized by the alignment of sericite and elongation of clastic grains, which generally cuts through the bedding almost orthogonally, except near tectonic contacts with the basement, shear zones and faults, where structural parallelism is observed. This relationship is also observed in the Western Chapada Diamantina region (Guimarães et al., 2005; Silva Neto et al., 2022).

In the Northern Espinhaço range (NER), the study area consists of a set of transpressional shear zones that form an anastomosing network. Among the structural elements, the Santo Onofre Fault is one of the most significant, characterizing a sinistral shear zone oriented North-South that crosses the entire São Francisco craton, connecting the Rio Preto and Araçuaí belts (Guimarães et al., 2019; Danderfer Filho, 2000). Based on the geological maps used for this study and field observations, the region shows generally closed to isoclinal folds, almost always associated with axial-plane foliation manifested as a slaty cleavage (Guimarães et al., 2019; Teixeira, 2000).

For the NER region the sedimentary bedding poles delineate two clusters with moderate dips to ENE and WSW, reflecting the fold limbs and thus an interlimb angle of approximately 77 degrees. The calculated π-pole of 166/02 (trend/plunge) coincides with the intersection lineation data dispersion (Figure 3G). The mylonitic foliation and slaty cleavage poles dispersion indicate a more complex structural framework, suggesting refolding of these structures (Figure 3E-F). The stretching lineation data appears to form two distinct families: subhorizontal lineations with SSE-NNW trends and down dip lineations oriented towards NE (Figure 3H).
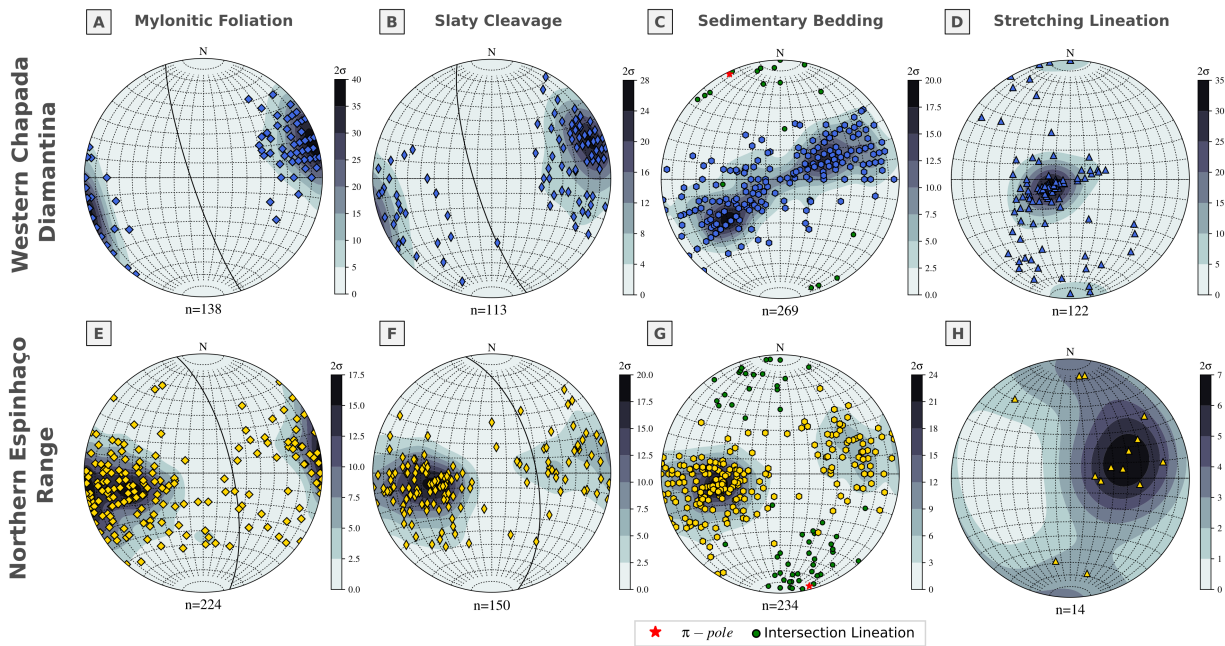
Figure 3: Structural data from the Western Chapada Diamantina and Northern Espinhaço fold-and-thrust belts (lower hemisphere, equal area projections).

On the contrary, the Western Chapada Diamantina region primary bedding poles demonstrate a great circle girdle that indicates open to gentle folding (Figure 3C). This is characterized by a sub-horizontal NE fold axis with two clusters of moderate dips to NE and SW that reflect the fold limbs. The π-pole axis calculated for this structure is 334/03 (trend/plunge), which coincides with the intersection lineation data clustering, indicating the main fold axis orientation. Figure 3A-B displays the tectonic foliation poles, which show a cluster with a mean upright attitude of NE strike and strong dip to SW. The stretching lineation is depicted in Figure 3D, with mean downdipping attitudes concerning the tectonic foliation.

While attitude data and kinematic indicators from the Northern Espinhaço corroborate the regional transport direction NE to SW, Western Chapada Diamantina stereograms suggest oposite sense of transport, from SW to NE. However, these two domains share similarities, as faults, fold upright axial-plane and SE-NW sub-horizontal fold axis. Ultimately, these data are consistent with the double vergence structural framework within which the study area is situated.

5.2 *Finite strain ellipsoids*

In this section, we present the results of finite strain distribution across the Northern Espinhaço Range and Western Chapada Diamantina fold-and-thrust belts. Data are reported in Table 1 and visually presented in Figure 4. To quantify the intensity of deformation in the 3D ellipsoids, we used the strain ratio (X/Z, major strain axis / minor strain axis). The supplementary material (Appendix) contains the complete raw data.

Table 1: Three dimesional strain data of best-fit ellipsoids. Axial attitudes are reported in the trend/plunge system, while XY planes follows the right-hand-rule convention (strike/dip, dipping to the right side of the observer).

Sample	XY Plane	Axes values			Axes attitudes			X/Z	X/Y	Y/Z	Flinn's k	$\sqrt{\bar{F}}$	Ellipsoids shape
		X	Y	Z	X	Y	Z						
NER-07	168/56	1.42	0.91	0.78	347/02	253/56	078/34	1.82	1.56	1.16	3.546	3.2	Prolate
NER-46	006/54	1.16	1.05	0.82	182/06	084/53	276/36	1.40	1.10	1.27	0.382	4.5	Oblate
NER-53	337/47	1.26	0.93	0.86	134/23	028/32	252/49	1.46	1.36	1.08	4.623	4.0	Prolate
NER-56	190/67	1.42	0.92	0.76	339/51	204/30	100/23	1.86	1.55	1.20	2.888	3.5	Prolate
NER-57	135/71	1.18	0.98	0.87	156/47	301/38	045/18	1.35	1.20	1.13	1.657	2.7	Prolate
NER-60	139/57	1.14	0.98	0.89	161/29	283/45	051/32	1.28	1.16	1.10	2.121	4.5	Prolate
NER-62	337/68	1.15	0.98	0.88	342/14	102/64	247/22	1.30	1.17	1.11	1.930	3.6	Prolate
NER-64	124/75	1.25	1.01	0.80	140/47	291/40	034/15	1.56	1.24	1.26	1.063	4.6	Prolate
NER-75B	169/62	1.22	0.96	0.85	178/17	296/56	078/29	1.43	1.27	1.13	2.182	3.2	Prolate
NER-79	356/53	1.23	0.97	0.84	169/08	069/51	266/38	1.46	1.26	1.16	1.803	4.5	Prolate
CD-01B	354/80	1.31	1.02	0.75	150/66	358/21	027/10	1.76	1.28	1.37	0.896	5.3	Oblate
CD-03A	308/62	1.23	1.05	0.77	099/43	329/35	218/27	1.60	1.17	1.37	0.455	7.6	Oblate
CD-06A	172/45	1.19	1.08	0.78	261/46	352/01	082/44	1.52	1.09	1.39	0.238	3.6	Oblate
CD-11	160/36	1.14	1.05	0.84	275/33	177/12	069/54	1.36	1.09	1.25	0.375	3.0	Oblate
CD-16	158/76	1.47	1.17	0.59	307/64	163/21	068/14	2.50	1.26	1.99	0.265	2.2	Oblate
CD-23	011/72	1.22	0.96	0.85	177/36	033/48	281/18	1.43	1.27	1.13	2.288	2.2	Prolate
CD-28	332/72	1.08	1.01	0.91	111/71	335/14	242/13	1.19	1.07	1.11	0.668	1.6	Oblate
CD-30A	129/69	1.09	1.05	0.88	294/33	154/49	039/21	1.24	1.04	1.20	0.203	2.5	Oblate
CD-40	359/65	1.12	1.00	0.90	156/39	021/41	268/25	1.25	1.11	1.12	0.982	3.3	Oblate

For the Northern Espinhaço Range, the strain ratio values (X/Z) obtained ranged from 1.28 to 1.86. The highest strain ratios (Samples NER-07, NER-56 and NER-64) fall on the westernmost part

of the study area, where sedimentary cover is thrusted over crystalline basement. Orange coloured samples, with intermediate strain ratios (X/Z) lie close to thrust faults crossing the middle portion and on the easternmost part of the study area, as represented by samples NER-46, NER-53, NER-75B and NER-79 (Figure 4). Samples NER-57, NER-60 and NER-62 display the lowest strain ratios (X/Z) forming a cluster lying among samples with intermediate to high strain ratios (Figure 4A).

In the WCD region, the strain ratio (X/Z) values obtained ranged from 1.190 to 2.504. Most of the highest strain ratios were found in samples from the eastern portion of the study area, which were either basement samples or located near shear zones that demarcate the boundary between basement and supracrustal rocks, which is the case of samples CD-01B, CD-03A and CD-06A. On the other hand, low to moderate strain magnitudes are scattered in the sedimentary cover, with the exception of sample CD-16 (Figure 4B).
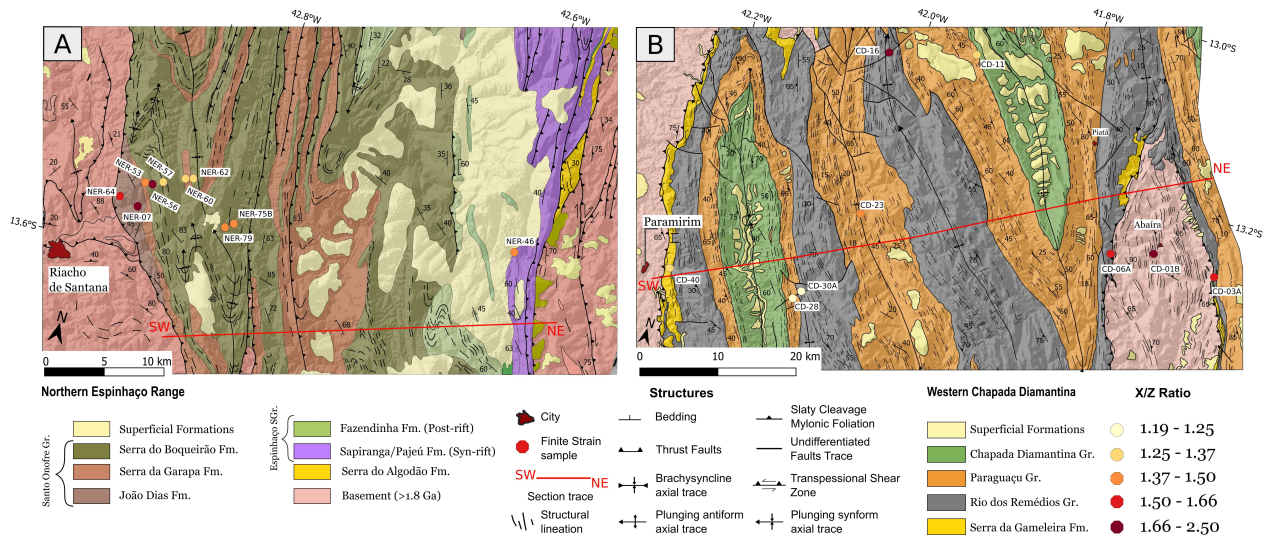

Figure 4: Finite strain samples distribution across the Northern Espinhaço (**A**) and Western Chapada Diamantina (**B**) fold-and-thrust belts. Samples are according to X/Z ratio values. Red line represents the section trace of forward models construction (Figures 10-11).

The majority of samples collected from the Northern Espinhaço Range and Western Chapada Diamantina fold-and-thrust belts comprise meta-sandstones and quartzites. Single quartz grains were used as strain markers for most samples, while a single meta-siltstone sample (CD-16) from the latter region was analyzed using mud-pellets as strain markers. Strain intensity measurements obtained from the CD-16 sample, which was collected from a more incompetent layer, may indicate

16

a higher degree of strain intensity in these layers. Conversely, strain intensity measurements obtained from competent layers were well constrained by other computed samples.

It is worth noting that the results presented in this study should be interpreted as a conservative estimate of the strain due to the limitations of the analytical techniques used. Specifically, the strain analysis focused primarily on metasandstones, which are generally more rheologically competent than metapelitic samples. As a result, the number of analyzed metapelitic samples was limited, which may have led to an underrepresentation of their contribution to the overall strain estimates. Despite these limitations, the results provide valuable information into the finite strain quantification for the study area.

5.3 *Ellipsoid axial parameters*

The axial orientations of the strain ellipsoid axes in the Western Chapada Diamantina region exhibit only slight variability in orientation for the Z and Y axes, while the X axes display a more dispersed pattern (Figure 5). The Z axes demonstrate a mean ENE sub-horizontal orientation that is consistent with a steep NNW flattening mean plane, and the Y axes exhibit a NNW sub-horizontal orientation. Although the X axes exhibit more variability, their mean orientation is oriented near down-dip regarding the mean flattening plane.

In contrast, samples from the Northern Espinhaço range exhibit a different orientation pattern for the X and Y axes, with the former displaying only slight variability, with a SSE-NNW sub-horizontal orientation, and the latter demonstrating a more scattered pattern, with a down-dipping WSW mean orientation. The Z axes exhibit very similar dispersion patterns to those from the Western Chapada Diamantina region, as shown in Figure 5. The Z-axial pattern retains the ENE sub-horizontal orientation, which is consistent with the NNW regional foliation plane.

In terms of ellipsoid shapes, the samples from the Western Chapada Diamantina fold-and-thrust belt are predominantly oblate, whereas those from the Northern Espinhaço Range region mostly display prolate shapes (Table 1 and Figure 6). It is worth noting that samples NER-46 and CD-23

are the only exceptions, with oblate and prolate shapes, respectively, which contradict samples from the same sampling area (Table 1).
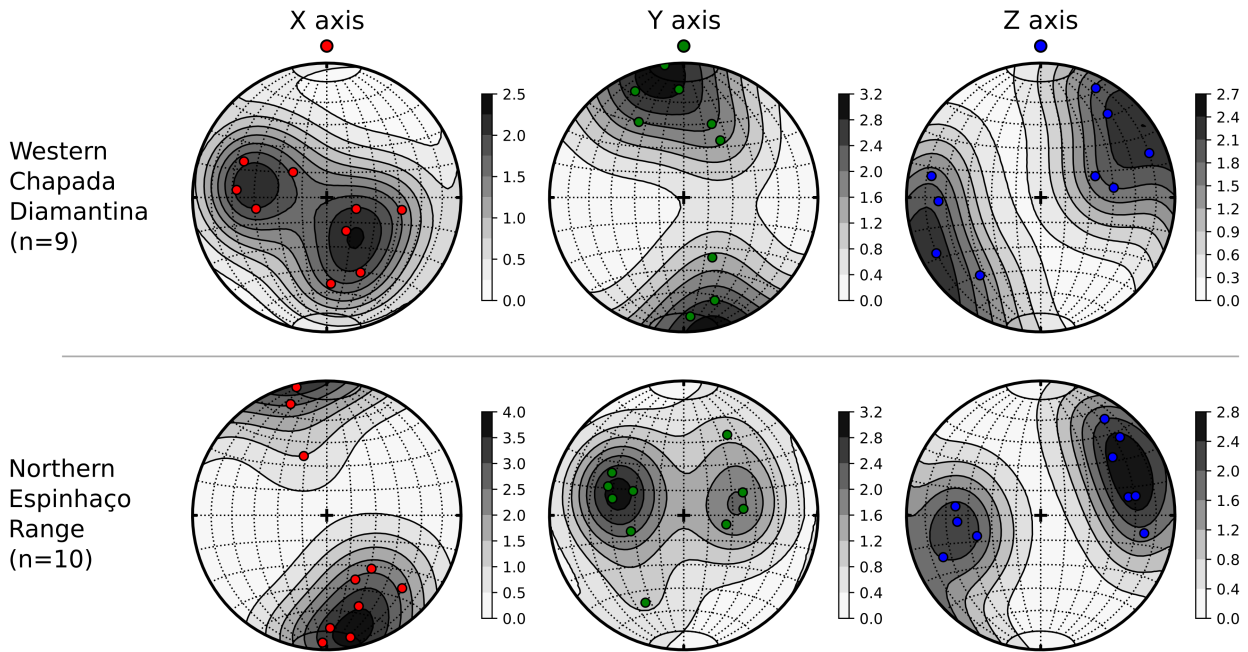

Figure 5: 3D finite strain ellipsoid X-, Y- and Z-axial orientations. Kamb contours are filled in gray scale at 2σ intervals. Low-hemisphere equal-area stereograms projection.
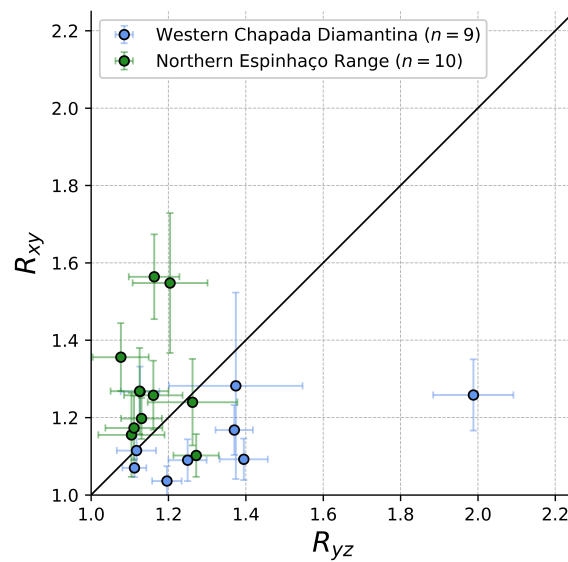

Figure 6: Flinn diagram representing the finite strain ellipsoid shape. Samples are colored according to spatial distribution. Error bars are computed from 95% confidence interval from axial lengths.

5.4 *Matrix modeling*

We conducted a deformation matrix modeling to understand how the shape of ellipsoids would vary under certain conditions. Specifically, we simulated the initial depositional fabric by an uniaxial vertical flattening, followed by deformation via simple shear in two different scenarios regarding the shear plane and slip direction orientation. This approach allowed us to investigate the evolution of strain ellipsoids in response to multiple and subsequent deformation events.

The modeling begins by creating six initial matrices with varying values of initial contraction $(1/k)$ ranging from 1 to 0.48 (k from 1 to 2.10). For each matrix, a deformational superimposed simple shear matrix is applied. The shear angles of the superimposed shear matrices are incremented in 10-degree steps, starting from 0 and ending at 80 degrees. The results regarded to the finite strain ellipsoid shapes were plotted as Flinn diagrams (Flinn, 1962) (Figs. 7 and 8) .

In order to simulate a North-South strike-slip regime, the simple shear matrix (SS_v) is used acting on a vertical North-South oriented shear plane, with a horizontal slip direction. The results of this modeling are presented in six plots in Figure 7, where each plot corresponds to a respective value of initial uniaxial compression $(1/k)$. For each plot, a simple shear matrix was imposed with increasing values of shear strain (γ), and from the final matrices representing the strain ellipsoid, the shape parameters were calculated.

When $1/k = 1$, which represents a scenario where the initial fabric is a perfect sphere (no sedimentary fabric), the imposition of a simple shear matrix results in an ellipsoid evolution path along the plane strain ($K_{Flinn} = 1$). For the subsequent scenarios, uniaxial flattening in the Z direction generates initial ellipsoids with an oblate shape. A stronger initial fabric is associated with a larger value of k (smaller $1/k$). The imposition of simple shear matrices causes changes in the final shape of the ellipsoid, which moves towards the prolate field with increasing values of shear strain (γ) (Figure 7).

Another scenario that was tested involves the superimposition of a simple shear matrix on a horizontal shear plane, with an East-West slip direction. Similarly, the simple shear matrix (SS_h) is applied to the initial uniaxial flattening matrices, simulating a thrust deformation regime. The results
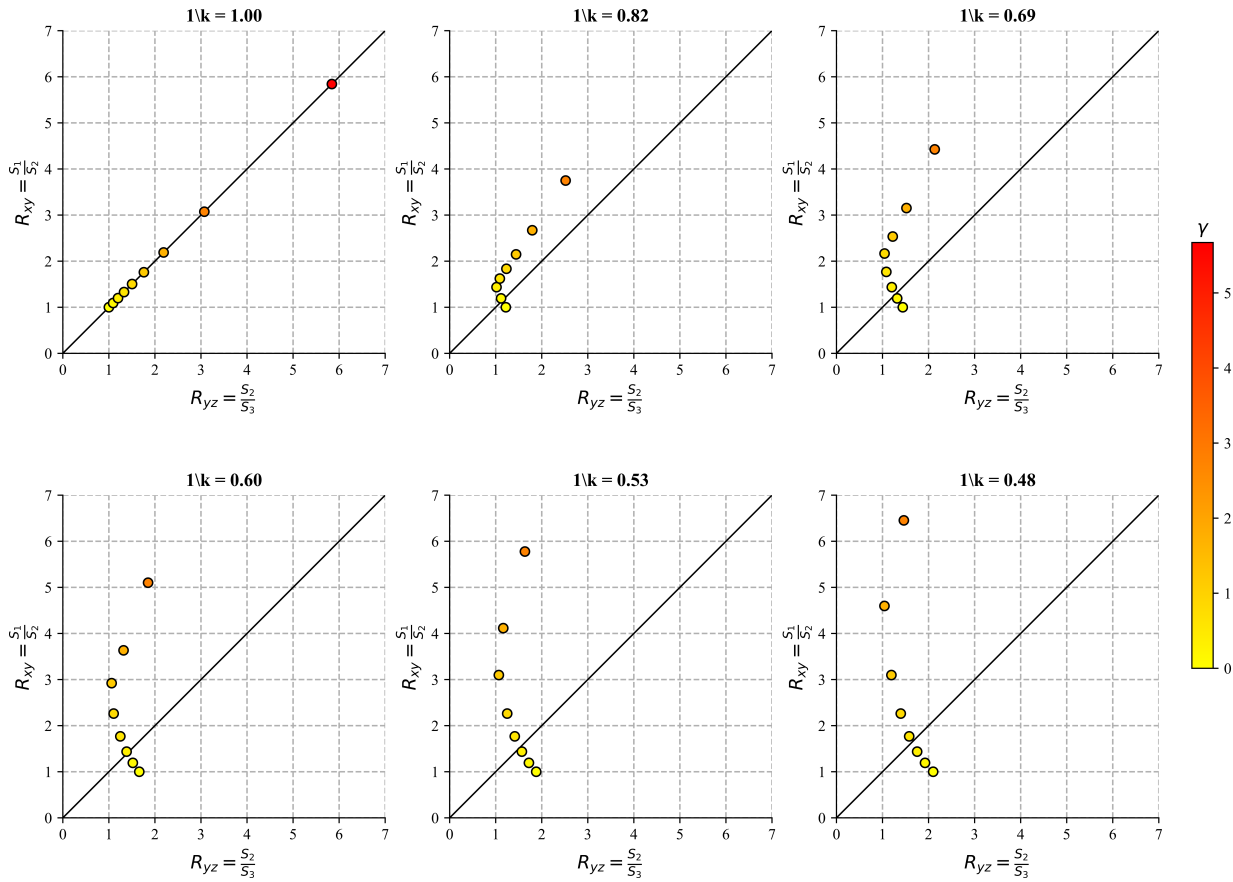
19

Figure 7: Flinn plot representation of all the final matrices given by the superimposition of a simple shear over a uniaxial flattening. Each diagram displays the results for a given $1/k$ value, with nine final matrices obtained by multiplying a simple shear matrix (SS_v), representing a vertical North-South oriented shear plane, with horizontal slip direction.

of this modeling are presented in six plots in Figure 8, where each plot corresponds to a different initial uniaxial compression value $(1/k)$. For each plot, a simple shear matrix was applied with increasing values of shear strain (γ), and from the final matrices representing the strain ellipsoid, the shape parameters were calculated again.

In a similar manner, for $1/k = 1$, applying the simple shear matrix to the initial fabric (perfect sphere) results in an evolution path of the ellipsoid along the plane strain ($K_{Flinn} = 1$). For the other scenarios, initial ellipsoids with an oblate shape are generated through uniaxial flattening in the Z direction. A stronger initial fabric is associated with a larger value of k (or smaller $1/k$), and imposing simple shear matrices causes changes in the final shape of the ellipsoid in terms of axial lengths. However, unlike the first scenario, the ellipsoids remain in the oblate field even with increasing values of shear strain (γ) (Figure 8).
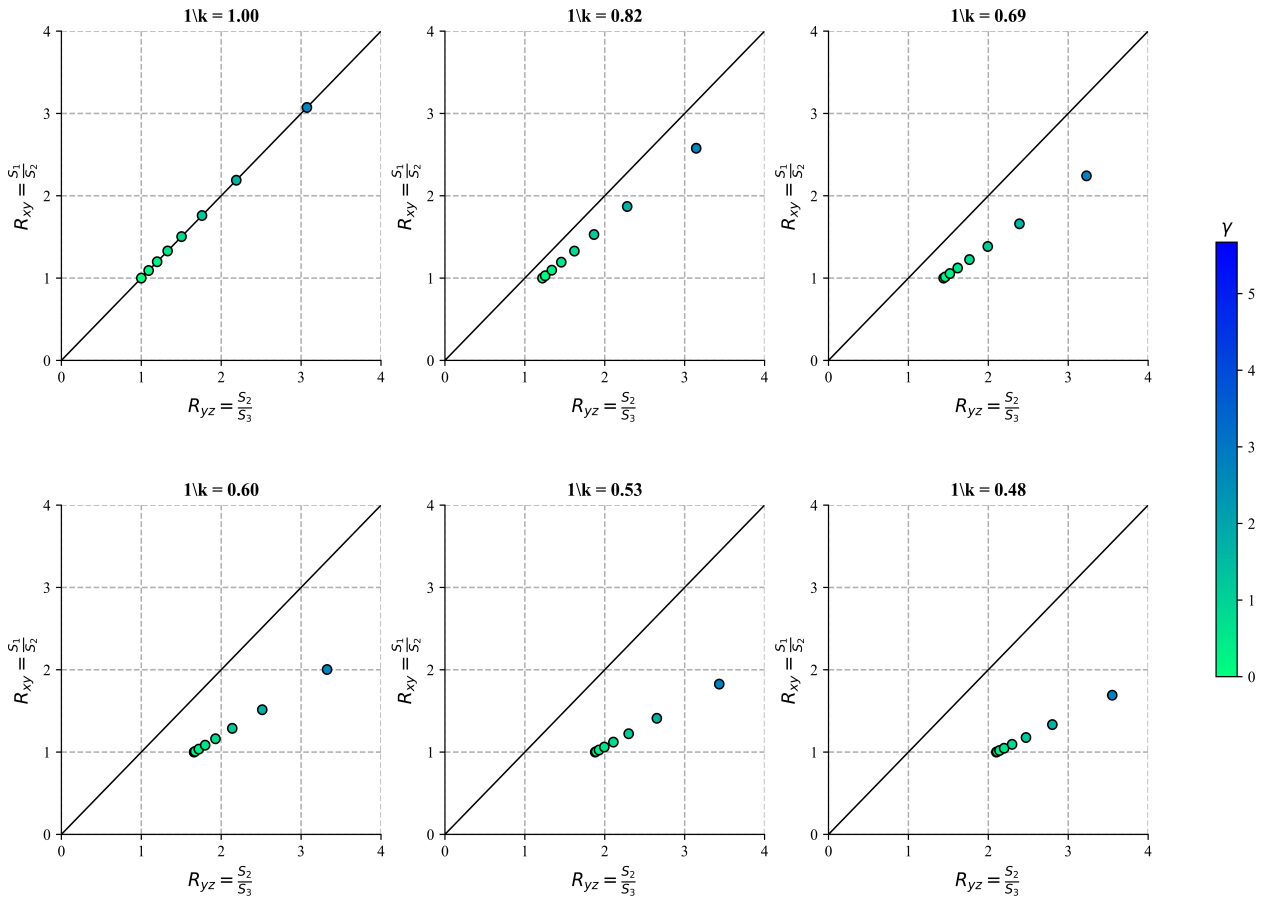
Figure 8: Flinn plot representation of all the final matrices given by the superimposition of a simple shear matrix over a uniaxial flattening. Each diagram displays the results for a given $1/k$ value, with nine final matrices obtained by multiplying a simple shear matrix (SS_h), representing a horizontal shear plane, with East-West slip direction.

5.5 *Strain integration*

Since the cross-section is generally drawn parallel to Z axes of the samples, the Z axial length, will be used to calculate the amount of shortening by the strain integration technique (Woodward et al., 1986; Hossack, 1978). After computing the original length, we found that the Northern Espinhaço Range and Western Chapada Diamantina fold-and-thrust belt underwent 16.30% and 17.02% shortening in the Z direction, respectively. It should be noted that the result presented here differs from that presented by Silva Neto et al. (2022) and represents a refinement of the previous results.

It is noticed that a data point (sample CD-16) was omitted in the calculation in the Chapada Diamantina region (Figure 9). This was done because, unlike all the other data points from both areas,

the calculated ellipsoid was not based on quartz grains as strain markers. Therefore, to maintain consistency in the analysis, it was disregarded.
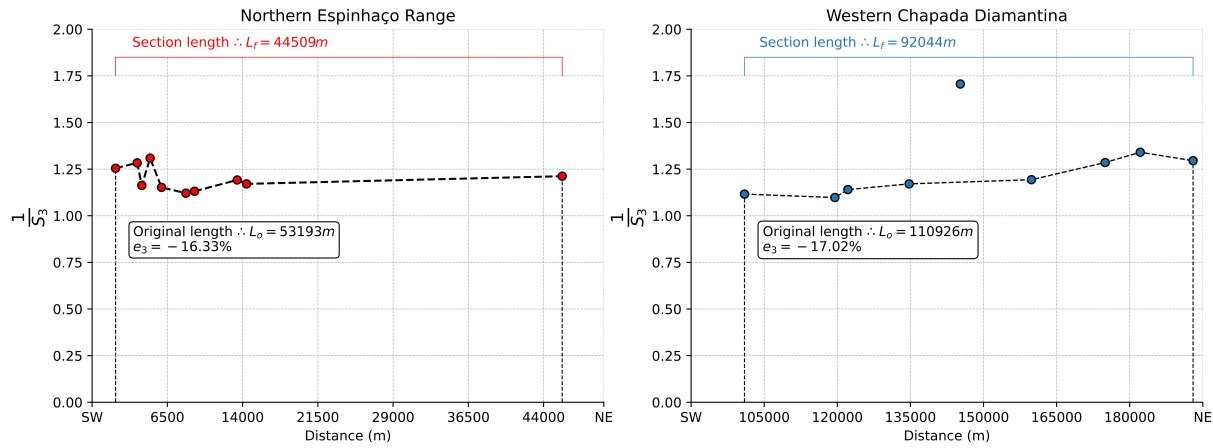

Figure 9: Finite strain integration: plot of the reciprocal stretch of Z axes along the section trajectory. The integration yields the area under the curve which is is the original length of the strain trajectory. Given the original section length, we can estimate the minimum shortening (e_3) that affected each of the fold-and-thrust belts. See the methodology for further details.

5.6 *Forward modeling*

We present the results of the scenario that best fits the available field observations and map interpretations, which consists of a sequence of southwestern and northeastern vergent thrusts, for the NER and WCD regions respectively. Although we tested different alternatives, the models were constructed based on stratigraphic relationships that cross-cut the section trace, as shown in Figure 4A, for the Northern Espinhaço Range and in Figure 4B, for the Western Chapada Diamantina.

For the Northern Espinhaço Range, the kinematic model begins with a crystalline basement unit overlain by a pre-rift unit horizon, and is subjected to northeast-directed crustal extension, by the development of listric normal faults, sequentially from fault 1 (older) to 3 (younger) (Figure 10). The model is simulated using a simple shear algorithm (White et al., 1986). During the rifting phase, syn-extensional units are deposited, represented by the Sapiranga Formation.

This is followed by the planar parallel deposition of post-extensional units, represented by the Fazendinha Formation, which covers the entire basin. The extensional phase then continues with the reactivation of normal faults with a northeast-directed displacement from fault 1 to 3, and deposition

22

of units from the Santo Onofre Group (including the João Dias, Serra da Garapa, and Serra do Boqueirão formations). At the end of the extensional stage, the scenario of the Northern Espinhaço Range original basin is reached, which is illustrated in Stage 1 of Figure 10.

Upon attaining the initial configuration of the sedimentary basin (Stage 1), inversion tectonic begins with the development of a thrust fault (4), with a southwestern sense of displacement, affecting the basement complex and thrusting it over the younger units of the basin (Figure 10 - Stage 2). This stage was characterized by a significant amount of deformation, which contributed to the development of the interpreted geometries and stratigraphic relationships represented in the maps, such as the overturned strata of the syn- and post-rift units (Fazendinha and Sapiranga formations) in that region (see Figure 4A).

The inversion process persists, characterized by the emergence of a thrust fault (5') that cuts across the entire sedimentary package, including the basement as well. This fault is responsible for the formation of folded structures on the surface. Subsequently, small step-like thrusts arise from the main fault, resulting in the repetition of cover units and minor folds (Figure 10 - Stage 3).

The southwest-directed movement persists as the old normal fault 3 is reactivated and transformed into the reverse fault 6'. This fault initiates the development of new thrusts, which repeat the upper layers of the sedimentary cover and control the formation of folds. The reverse fault 7' (old normal fault 2 in reverse) exhibits a ramp-flat-ramp geometry, causing thrusting of older sedimentary units over younger units, facilitated by detachment within the stratigraphic package. Lastly, the fault 8 represents the reactivation of the old normal fault 1, which results in the westward thrusting of the entire sedimentary package over the basement (Figure 10 - Stage 4).

The final step involves plotting the current topographic line and removing all material above it to obtain a possible representation for the study area subsurface (Figure 10 - Stage 5). The resulting representation is consistent with the stratigraphic relationships observed on the geological maps of the region and respects the available surface structural data. By comparing the final stage, representing the deformed current section (Stage 5), with the synthetic initial stage representing the original basin, a minimum tectonic shortening value of 13.46% is obtained.
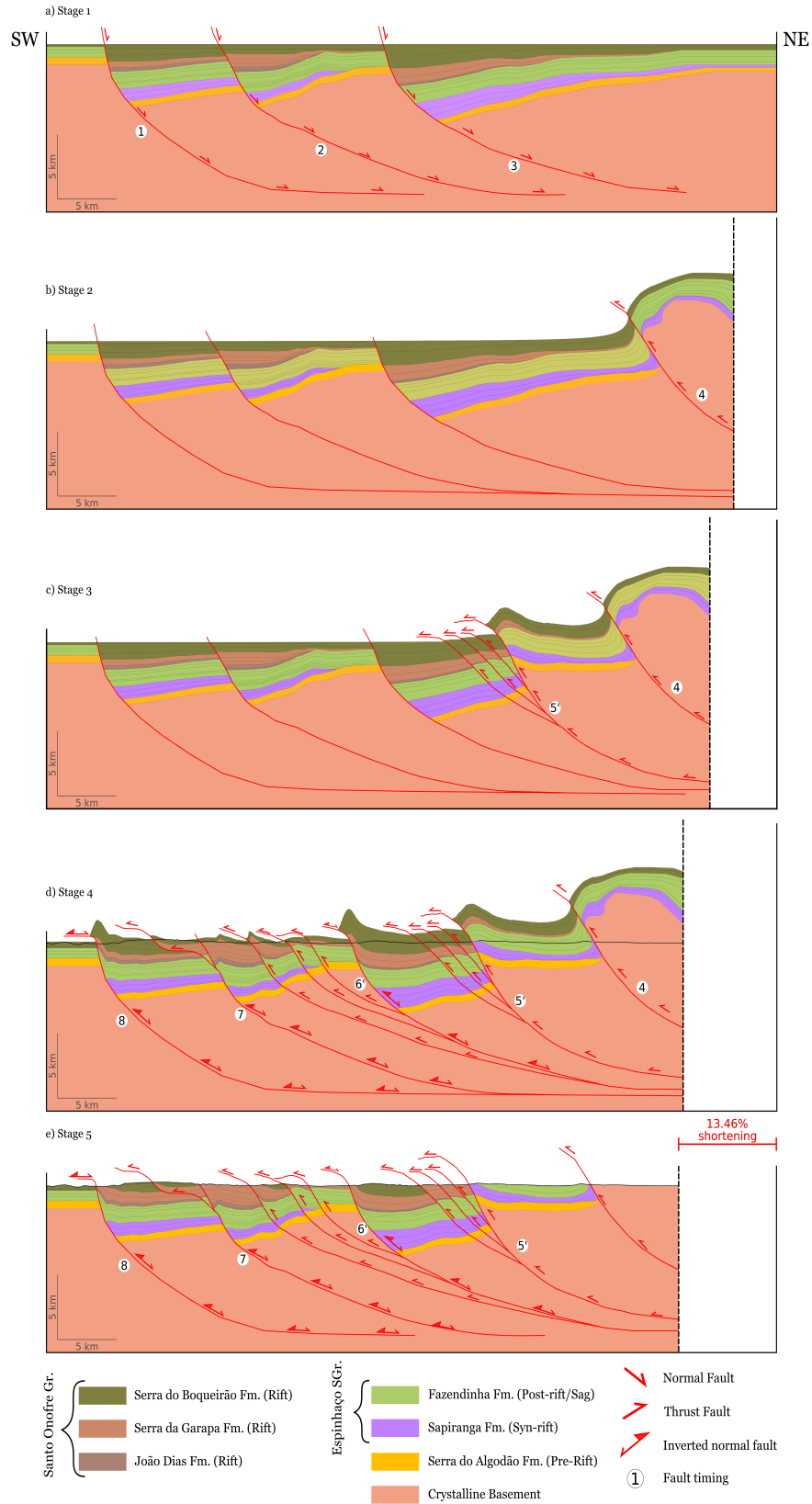
Figure 10: Kinematic forward model of the Northern Espinhaço Range fold-and-thrust belt, showing a predominant southwestern sequence of thrusts. Section trace is shown in Figure 4A.

We also present and describe the structural styles proposed for the Western Chapada Diamantina region, based on kinematic forward models (Figure 11). The proposed section runs across the Western Chapada Diamantina fold-and-thrust belt (FTB) involving large thin- and thick-skinned regional structures.

A possible and viable model for the Western Chapada Diamantina FTB is proposed, based on the reactivation of minor and major extensional normal faults separating structural highs and grabens in a formerly extensional basin. Although not shown here, the modelling started at the extensional phase, where we applied simple shear algorithm to model extension and syn-subsidence sedimentation. After the rifting phase, a short phase of erosion was applied on top of the syn-rift to construct the unconformity between syn- and the post-rift sedimentary packages (Figure 11A).

The tectonic inversion process started with the reactivation of the two easternmost faults, where fault (1) was responsible for uplifting the major Archean (Figure 11B). In the following stage, back-thrusts occurred with basement uplift, which resulted in folding of the sedimentary cover. This occurred due to the reactivation of minor buried normal faults (3) and partial inversion of extensional faults (4 and 5) (Figure 11C).

To continue modeling the sedimentary cover folding pattern, new thrust faults were introduced. These faults accounted for thick-skinned tectonics, and fault (6) represented a footwall shortcut thrust (Figure 11D). The propagation of fault (7) led to an increase in folding onto the structure, resulting in an overturned syncline. To account for present-day erosion, a topographic line similar to the present configuration was used in the model. When compared to surface interpretations and the overall style reported in previous publications in the study area, the model displayed a reasonable fit in structural style (Figure 11E).

By comparing the final stage, representing the deformed current section (Figure 11E) with the synthetic initial stage (Figure 11A), representing the original basin, a minimum tectonic shortening value of 18.5% is estimated for the Western Chapada Diamantina region.
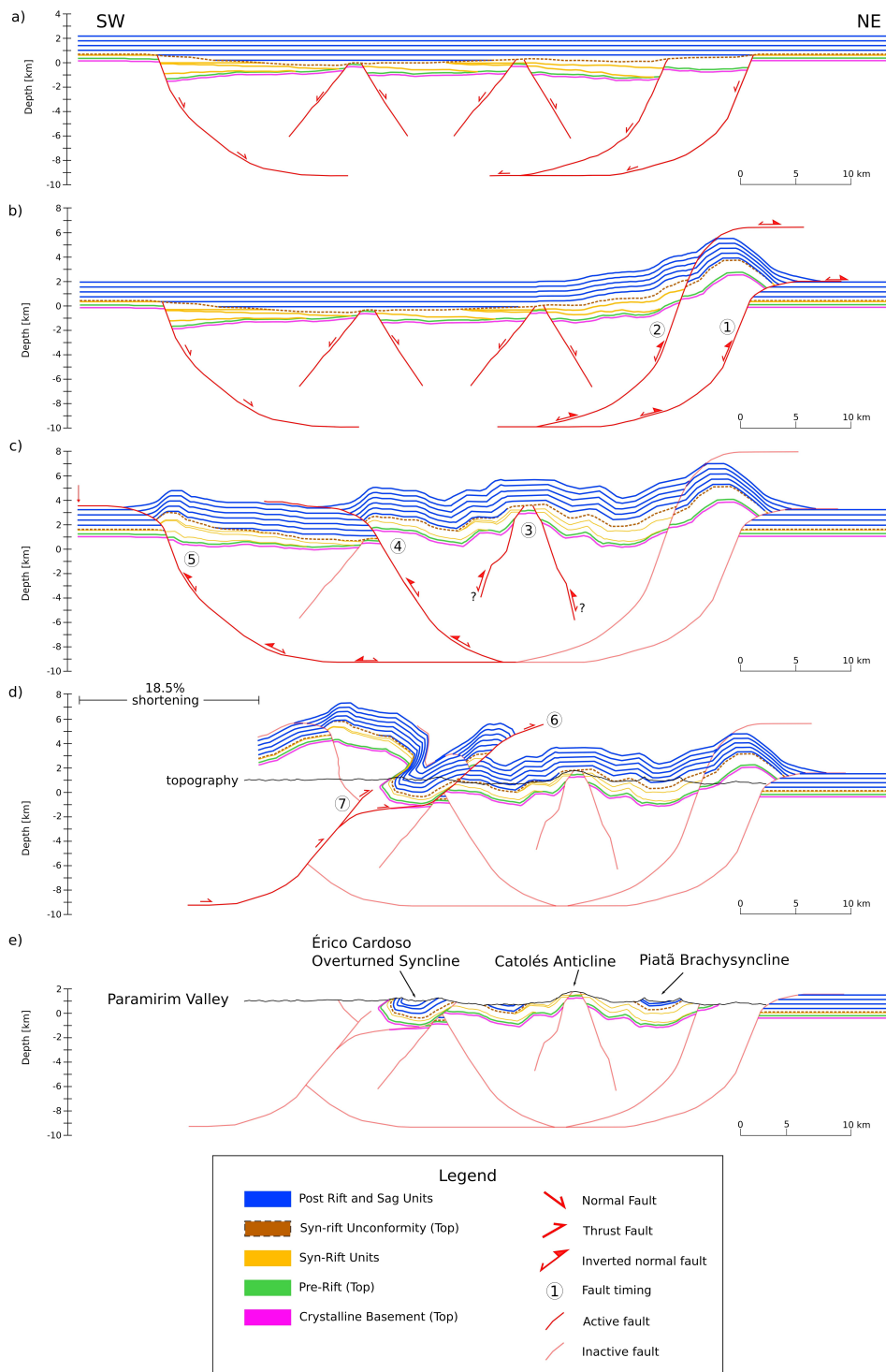
Figure 11: Kinematic forward modelling of the Western Chapada Diamantina region. Geological evolution is described in text. We warn the reader that the horizontal beds at east of the model do not represent the actual geology of the area, but rather a modeling artifact. See Guimarães et al. (2005) and Silva Neto et al. (2022) for more details of the regional main geological structures and model description.

6 DISCUSSION

6.1 *Finite strain*

The Inertia Tensor method has been widely used in finite strain analysis, and its potential has been demonstrated in previous research that utilized the shape preferred orientation (SPO) software (Launeau & Cruden, 1998; Zhang et al., 2013; McCarthy et al., 2015; Launeau et al., 2010; Sen & Mamtani, 2006). However, certain assumptions need to be met when using this method, such as the initial mean shape of the deformed objects being approximately equidimensional, and the deformation being passive without any viscosity contrast between the measured objects and their interstitial matrix (Launeau, 2004; Faleiros, 2008). In our study, we infer that these conditions were satisfied, as we primarily analyzed quartz grains in metasandstones, which are believed to have had an approximately spherical shape in their original sedimentary state. Furthermore, sample rock matrix displayed similar mineralogical composition to the quartz grains, indicating a non-rheological contrast. The combination of a large number of grains per section resulted in almost perfect ellipses, as demonstrated in the supplementary material, strengthening this interpretation.

Our analysis revealed a satisfactory agreement between the ellipsoid axes and the flattening foliations and stretching lineations measured in the field (compare Figs. 3 and 5). In both areas studied, we observed that the Z axial orientation aligns well with the foliation/slaty cleavage poles orientation. Specifically, in the Northern Espinhaço Range area, our results are consistent with the existence o f a steep NNW-striking flattening plane with a NE dip. In the Western Chapada Diamantina region, our findings support the presence of a steep NNW-striking flattening plane with a SW dip.

In the WCD domain, a concentration of down-dip stretching lineation is observed (Figure 3D), which is well-aligned with the axial orientation of the X-axis of the finite strain ellipsoids (Figure 5). In contrast, in the NER region, a distribution of sub-horizontal X-axes oriented SSW-NNE is observed, while the stretching lineations appear to have two clusters of dispersion: one pole of

concentration plunging to NE and one pole with SSW-NNE sub-horizontal orientation (Figures 5 and 3H).

Moreover, in the NER region, the possible existence of two clusters of dispersion of stretching lineation suggests the occurrence of strain partitioning, with the coexistence of thrusting and strike-slip tectonics, where the measured ellipsoids mainly display X-axes compatible with the latter settings. This scenario is also suggested by the existing geological maps of the area, where strike-slip faults, as the Santo Onofre fault, are represented (Guimarães et al., 2019; Danderfer Filho, 2000). Importantly, the strain techniques utilized in this study were entirely independent of the field measurements of foliation and lineation.

The shapes of the finite strain ellipsoids reveal a clear differentiation between the Western Chapada Diamantina and Northern Espinhaço Range regions. The former exhibits almost exclusively oblate ellipsoids, while the latter displays prolate ellipsoids (Figure 6). Usually the prolate and oblate ellipsoid shapes are interpreted as the result of transtension and transpression respectively (Sanderson & Marchini, 1984; Fossen et al., 1994; Fossen & Tikoff, 1998), but another deformational regimes are also possible (Ramsay & Wood, 1973; Merle & Gapais, 1997). Furthemore, the possibility that the oblate shape is related to a loss of volume cannot be completely dismissed, as pressure solution along tectonic cleavages is a common phenomenon in low-grade metasedimentary rocks (Ramsay & Wood, 1973). For these reasons we have carried out the matrix simulation as an attempt to explain the strain shapes obtained.

The finite strain matrix modeling results for the WCD domain indicate that initial oblate ellipsoids, when subjected to simple shear on a horizontal shear plane with an East-West slip direction, change their axial magnitudes according to the increase in the shearing angle but remain within the oblate field (Figure 8). This modeling could represent the ESW-ENE thrusts that define the main structuring of the Western Chapada Diamantina fold-and-thrust belt developed over an initial sedimentary fabric, as attested by other evidence (Figure 5, Figure 3D).

For the NER region, the finite strain ellipsoids are predominantly prolate (Figure 6), with X-axes sub-horizontal and oriented SSW-NNE. This pattern would be correlated with a transtensional

regime, which however is not consistent with field and mapping evidences. Our finite strain matrix modeling suggest that a North-South strike-slip deformation superimposed over an initial oblate fabrics, both from a initial sedimentary fabric or a sedimentary fabric plus a thrust regime, could explain the prolate finite strain shapes obtained for the NER. This scenario is supported by the field and geological mapping of the region (Guimarães et al., 2019; Danderfer Filho, 2000) where strike-slip faults (e.g. Santo Onofre fault) are recognized developing over former or simultaneous thrust faults. In this case, the existence of a strong component of strike-slip tectonics in the NER region is suggested, responsible for altering the shape of the ellipsoids.

6.2 *Geological model*

The initial concept adopted for the construction of the forward models assumes the structural archetype of a intracontinental rift basin consistent with the geological evolution of the study area. The model of inversion tectonics for the Paramirim aulacogen is widely assumed and it has also been tested (Cruz & Alkmim, 2006, 2017; D'Angelo et al., 2019; Silva Neto et al., 2022).

In practice, this means that with the increase of shortening during tectonic inversion, the originally normal faults were reactivated as reverse faults. In addition to the reactivation of rift faults, our model also tests the scenario of generating new shortcut thrust ramps faults associated with major reactivated structures (Stages 3 to 5 of Figure 10).

Our model incorporates a detachment level at around 13 km depth, allowing for the coexistence of both thin- and thick-skinned structures. For the Western Chapada Diamantina region, previous kinematic models have shown a detachment level at around 21 km deep, slightly deeper than what was modeled for the Northern Espinhaço Range. This variability and lack of data regarding the existence or not of a detachment level emphasizes the importance of further constraining uncertainties in the deep subsurface.

The structural models depicted in Figs.10-11 provides a feasible geometry and kinematics, leading to a valid and plausible structural representation of the Northern Espinhaço range and Western Chapada Diamantina fold-and-thrust belts, which is consistent with the current regional

understanding of the area (Cruz & Alkmim, 2006, 2017; Guimarães et al., 2019). Nevertheless, it is important to acknowledge that the structure at depth and geometric relationships between sedimentary units still needs further constraints to refine the proposed models.

6.3 *Tectonic shortening and implications*

We employed multiple and independent methods to assess tectonic shortening in the Northern Espinhaço Range and Western Chapada Diamantina fold-and-thrust belts (Figure 1). Kinematic forward modeling and integration of finite strain yielded a tectonic shortening range of 13.5% - 16.3% for the Northern Espinhaço Range, while the Western Chapada Diamantina fold-and-thrust belts exhibited a range of 17.02% - 18.5%. In addition, balanced cross section restoration was used in the latter region, yielding a maximum estimate of 19.4%, thus increasing the range to 17.02% - 19.4% (Silva Neto et al., 2022).

By combining and averaging the maximum estimates for the shortening ranges of the two belts, we obtained a range of approximately 15.3% - 17.8% of shortening. However, as there are no shortening estimations for the Paramirim valley, the total amount of shortening across the Paramirim corridor might be greater than our estimated interval.

Additionaly, combining the estimated original width (l_o) of the Northern Espinhaço Range and Western Chapada Diamantina basins, we estimate the composite intracratonic basin system width extension approximately 165 km. It is important to note that the estimation of the original composite intracratonic basin system width should be regarded as a conservative minimum value since it does not account for the Paramirim valley in the calculation.

7 CONCLUSIONS

This study presents refined, integrated data for the Western Chapada Diamantina fold-and-thrust belt and new data for the Northern Espinhaço Range, both located within the Paramirim corridor. The results include analysis of finite strain ellipsoid shape, axial orientation, and estimation of tectonic shortening. The key findings from this study can be summarized below:

i. The study found that both the Northern Espinhaço Range and the Western Chapada Diamantina fold-and-thrust belts exhibit similar ranges of finite strain intensity, as given by the X/Z ratio, when considering only samples with quartz grains as strain markers;

ii. The axial orientation of the finite strain ellipsoids is highly consistent with the orientation of the foliation and slaty cleavage planes, as well as the lineation data. Notably, in the Northern Espinhaço Range, the stretching lineation shows two clusters, with the sub-horizontal one being highly consistent with the X-axis dispersion;

iii. The majority of the ellipsoids in the Western Chapada Diamantina region are oblate in shape, while those in the Northern Espinhaço Range are prolate. This difference in shape suggests a important component of strike-slip tectonics in the NER region, responsible for altering the shape of the ellipsoids;

iv. For the WCD our data corroborates with the possibility of a thrust regime, while the NER region is suggestive of strain partitioning with the coexistence of SSW-NNE strike-slip and ENE-WSW thrusting;

v. Three independent techniques, finite strain integration, forward modeling and cross section restoration, were employed to estimate the tectonic shortening across the Paramirim corridor. The Northern Espinhaço Range exhibited a shortening estimation range of 13.5% to 16.3%, while the Western Chapada Diamantina exhibited a range of 17.02% to 19.4%, thus a range of approximately 13.5% - 19.4% for the Paramirim corridor. It should be noted that these

estimations represent a minimum shortening value, as they do not account for deformation in the Paramirim valley;

vi. The estimation of the original composite intracratonic basin system width of approximately 165 km, considering the Northern Espinhaço Range and Western Chapada Diamantina basins, provides valuable geometric constraints and serves as a reliable basis for further investigations into the kinematic and geological evolution of the Araçuaí West Congo orogenic building system;

vii. The minimum shortening estimate range of 13.5% - 19.4% in the Paramirim corridor highlights its nature as a Neoproterozoic deformation zone, supporting the hypothesis of a non-rigidity zone between the western and eastern cratonic regions of the São Francisco craton.

Overall, our findings suggest that the Northern Espinhaço Range and Western Chapada Diamantina fold-and-thrust belts experienced similar deformation intensities and orientations during the Brasiliano orogeny. However, it is important to note that the two areas may have undergone different deformation styles. Further research is needed to understand the specific mechanisms involved and their implications for the tectonic evolution of the region. Nevertheless, the results of this study offer valuable geometric constraints and a robust foundation for further investigations on the kinematic and geological evolution of the Araçuaí West Congo Orogenic building system within the São Francisco craton.

REFERENCES

Alkmim, F. F., Marshak, S., Fonseca, M. A. (2001). Assembling West Gondwana in the Neoproterozoic: clues from the Sao Francisco craton region, Brazil. *Geology*. 29(4), 319–322.

Alkmim, F. F., Marshak, S., Pedrosa-Soares, A. C., Peres, G. G., Cruz, S. C. P., Whittington, A. (2006). Kinematic evolution of the Araçuaí-West Congo orogen in Brazil and Africa: Nutcracker tectonics during the Neoproterozoic assembly of Gondwana. *Precambrian research*. 149(1-2), 43–64.

Alkmim, F. F., Martins-Neto, M. A. (2012). Proterozoic first-order sedimentary sequences of the São Francisco craton, eastern Brazil. *Marine and Petroleum Geology*. 33(1), 127–139.

Almeida, F. F. M. (1977). O cráton do São Francisco. *Revista Brasileira de Geociências*. 7(4), 349–364.

Almeida, F. F. M., de Brito Neves, B. B. d., Carneiro, C. D. R. (2000). The origin and evolution of the South American Platform. *Earth-Science Reviews*. 50(1-2), 77–111.

Arcanjo, J. B., Varela, P. H. L., Martins, A. A., Loureiro, H. S. C., Neves, J. P. (2000). *Projeto Vale do Paramirim*. Convênio CPRM/CBPM.

Bitencourt, C. N., Cruz, S. C. P., dos Anjos Cruz, V., Pedrosa-Soares, A. C., Paquette, J. L., Alkmim, A. R., Barbosa, J. S. F. (2019). Rifting events in the southern sector of the Paramirim Aulacogen, NE Brazil: New geochronological data and correlations for the São Francisco–Congo paleocontinent. *Precambrian Research*. 326, 417–446.

Brito Neves, B. B., Campos Neto, M. D. C., Fuck, R. A. (1999). From Rodinia to Western Gondwana: an approach to the Brasiliano-Pan African Cycle and orogenic collage. *Episodes*. 22(3), 155–199.

Brito Neves, B. B., Sá, J. M., Nilson, A. A., Botelho, N. (1995). A Tafrogênese Estateriana nos bocos Proterozóicos da américa do Sul e processos subsequentes. *Geonomos*. 3(2), 1–21.

Campanha, G. A. C. (2002). *O papel do sistema de zonas de cisalhamento transcorrentes na configuração da porção meridional da Faixa Ribeira*. Tese de Livre Docência. 108. Instituto de Geociências, Universidade de São Paulo.

Campos Neto, M. D. C. (2000). Orogenic systems from Southwestern Gondwana: an approach to Brasiliano–Pan African Cycle and orogenic collage in Southeastern Brazil. *Tectonic Evolution of South America*. 31, 335–365.

Cavalcante, C., Fossen, H., de Almeida, R. P., Hollanda, M. H. B., Egydio-Silva, M. (2019). Reviewing the puzzling intracontinental termination of the Araçuaí-West Congo orogenic belt and its implications for orogenic development. *Precambrian Research*. 322, 85–98.

Caxito, F. A., Hartmann, L. A., Heilbron, M., Pedrosa-Soares, A. C., Bruno, H., Basei, M. A., Chemale, F. (2022). Multi-proxy evidence for subduction of the Neoproterozoic Adamastor Ocean and Wilson cycle tectonics in the South Atlantic Brasiliano Orogenic System of Western Gondwana. *Precambrian Research*. 376, 106678.

Cruz, S., Miranda, L., Veiga, P. (2008). Província Uranífera de Lagoa Real, Bahia. *Companhia Baiana de Pesquisa Mineral-CBPM/Companhia de Pesquisa de Recursos Minerais-CPRM, Salvador, Bahia, Brazil*.

Cruz, S. C., Alkmim, F. F. (2006). The tectonic interaction between the Paramirim aulacogen and the Araçuaí belt, São Francisco craton region, Eastern Brazil. *Anais da Academia Brasileira de Ciencias*. 78(1), 151–173.

Cruz, S. C. P., Alkmim, F. F. (2017). The Paramirim Aulacogen. In Heilbron, M., Cordani, U. G., Alkmim, F. F. (Eds.), *São Francisco Craton, Eastern Brazil: Tectonic Genealogy of a Miniature Continent*. Cap. 6, 97–115. Springer.

Cruz, S. C. P., Alkmim, F. F., Barbosa, J. S. F., Dussin, I., Gomes, L. C. C. (2015). Tectonic inversion of compressional structures in the Southern portion of the Paramirim Corridor, Bahia, Brazil. *Brazilian Journal of Geology*. 45(4), 541–567.

Cruz, S. C. P., dos Santos Machado, G., Barbosa, J. S. F., Vitoria, R. S., Barbosa, N. S., Neto, O. B. V., Bitencourt, C. N., dos Anjos Cruz, V., Marinho, M. M. (2023). The statherian anorogenic magmatism in the paramirim aulacogen, são francisco-congo paleoplate: New data, synthesis and regional correlations. *Journal of South American Earth Sciences*. 104346.

Danderfer, A., Dardenne, M. A. (2002). Tectonoestratigrafia Da Bacia Espinhaço Na Porção Centro-Norte Do Cráton Do São Francisco: Registro De Uma Evolução Poliistórica Descontínua. *Revista Brasileira de Geociências*. 32(4), 449–460.

Danderfer, A., De Waele, B., Pedreira, A. J., Nalini, H. A. (2009). New geochronological constraints on the geological evolution of Espinhaço basin within the São Francisco Craton—Brazil. *Precambrian Research*. 170(1-2), 116–128.

Danderfer Filho, A. (1990). Análise estrutural descritiva e cinemática do Supergrupo Espinhaço na região da Chapada Diamantina (BA). Tese (Mestrado). Universidade Federal de Ouro Preto.

Danderfer Filho, A. (2000). *Geologia sedimentar e evolução tectônica do Espinhaço Setentrional, estado da Bahia*. Tese (Doutorado). Instituto de Geociências da Universidade de Brasília.

Danderfer Filho, A., Lana, C. d. C., Júnior, H. N., Costa, A. F. d. O. (2015). Constraints on the statherian evolution of the intraplate rifting in a paleo-mesoproterozoic paleocontinent: New stratigraphic and geochronology record from the eastern são francisco craton. *Gondwana Research*. 28(2), 668–688.

D'Angelo, T., Barbosa, M. S. C., Danderfer Filho, A. (2019). Basement controls on cover deformation in eastern chapada diamantina, northern são francisco craton, brazil: Insights from potential field data. *Tectonophysics*. 772, 228231.

Erslev, E. A. (1991). Trishear fault-propagation folding. *Geology*. 19(6), 617–620.

Faleiros, F. M. (2008). *Evolução de Terrenos Tectono-Metamórficos da Serrania do Ribeira e Planalto Alto Turvo (SP, PR)*. Tese (Doutorado). 306. Universidade de São Paulo.

Flinn, D. (1962). On folding during three-dimensional progressive deformation. *Quarterly Journal of the Geological Society*. 118(1-4), 385–428.

Fossen, H., Cavalcante, C., Konopásek, J., Meira, V. T., de Paes Almeida, R., Hollanda, M. H. B., Trompette, R. (2020). A critical discussion of the subduction-collision model for the Neoproterozoic Araçuaí-West Congo orogen. *Precambrian Research*. 105715.

Fossen, H., Tikoff, B. (1998). Extended models of transpression and transtension, and application to tectonic settings. *Geological Society, London, Special Publications*. 135(1), 15–33.

Fossen, H., Tikoff, B., Teyssier, C. (1994). Strain modeling of transpressional and transtensional deformation. *Norsk geologisk tidsskrift*. 74(3), 134–145.

François, C., Pubellier, M., Robert, C., Bulois, C., Jamaludin, S. N. F., Oberhänsli, R., Faure, M., St-Onge, M. R. et al. (2022). Temporal and spatial evolution of orogens: a guide for geological mapping. *Episodes Journal of International Geoscience*. 45(3), 265–283.

Guadagnin, F., Chemale Jr, F. (2015). Detrital zircon record of the Paleoproterozoic to Mesoproterozoic cratonic basins in the São Francisco Craton. *Journal of South American Earth Sciences*. 60, 104–116.

Guimarães, J. T., Nogueira, A. d. C., Carvalho, C. M. B. d., Neves, J. P. d., Medeiros, K. O. P., Texeira, L. R., Pereira, L. H. M., Di Salvio, L. P. P., Melo, R. C., Oliveira, R. G. d., Borges, V. P. et al. (2019). Projeto Igaporã-Macaúbas: Geologia e recursos minerais das folhas Boquira - SD.23-X-B-V, Macaúbas-SD.23-X-D-II e Riacho de Santana-SD.23-X-D-V, estado da Bahia. Technical report. CPRM.

Guimarães, J. T., Santos, R. A., Melo, R. C. (2005). Geologia da Chapada Diamantina Ocidental (Projeto Ibitiara-Rio de Contas). *Companhia Baiana de Pesquisa Mineral - CBPM, Companhia Pesquisa de Recursos Minerais - CPRM*.

Hossack, J. (1978). The correction of stratigraphic sections for tectonic finite strain in the Bygdin area, Norway. *Journal of the Geological Society*. 135(2), 229–241.

Konopásek, J., Cavalcante, C., Fossen, H., Janoušek, V. (2020). Adamastor–an ocean that never existed? *Earth-Science Reviews*. 205, 103201.

Launeau, P. (2004). Evidence of magmatic flow by 2-D image analysis of 3-D shape preferred orientation distributions. *Bulletin de la Société Géologique de France*. 175(4), 331–350.

Launeau, P., Archanjo, C. J., Picard, D., Arbaret, L., Robin, P.-Y. (2010). Two-and three-dimensional shape fabric analysis by the intercept method in grey levels. *Tectonophysics*. 492(1-4), 230–239.

Launeau, P., Cruden, A. R. (1998). Magmatic fabric acquisition mechanisms in a syenite: results of a combined anisotropy of magnetic susceptibility and image analysis study. *Journal of Geophysical Research: Solid Earth*. 103(B3), 5067–5089.

Launeau, P., Robin, P.-Y. F. (2005). Determination of fabric and strain ellipsoids from measured sectional ellipses—implementation and applications. *Journal of Structural Geology*. 27(12), 2223–2233.

Loureiro, H. S. C., Bahiense, I. C., Neves, J. P., Guimarães, J. T., Teixeira, L. R., Santos, R. A., Melo, R. C. (2009). *Geologia e recursos minerais da parte norte do corredor de deformação do Paramirim (Projeto Barra - Oliveira dos Brejinhos)*. Série Arquivos Abertos 33. Companhia Baiana de Pesquisa Mineral - CBPM.

Malvern, L. E. (1969). *Introduction to the Mechanics of a Continuous Medium*. Englewood, Prentice-Hall. 713p.

McCarthy, D. J., Meere, P. A., Petronis, M. S. (2015). A comparison of the effectiveness of clast based finite strain analysis techniques to AMS in sandstones from the Sevier Thrust Belt, Wyoming. *Tectonophysics*. 639, 68–81.

Means, W. D. (1978). *Stress and Strain: basic concepts of continuum mechanics for geologists.* New York, Springer-Verlag. 339p.

Meira, V. T., Garcia-Casco, A., Hyppolito, T., Juliani, C., Schorscher, J. H. D. (2019). Tectono-metamorphic evolution of the Central Ribeira Belt, Brazil: A case of late Neoproterozoic intracontinental orogeny and flow of partially molten deep crust during the assembly of West Gondwana. *Tectonics.* 38(8), 3182–3209.

Meira, V. T., García-Casco, A., Juliani, C., Almeida, R. P., Schorscher, J. H. D. (2015). The role of intracontinental deformation in supercontinent assembly: insights from the Ribeira Belt, Southeastern Brazil (Neoproterozoic West Gondwana). *Terra Nova.* 27(3), 206–217.

Merle, O., Gapais, D. (1997). Strains within thrust-wrench zones. *Journal of Structural Geology.* 19(7), 1011–1014.

Moraes, A. (2016). *Mecânica do contínuo para a geologia estrutural.* São Paulo, PERSE. 798p.

Oertel, G. (1996). *Stress and deformation: a handbook on tensors in geology.* Oxford University Press. 292p.

Pedrosa-Soares, A. C., Alkmim, F. F. (2011). How many rifting events preceded the development of the Araçuaí-West Congo orogen? *Geonomos.* 19, 244–251.

Pedrosa-Soares, A. C., Alkmim, F. F., Tack, L., Noce, C. M., Babinski, M., Silva, L. C., Martins-Neto, M. A. (2008). Similarities and differences between the Brazilian and African counterparts of the Neoproterozoic Araçuaí-West Congo orogen. *Geological Society, London, Special Publications.* 294(1), 153–172.

Pedrosa-Soares, A. C., Noce, C. M., Wiedemann, C. M., Pinto, C. P. (2001). The Araçuaí-West-Congo Orogen in Brazil: An overview of a confined orogen formed during Gondwanaland assembly. *Precambrian Research.* 110(1-4), 307–323.

Ramsay, J. G., Lisle, R. J. (2000). *Applications of continuum mechanics in structural geology. Techniques of modern structural geology..* v. 3. Academic Press.

Ramsay, J. G., Wood, D. S. (1973). The geometric effects of volume change during deformation processes. *Tectonophysics.* 16(3-4), 263–277.

Robin, P.-Y. F. (2002). Determination of fabric and strain ellipsoids from measured sectional ellipses—theory. *Journal of Structural Geology.* 24(3), 531–544.

Sanderson, D. J., Marchini, W. (1984). Transpression. *Journal of structural Geology.* 6(5), 449–458.

Schobbenhaus, C. (1996). As tafrogêneses superpostas Espinhaço e Santo Onofre, estado da Bahia: Revisão e novas propostas. *Brazilian Journal of Geology.* 26(4), 265–276.

Sen, K., Mamtani, M. A. (2006). Magnetic fabric, shape preferred orientation and regional strain in granitic rocks. *Journal of Structural Geology.* 28(10), 1870–1882.

Serra, J. (1982). *Image analysis and mathematical morphology.* London, Academic press.

Silva Neto, R. S., Campanha, G. A. C., Vidal-Royo, O., Launeau, P., Salazar-Mora, C. A. (2022). Tectonic shortening and strain magnitudes across the Chapada Diamantina Fold and Thrust Belt: New insights into the tectonic evolution of the Paramirim Aulacogen. *Journal of South American Earth Sciences.* 116, 103820.

Teixeira, L. R. (2000). *Projeto Vale do Paramirim. Relatório Temático de Litogeoquímica.* Convênio CPRM/CBPM.

Teixeira, W., Oliveira, E. P., Marques, L. (2017). Nature and Evolution of the Archean Crust of the São Francisco Craton. In Heilbron, M., Cordani, U. G., Alkmim, F. F. (Eds.), *São Francisco Craton, Eastern Brazil: Tectonic Genealogy of a Miniature Continent*. Cap. 3, 34–61. Springer.

Vidal-Royo, O., Ticona, D. E. M., Montano, G. B. (2022). Seismic interpretation challenges in the southern Subandean fold and thrust belt of Bolivia. In *Andean Structural Styles*. 359–369. Elsevier.

White, N. J., Jackson, J. A., McKenzie, D. P. (1986). The relationship between the geometry of normal faults and that of the sedimentary layers in their hanging walls. *Journal of Structural Geology*. 8(8), 897–909.

Woodward, N. B., Gray, D. R., Spears, D. B. (1986). Including strain data in balanced cross-sections. *Journal of Structural Geology*. 8(3-4), 313–324.

Zhang, Q., Giorgis, S., Teyssier, C. (2013). Finite strain analysis of the Zhangbaling metamorphic belt, SE China–Crustal thinning in transpression. *Journal of Structural Geology*. 49, 13–22.

8   SUPPLEMENTARY MATERIAL

8.1   *Tectonic shortening and strain magnitudes across the Chapada Diamantina Fold-and-Thrust Belt*: *New insights into the tectonic evolution of the Paramirim Aulacogen*

This paper, published in the Journal of South American Earth Sciences in the beginning of this masters course, analyzes data from the Western Chapada Diamantina fold-and-thrust belt, combining shape preferred orientation analysis, balanced cross sections, and kinematic forward models. The paper is available at https://doi.org/10.1016/j.jsames.2022.103820.

The study aimed to calculate strain magnitudes and tectonic shortening across the Western Chapada Diamantina fold and thrust belt through finite strain analysis and cross-section restoration. The authors used 3D strain analysis on oriented samples, which resulted in oblate-shaped ellipsoids with strain ratios (X/Z) varying from 1.190 to 2.504.

The proposed model for section balancing is consistent with the relationship between the former rift architecture and the folding style, which affects the sedimentary cover. The reactivation of normal faults controlled the localization and kinematics of thrust ramps. The authors successfully restored a geological cross section together with kinematic models and provided a geometrically viable geological model. Using three different and independent approaches, the authors estimated a range of minimum tectonic shortening between 18-22% at the Western Chapada Diamantina fold and thrust belt. These results suggest that the western and eastern parts of the São Francisco craton could not be considered as rigidly linked during the Neoproterozoic-Cambrian Brasiliano orogeny and were separated by the Paramirim aulacogen.

Tectonic shortening and strain magnitudes across the Chapada Diamantina Fold and Thrust Belt: New insights into the tectonic evolution of the Paramirim Aulacogen

Raulindo Santana Silva Neto [a,*], Ginaldo Ademar Cruz Campanha [a], Oskar Vidal-Royo [b], Patrick Launeau [c], Claudio Alejandro Salazar-Mora [a]

[a] *Departamento de Mineralogia e Geotectônica, Instituto de Geociências, Universidade de São Paulo, Rua do Lago, 562, São Paulo, 05508-900, SP, Brazil*
[b] *Terractiva Consulting SL, Barcelona, Spain*
[c] *Laboratoire de Planétologie et Géodynamique, Université de Nantes, Faculté des Sciences et des Techniques, rue de la Houssinière, 2, Nantes, 440721, France*

ARTICLE INFO

ABSTRACT

In this study, strain magnitudes and tectonic shortening across the Chapada Diamantina fold-and-thrust belt are calculated by finite strain analysis, cross-section restoration and kinematic forward models. A total of 9 complete 3D strain analyses on oriented samples were conducted by the Inertia Tensor method and best fit ellipsoids were computed, resulting in strain ratios (X/Z) varying from 1.190 to 2.504. Predominant oblate shaped ellipsoids related to down-dipping stretching directions are associated with regional transport direction from SW to NE, with reverse faults, upright axial-plane fold and sub-horizontal axis. The restoration of the cross-section yielded a shortening of 19.37%, understood as the minimum tectonic shortening. The adopted model assumes the inversion of former extensional faults (steep thrusts), where the structural architecture of the area is mainly controlled by the inherited rift basin architecture, with basement involvement in a combination of thick and thin skin deformation. Similarly, the assessment of kinematic forward models resulted in a minimum shortening of 18.5%. Comparably, finite strain data integration techniques yielded a total of 21.65% of regional tectonic shortening, representing the horizontal component of ductile flattening strain across the section due to penetrative strain. Therefore, we present, by three different and independent approaches, an estimate range of tectonic shortening between 18%–22% at the western Chapada Diamantina region, but the total amount of shortening across the Paramirim aulacogen might have been greater. These results suggest that the western and eastern parts of the São Francisco craton could not be considered as rigidly linked during the Neoproterozoic–Cambrian Brasiliano orogeny, with the Paramirim aulacogen exerting an import role.

1. Introduction

The Paramirim Aulacogen or Corridor is understood as an intracontinental rift system nucleated around the Statherian Period in the central area of the São Francisco–Congo craton, which provided an accommodation space for a long bacinal stage with alternating pulses of mechanical and flexural subsidence (Pedrosa-Soares and Alkmim, 2011; Cruz and Alkmim, 2017). The filling units are mainly siliciclastic and metavolcanic rocks of the Espinhaço Supergroup that outcrop in the Northern Espinhaço Range towards west, in the Paramirim Valley in the central region and in Chapada Diamantina in the eastern region (Fig. 1) (Danderfer Filho, 1990; Danderfer and Dardenne, 2002; Guimarães et al., 2005; Cruz and Alkmim, 2017).

During the Brasiliano–Pan African orogenic cycle (Ediacaran period), the Paramirim Aulacogen was partially inverted due to the amalgamation of Western Gondwana paleocontinent. During this context of tectonic inversion, two thrust-and-fold belts were developed, Northern Espinhaço Range and Chapada Diamantina, with thick and thin skinned deformation (Cruz and Alkmim, 2017, 2006; Danderfer Filho, 1990).

Although the model of an indivisible São Francisco craton, as proposed by Almeida (1977), has been predominant in the regional literature, another models have already been proposed, as the existence of two cratons, São Francisco and Salvador, separated by the Paramirim Aulacogen (Cordani, 1973, 1978; Trompette et al., 1992b,a). The dominant model suggests that the Paramirim Aulacogen is an inverted

---

8.2 *Finite strain matrix modeling scripts*

The following scripts were written in Python (3.8.10) with the purpose of performing calculations related to finite strain matrix modeling for the Northern Espinhaço Range domain.

```python
# libraries import
import numpy as np
import matplotlib.pyplot as plt
import numpy as np
from sys import float_info

# plot font choose
plt.rcParams["font.family"] = "Times New Roman"
labelfont = {'fontname':'Times New Roman'}

# Function definitions
def eig_values(matrix):
    '''
    Calculate eigenvalues and return stretch values

    Parameters:
    matrix (numpy array): input matrix

    Returns:
    S1, S2, S3 (float): stretch values
    '''
    # vals = The eigenvalues in ascending order
    vals, vecs = np.linalg.eigh(matrix)

    # As the tensor is Cauchy, the eigenvalues are the reciprocal quadratic elongation
    # To convert to Stretch (S): S = (1/L')^1/2
    S1 = np.sqrt(1/vals[0])
    V1 = vecs[:, 0]

    S2 = np.sqrt(1/vals[1])
    V2 = vecs[:, 1]

    S3 = np.sqrt(1/vals[2])
    V3 = vecs[:, 2]

    return S1, S2, S3
```

```python
def eig_vecs(matrix):
    '''
    Calculate eigenvectors and return normalized eigenvectors

    Parameters:
    matrix (numpy array): input matrix

    Returns:
    V1, V2, V3 (numpy array): normalized eigenvectors
    '''
    # vecs = The column v[:, i] is the normalized eigenvector corresponding
    # to the eigenvalue w[i]
    vals, vecs = np.linalg.eigh(matrix)

    # As the tensor is Cauchy, the eigenvalues are the reciprocal quadratic elongation
    # To convert to Stretch (S): S = (1/L')^1/2
    S1 = np.sqrt(1/vals[0])
    V1 = vecs[:, 0]

    S2 = np.sqrt(1/vals[1])
    V2 = vecs[:, 1]

    S3 = np.sqrt(1/vals[2])
    V3 = vecs[:, 2]

    return V1, V2, V3

def add_identity(axes, *line_args, **line_kwargs):
    '''
    Add a diagonal line of identity to a plot. Parameters:
    axes (matplotlib axes object): plot object
    *line_args: arguments for line properties
    **line_kwargs: keyword arguments for line properties

    Returns:
    axes (matplotlib axes object): plot object with diagonal line of identity
    '''
    identity, = axes.plot([], [], *line_args, **line_kwargs)
    def callback(axes):
        low_x, high_x = axes.get_xlim()
        low_y, high_y = axes.get_ylim()
        low = max(low_x, low_y)
        high = min(high_x, high_y)
        identity.set_data([low, high], [low, high])
    callback(axes)
    axes.callbacks.connect('xlim_changed', callback)
    axes.callbacks.connect('ylim_changed', callback)
    return axes
```

```python
def preventDivisionByZero(some_array):
    '''
    Replace zero values in an array with a small value to prevent division by zero

    Parameters:
    some_array (numpy array): input array

    Returns:
    corrected_array: array with zero values replaced with small values
    '''
    corrected_array = some_array.copy()
    for i, entry in enumerate(some_array):
        # If element is zero, set to some small value
        if abs(entry) < float_info.epsilon:
            corrected_array[i] = float_info.epsilon

    return corrected_array

def PhitoGamma(phi):
    '''
    Convert shear angle (phi) to shear deformation (gamma)

    Parameters:
    phi (float): shear angle in degrees

    Returns:
    gamma (float): shear deformation
    '''
    gamma = np.tan(np.deg2rad(phi))
    return gamma


def GammatoPhi(gamma):
    '''
    Convert shear deformation (gamma) to shear angle (phi)

    Parameters:
    gamma (float): shear deformation

    Returns:
    phi (float): shear angle in degrees
    '''
    phi = np.rad2deg(np.arctan(gamma))
    return
#-------------------------------------
```

```python
# uniaxial flattening followed by simple shear
# Vertical Simple Shear NS shear plane, slip horizontal
# Define subplots with same size
fig, axs = plt.subplots(nrows=2, ncols=3, figsize=(16, 10))
plt.rcParams["font.family"] = "Times New Roman"
labelfont = {'fontname':'Times New Roman'}

# Create a list of values to iterate over
k_values = np.linspace(1, 2.1, 6)
phi_values = np.arange(0, 81, 10) # iterate until the second-to-last point

initial_k = []
gamma_val = []
x1_E_val  =  []
x2_N_val  =  []
x3_Z_val  =  []
kflinn_val= []
s1s2_val  =  []
s2s3_val  =  []

# Iterate over k_values
for i, k in enumerate(k_values):
    # Create a 2D transformation matrix for vertical uniaxial compression
    UC = np.array([[1, 0, 0],
                   [0, 1, 0],
                   [0, 0, 1/k]])

    # Create lists to store values
    s1s2 = [] # Stores s1/s2 ratios
    s2s3 = [] # Stores s2/s3 ratios
    Kf = [] # Stores K-Flinn values

    # Iterate over psi_values
    for phi in phi_values:
        # Convert psi to gamma
        gamma = np.tan(np.deg2rad(phi))
        # Create a 2D transformation matrix for simple shear
        # Vertical NS shear plane, with horizontal slip direction
        CS = np.array([[1, 0, 0],
                       [gamma, 1, 0],
                       [0, 0, 1]])

        F = np.matmul(CS, UC) # Calculate final transformation matrix F = CS*UC
        # Calculate Cauchy stress tensor (C)
        C = np.matmul((np.linalg.inv(F)).T, np.linalg.inv(F))

        # Calculate eigenvalues reported as stretch
        s1, s2, s3 = eig_values(C)
```

```python
            # store data for plot
            s1s2.append(s1/s2)
            s2s3.append(s2/s3)
            # Calculate K-Flinn value
            k_flinn = ((s1/s2))/((s2/s3))
            # Store vals for table
            initial_k.append(1/k)
            gamma_val.append(gamma)
            x1_E_val.append(s1)
            x2_N_val.append(s2)
            x3_Z_val.append(s3)
            s1s2_val.append(s3/s2)
            s2s3_val.append(s2/s3)
            kflinn_val.append(k_flinn)

# Flinn Plot
# Create scatter plot
ax = axs[i//3, i%3]
sc = ax.scatter(x=s2s3, y=s1s2, c=np.tan(np.deg2rad(phi_values)),
                cmap='autumn_r', zorder=3,edgecolors='black')
# Identity line
add_identity(ax, color='black', ls='-', lw=1, zorder=2)
ax.set_box_aspect(1)

# Add colorbar
if i == len(k_values) - 1:
    cbar = plt.colorbar(sc, ax=axs, shrink=0.5, spacing = 'uniform')
    cbar.ax.set_title(r'$\gamma$')

# Configure plot
# Set axis labels
ax.set_ylabel(r'$R_{xy}=\frac{S_1}{S_2}$', fontsize=12);
ax.set_xlabel(r'$R_{yz}=\frac{S_2}{S_3}$', fontsize=12, **labelfont);
#title
ax.set_title(r'1\k = %0.2f' % (1/k), fontweight='bold', **labelfont)
#grid
ax.grid(True, ls='--', lw=1, zorder=-1)
# Set axis limits
ax.set_xlim(0, 7)
ax.set_ylim(0, 7)
ax.set_xticks(ticks=np.arange(0,7.1, 1))
ax.set_yticks(ticks=np.arange(0,7.1, 1))

# Hide the right and top spines
ax.spines[['right', 'top']].set_visible(False)

plt.tight_layout()
plt.show()
```

```python
#----------------------------------------------------------------------------
# uniaxial flattening followed by simple shear
# Simple Shear Horizontal EW shear plane, with shear direction EW
# Define subplots with same size
fig, axs = plt.subplots(nrows=2, ncols=3, figsize=(16, 10))

# Create a list of values to iterate over
k_values = np.linspace(1, 2.1, 6)
phi_values = np.arange(0, 81, 10) # iterate until the second-to-last point

# Iterate over k_values
for i, k in enumerate(k_values):
    # Create a 2D transformation matrix for vertical uniaxial flattening
    UC = np.array([[1, 0, 0],
                   [0, 1, 0],
                   [0, 0, 1/k]])

    # Create lists to store values
    s1s2 = [] # Stores s1/s2 ratios
    s2s3 = [] # Stores s2/s3 ratios
    Kf = [] # Stores K-Flinn values

    # Iterate over psi_values
    for phi in phi_values:
        gamma = np.tan(np.deg2rad(phi)) # Convert psi to gamma
        # Create a 2D transformation matrix for simple shear
        # horizontal shear plane with EW slip direction
        CS = np.array([[1, 0, gamma],
                       [0, 1, 0],
                       [0, 0, 1]])

        F = np.matmul(CS, UC) # Calculate final transformation matrix F = CS*UC
        # Calculate Cauchy stress tensor (c)
        C = np.matmul((np.linalg.inv(F)).T, np.linalg.inv(F))
        s1, s2, s3 = eig_values(C) # Calculate eigenvalues

        s1s2.append(s1/s2)
        s2s3.append(s2/s3)

        k_flinn = ((s1/s2))/((s2/s3)) # Calculate K-Flinn value
        Kf.append(np.round(k_flinn,3))

    # Flinn Plot
    # Create scatter plot
    ax = axs[i//3, i%3]
    sc = ax.scatter(x=s2s3, y=s1s2, c=np.tan(np.deg2rad(phi_values)),
                    cmap='winter_r', zorder=3,edgecolors='black')
    add_identity(ax, color='black', ls='-', lw=1, zorder=2) # Identity line
```

```python
        ax.set_box_aspect(1)

        # Add colorbar
        if i == len(k_values) - 1:
            cbar = plt.colorbar(sc, ax=axs, shrink=0.5)
            cbar.ax.set_title(r'$\gamma$')

        # Configure plot
        # Set axis labels
        ax.set_ylabel(r'$R_{xy}=\frac{S_1}{S_2}$', fontsize=12);
        ax.set_xlabel(r'$R_{yz}=\frac{S_2}{S_3}$', fontsize=12, **labelfont);
        #title
        ax.set_title(r'1\k = %0.2f' % (1/k), fontweight='bold', **labelfont)
        #grid
        ax.grid(True, ls='--', lw=1, zorder=-1)
        # Set axis limits
        ax.set_xlim(0, 4)
        ax.set_ylim(0, 4)
        ax.set_xticks(ticks=np.arange(0,4.1, 1))
        ax.set_yticks(ticks=np.arange(0,4.1, 1))

        # Hide the right and top spines
        ax.spines[['right', 'top']].set_visible(False)

plt.show()
```

8.3 *Finite strain data - Northern Espinhaço Range*

Here we provide field information regarding the samples utilized for finite strain analysis in this work (Table 2). We also present the shape preferred orientation (SPO) ellipses of each sample obtained by the Inertia Tensor method (Launeau & Cruden, 1998). Later, all ellipses were used to compute the best fit ellipsoid using the using the software *ELLIPSOID* (Robin, 2002; Launeau & Robin, 2005). Finally, Table 3 summarizes the 2D strain data obtained for all samples used in this study followed by all microphotographs and computed shape preferred ellipses for all samples.

Table 2: Geographic and geological information regarding the samples utilized in this study.

Site	X	Y	Lithology	Map Unit	Slaty Cleavage (Clar)	Slaty Cleavage (RHR)	Foliation by Ellipsoid (RHR)
NER-07	-42.8858	-13.5659	Meta-qtz-sandstone	João Dias Fm.	245/19	155/19	168/56
NER-46	-42.5962	-13.5178	Meta-qtz-sandstone	Sapiranga Fm.	086/74	356/74	006/54
NER-53	-42.5785	-13.5163	Meta-qtz-sandstone	Serra do Boqueirão Fm.	065/70	335/70	337/47
NER-56	-42.8792	-13.5472	Meta-qtz-sandstone	Serra do Boqueirão Fm.	228/75	138/75	190/67
NER-57	-42.8718	-13.5433	Meta-qtz-sandstone	Serra do Boqueirão Fm.	230/74	140/74	134/71
NER-60	-42.8558	-13.5362	Meta-qtz-sandstone	Serra da Garapa Fm.	255/61	165/61	140/57
NER-62	-42.8499	-13.5344	Meta-qtz-sandstone	Serra do Boqueirão Fm.	-	-	337/68
NER-64	-42.9010	-13.5625	Quartzite	João Dias Fm.	205/48	115/48	124/75
NER-75B	-42.8107	-13.5577	Meta-qtz-sandstone	Serra do Boqueirão Fm.	244/54	154/54	168/54
NER-79	-42.8166	-13.5620	Meta-qtz-sandstone	Serra do Boqueirão Fm.	062/46	335/46	356/53

Table 3: Two Dimensional (2D) Strain Data - Shape preferred orientation ellipses for all planes used to compute best fit ellipsoids.

Sample Code	A Plane				B Plane				C Plane			
	n	R_s	Strike	Dip	n	R_s	Strike	Dip	n	R_s	Strike	Dip
NER-07	247	1.641	175	22	238	1.341	025	76	335	1.247	289	76
NER-46	490	1.299	210	27	621	1.317	095	79	410	1.205	357	73
NER-53	400	1.077	223	80	307	1.456	130	71	300	1.318	340	20
NER-56	322	1.293	153	57	330	1.450	337	30	284	1.408	069	87
NER-57	371	1.244	334	81	415	1.226	067	86	309	1.142	181	13
NER-60	354	1.189	163	84	460	1.204	073	54	304	1.097	253	38
NER-62	441	1.089	015	79	377	1.045	284	74	366	1.282	142	18
NER-64	248	1.505	012	75	210	1.251	260	36	200	1.255	110	55
NER-75B	312	1.265	063	75	305	1.261	161	69	304	1.212	300	30
NER-79	439	1.328	152	89	324	1.254	256	33	337	1.097	063	57

- n is the number of quartz grains analyzed in each thin section to compute the SPO ellipse;
- Strike direction follows the right hand rule convention and it represents thin section orientation;
- item R_s is the SPO ellipse shape ratio.

Sample NER-07 is a fine- to medium-grained, massive, well-sorted quartzite with high textural maturity. Petrographic sections indicate that the boundaries between quartz grains are marked by inclusions of other minerals and by dynamic recrystallization of quartz textural features (bulging).
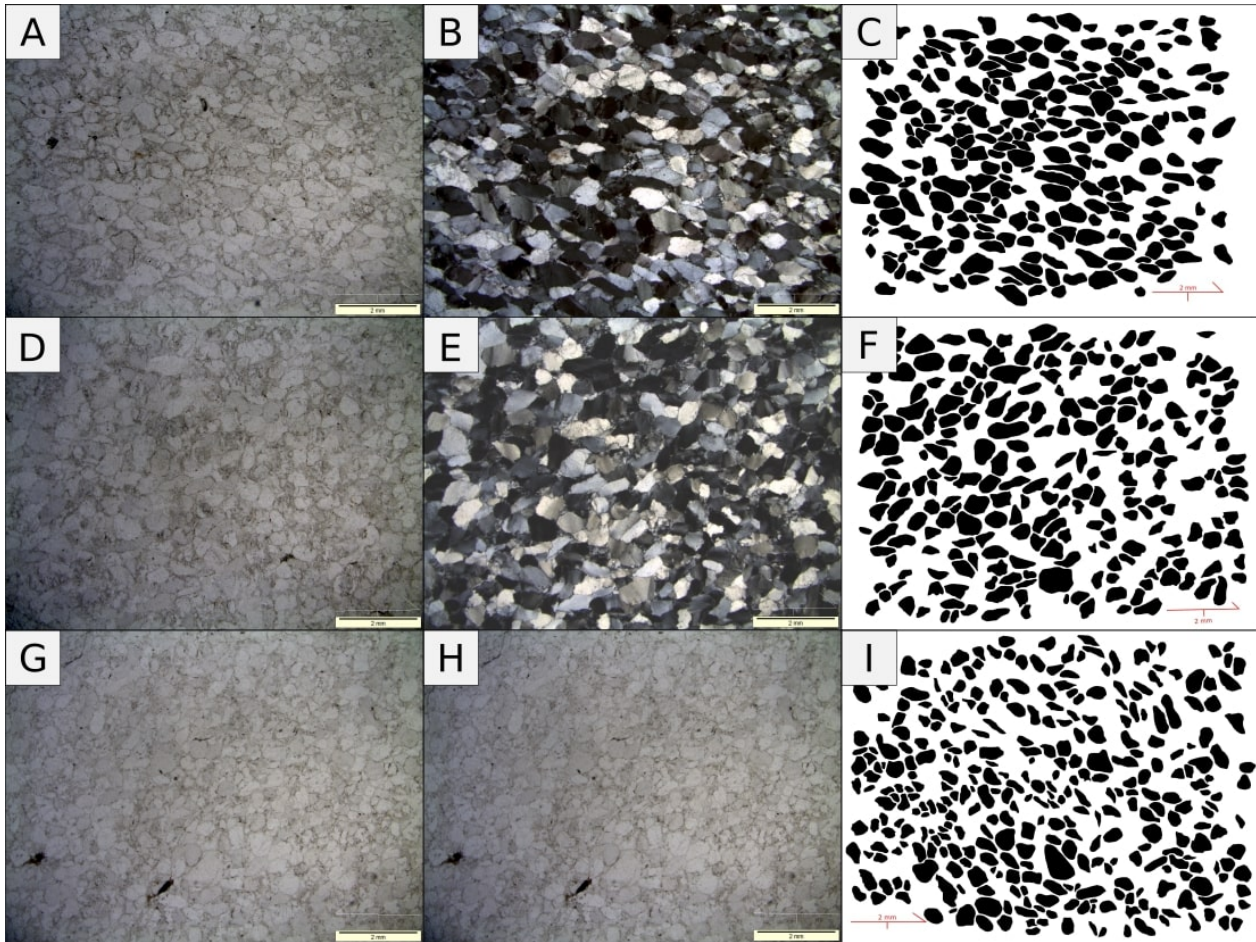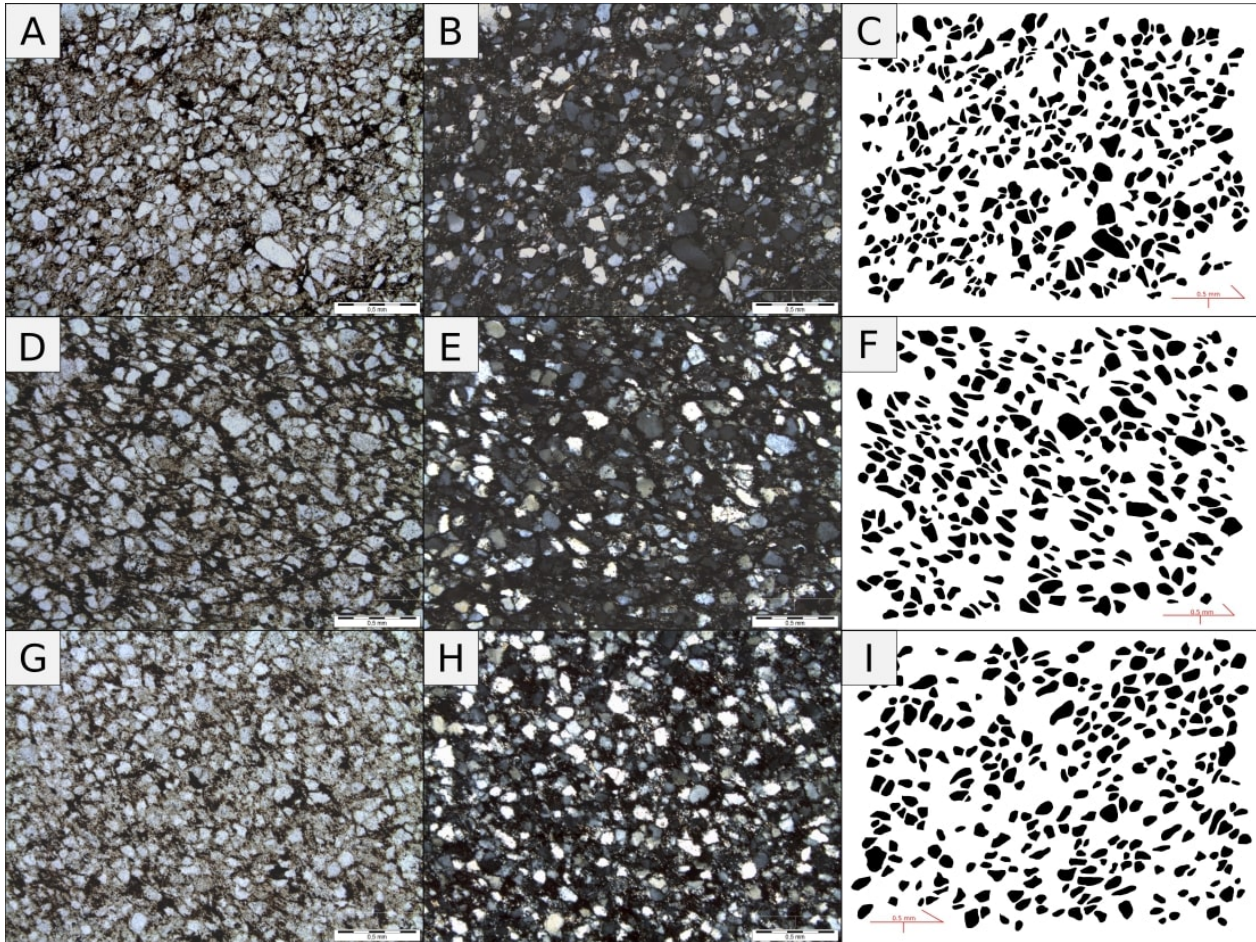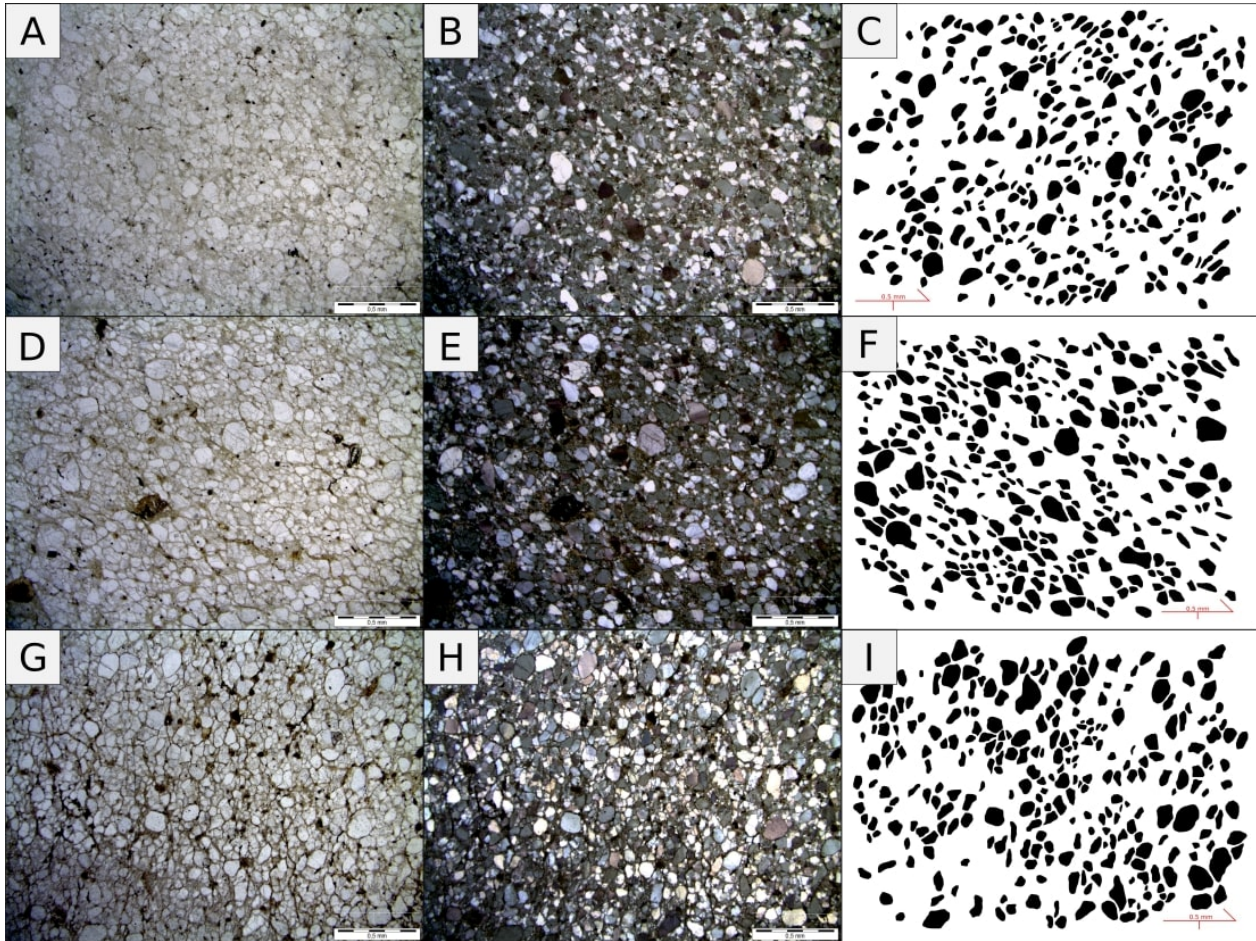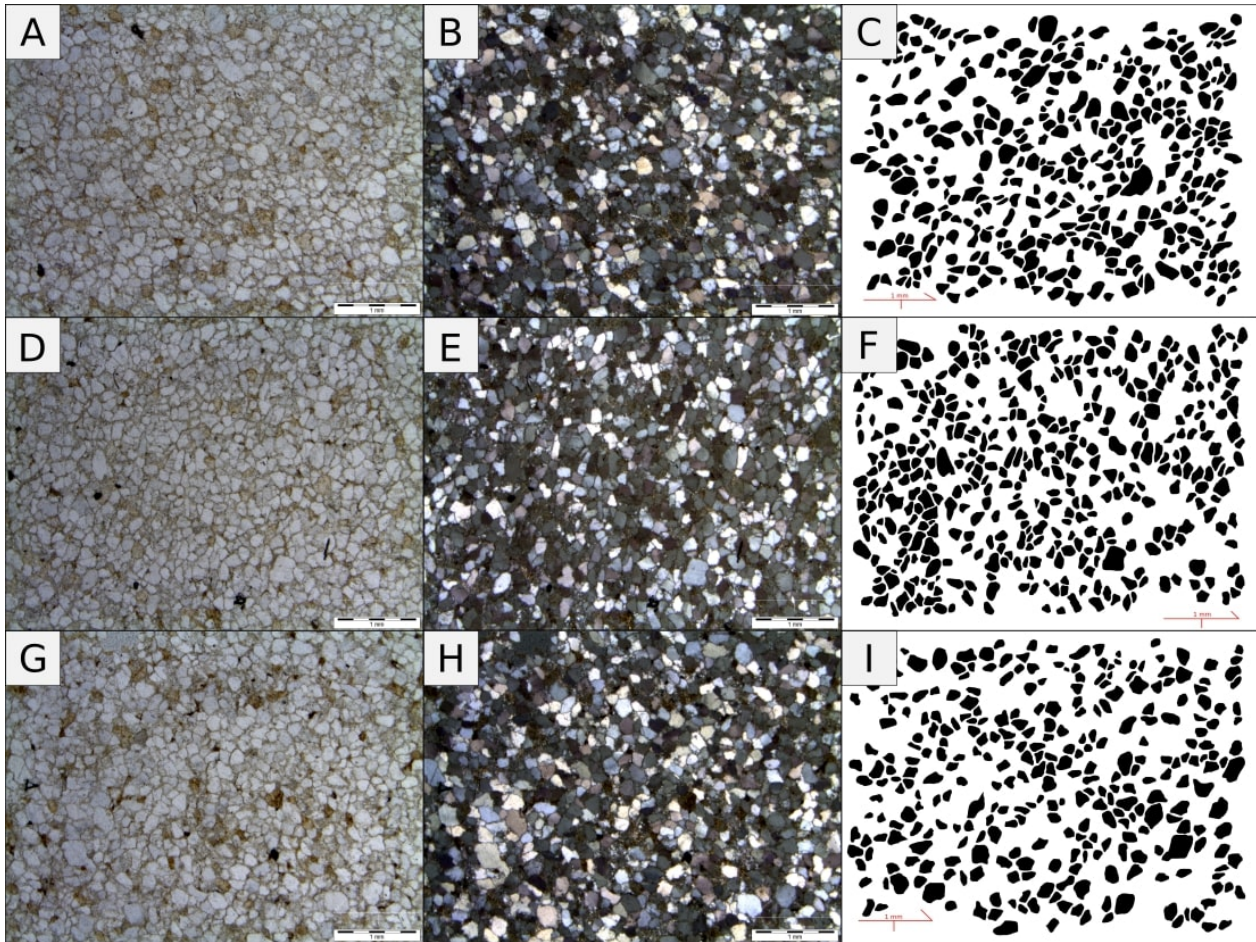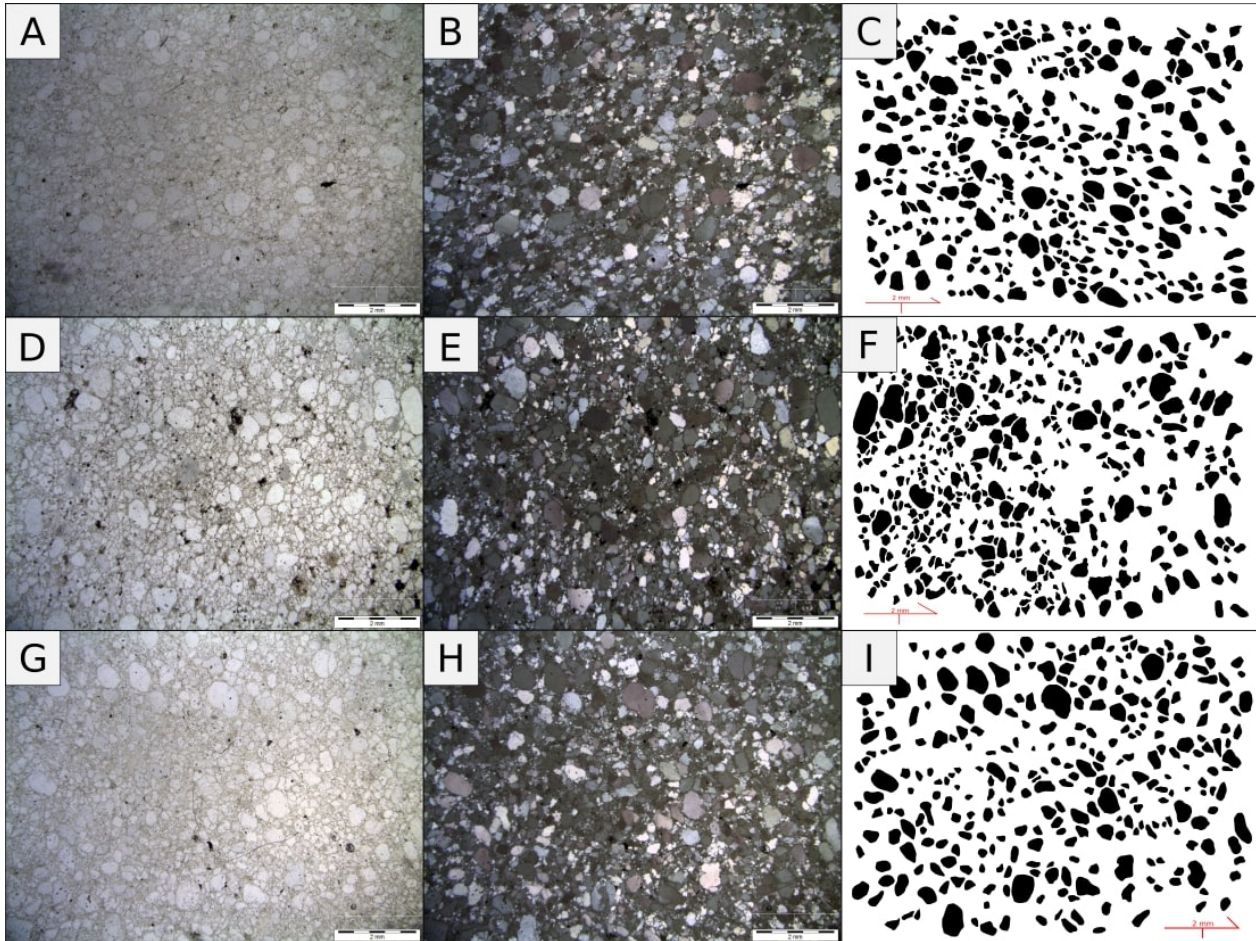

Figure 12: A,D,G: Polarized light microphotograph of the thin sections of planes AC, AB and BC of sample NER-07, respectively. **B, E, H:** Cross-Polarized light microphotograph of the thin sections of planes AC, AB and BC from sample NER-07, respectively. **C, F, I:** Single quartz grain digitized for SPO analysis of planes AC, AB and BC from sample NER-07.

	CD-07-A	CD-07-B	CD-07-C
	n = 247; R = 1.641	n = 238; R = 1.341	n = 335; R = 1.247
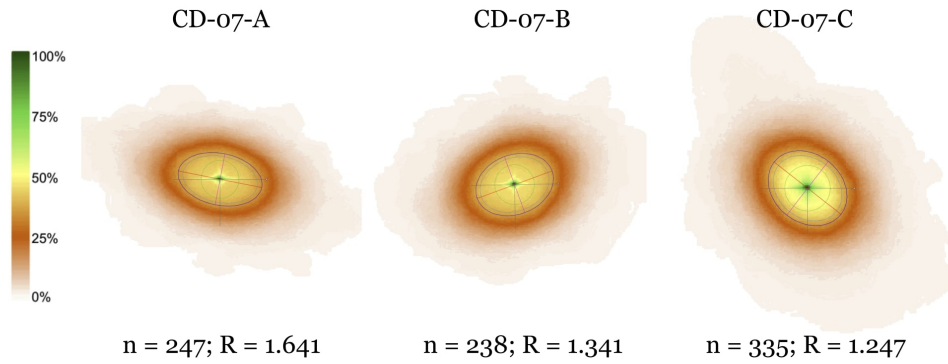
Figure 13: Shape preferred orientation ellipse of sample NER-07.
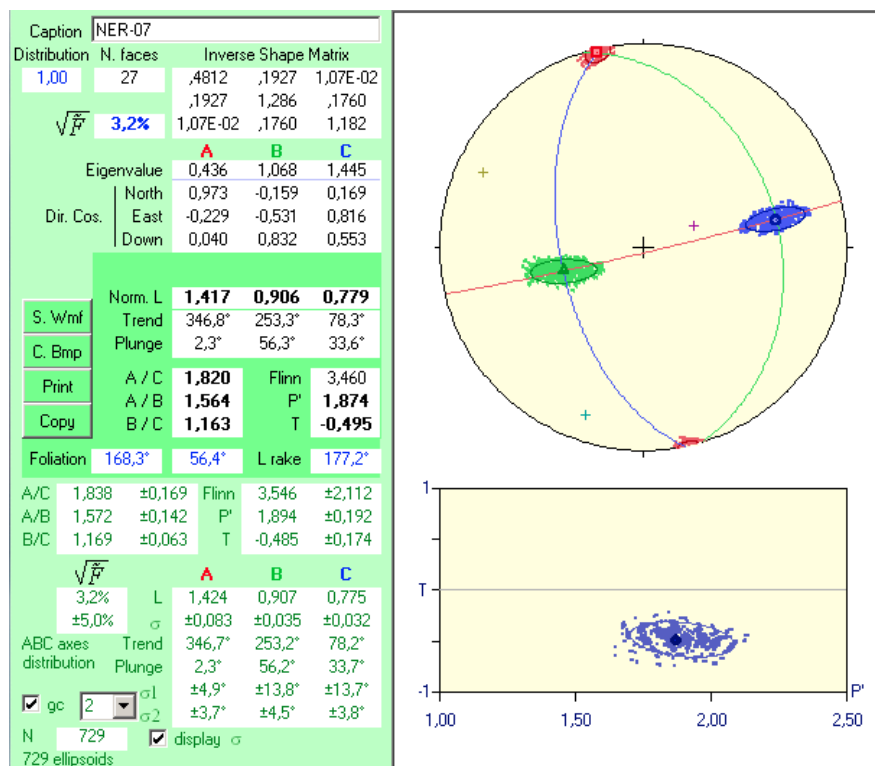
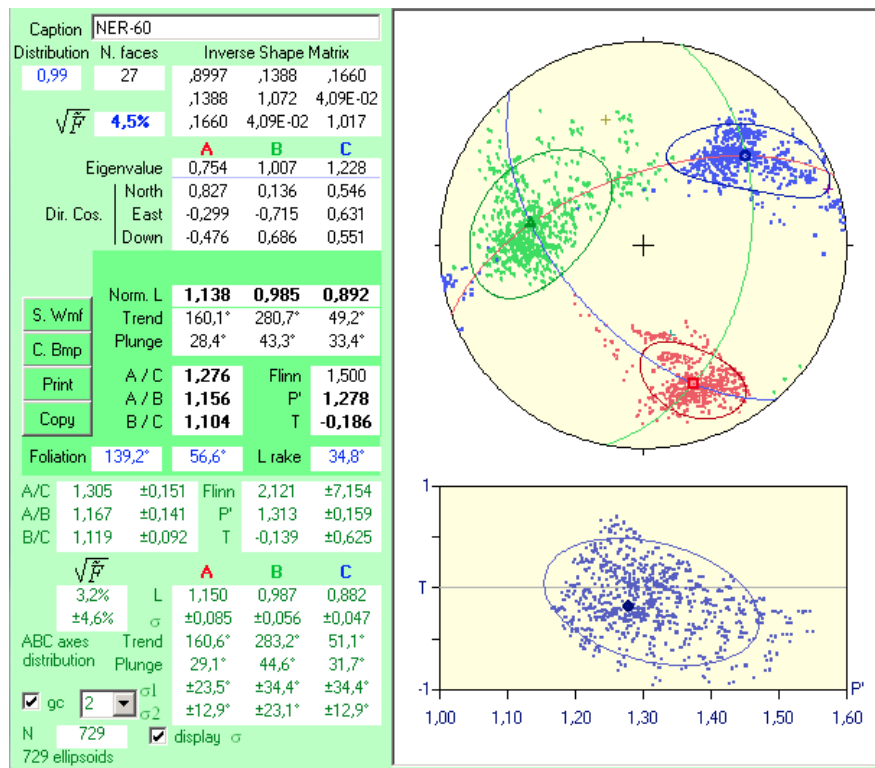**Figure 14:** Best-fit ellipsoid parameters from sample NER-07. Results direct from the program ELLIPSOID screen.

Sample NER-46 is a very fine-grained, highly foliated metaquartzarenite with a high degree of sorting. The development of a preferred orientation coincides with the direction of regional slaty cleavage.
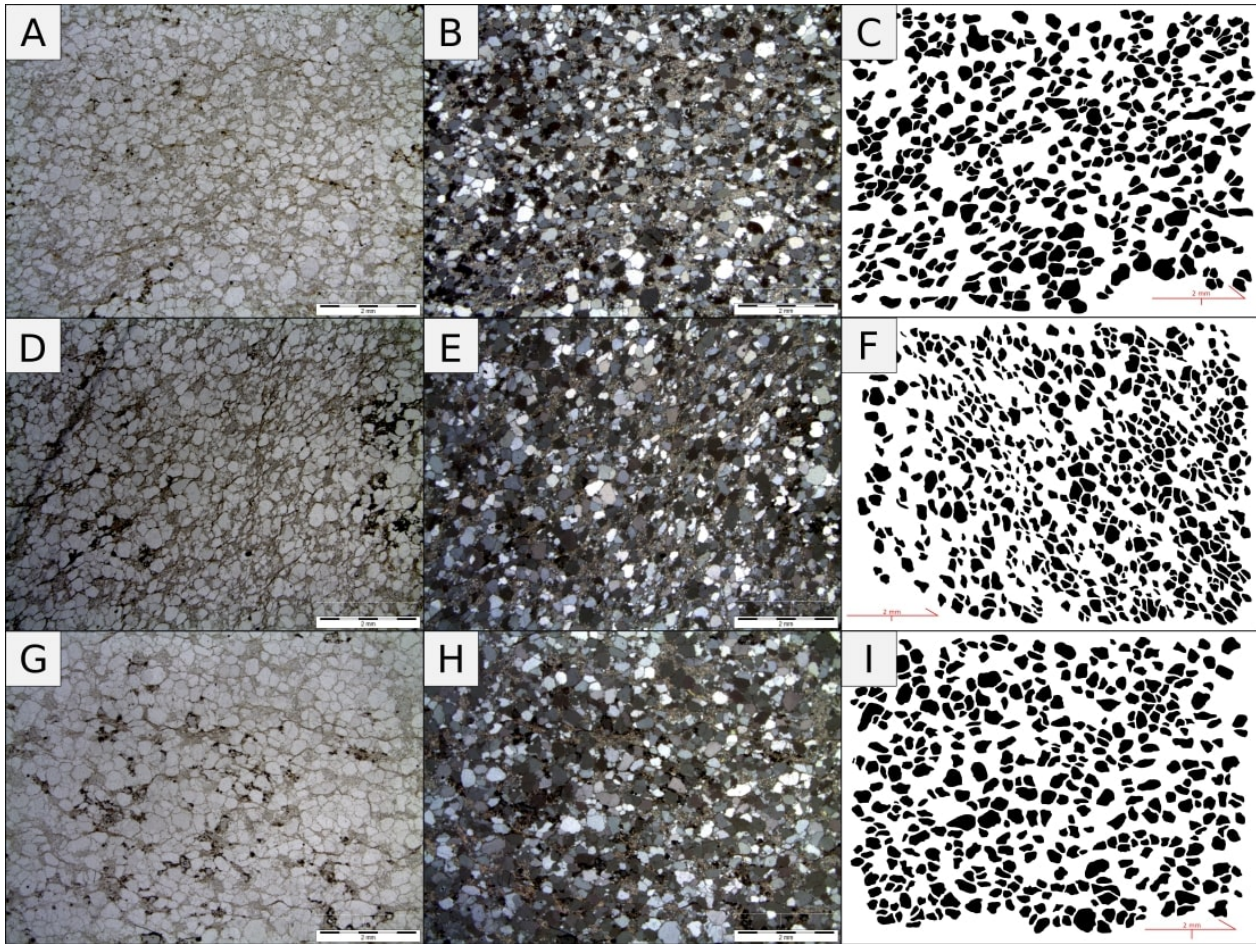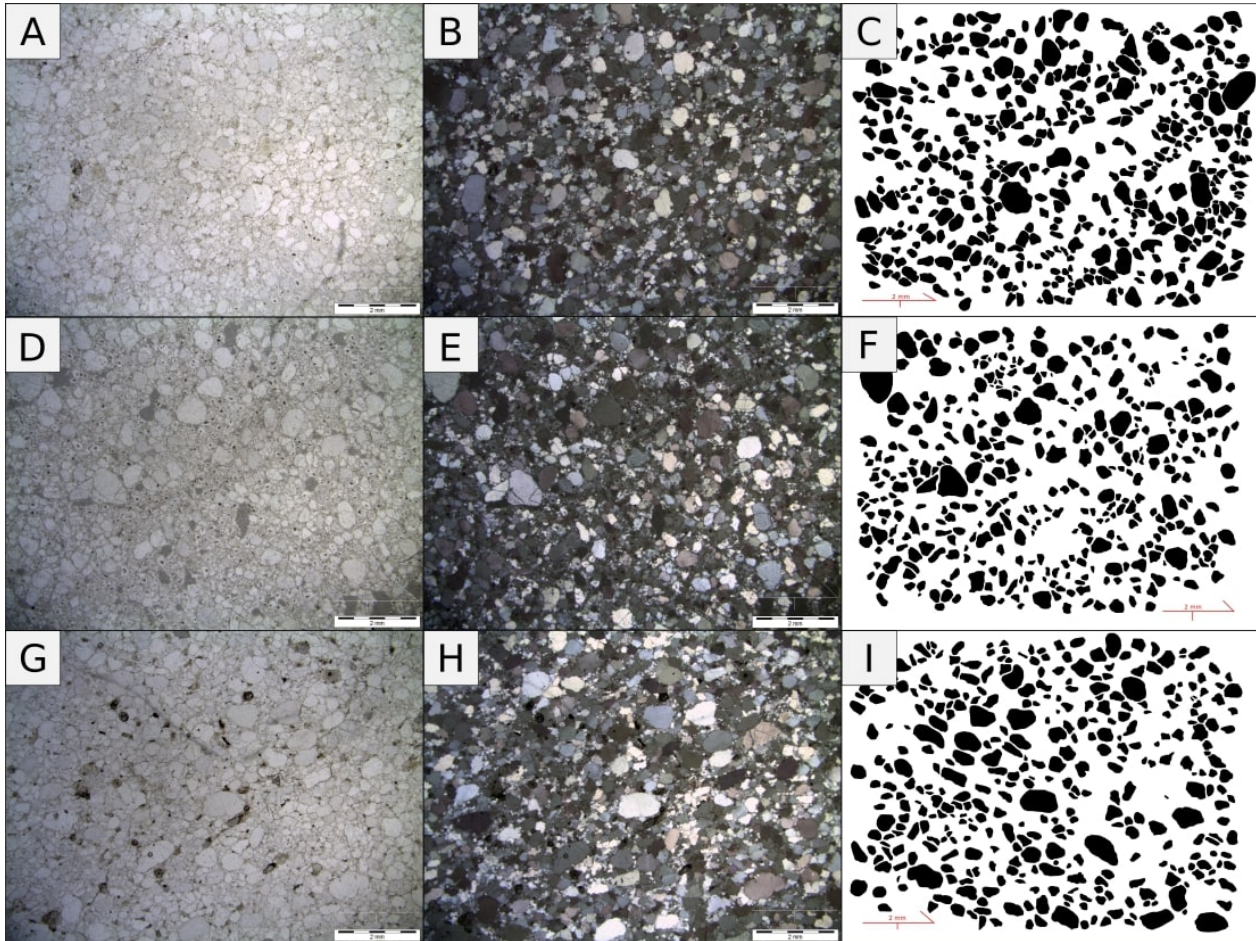

Figure 15: A,D,G: Polarized light microphotograph of the thin sections of planes AC, AB and BC of sample NER-46, respectively. **B, E, H:** Cross-Polarized light microphotograph of the thin sections of planes AC, AB and BC from sample NER-46, respectively. **C, F, I:** Single quartz grain digitized for SPO analysis of planes AC, AB and BC from sample NER-46.

CD-46-A   CD-46-B   CD-46-C

n = 490; R = 1.299   n = 621; R = 1.317   n = 410; R = 1.205
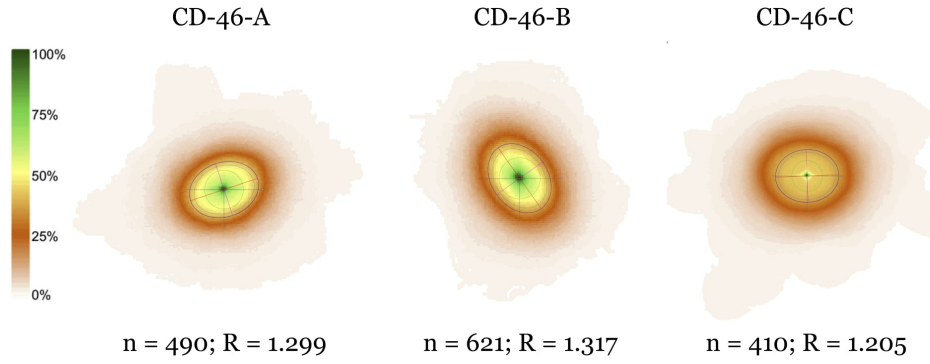
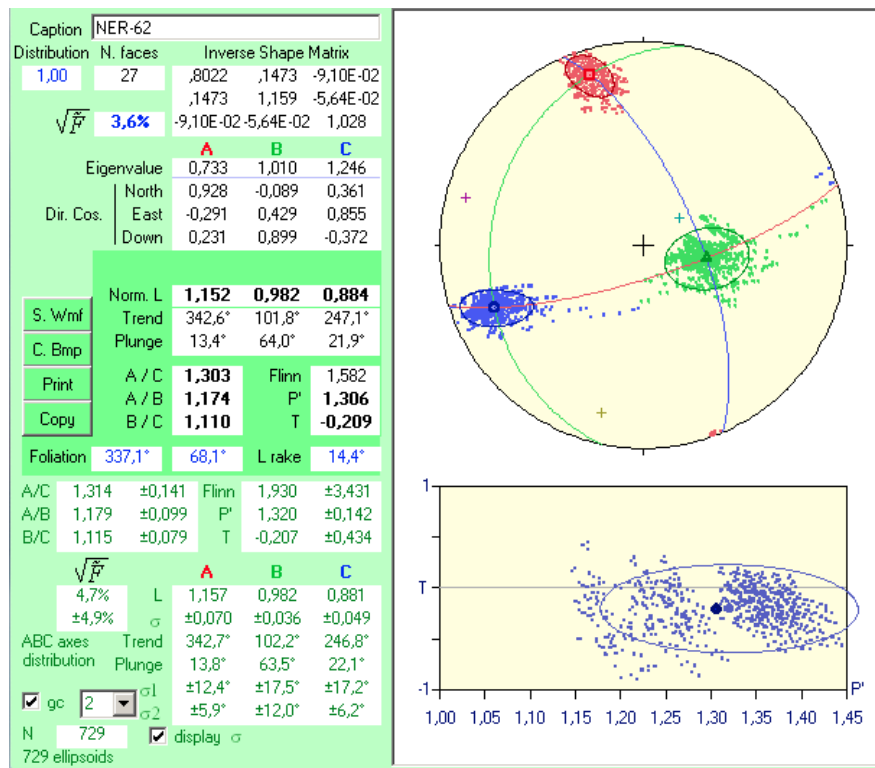**Figure 16:** Shape preferred orientation ellipse of sample NER-46.
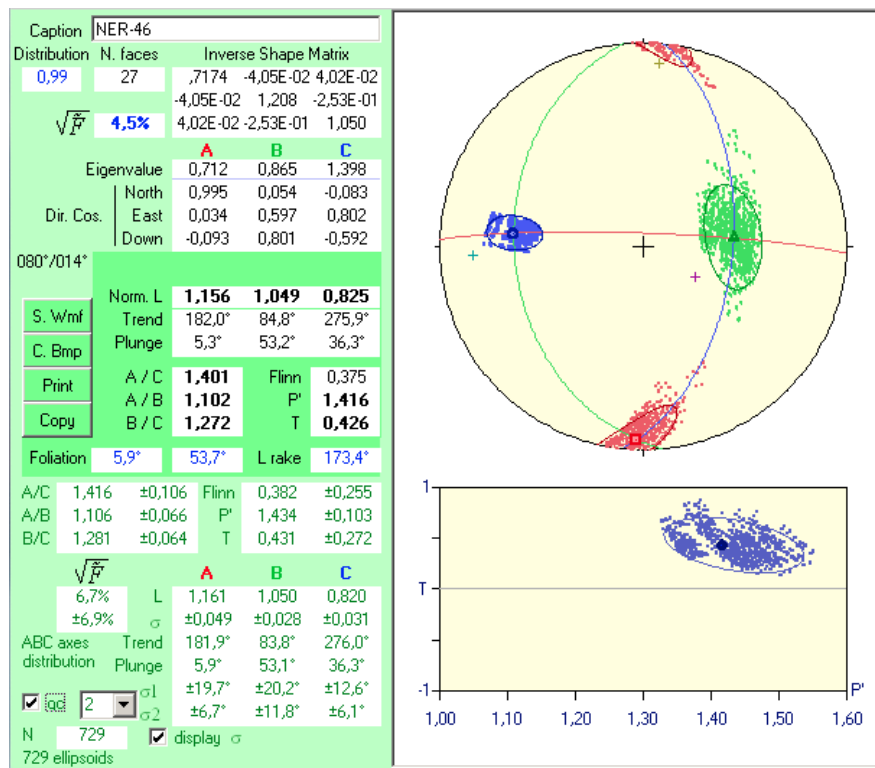
Figure 17: Best-fit ellipsoid parameters from sample NER-46. Results direct from the program ELLIPSOID screen.

Sample NER-53 is a fine- to medium-grained, inequigranular, poorly sorted sandstone with some coarse quartz grains. It marks the contact between the Boqueirão Formation and the Serra da Garapa Formation.
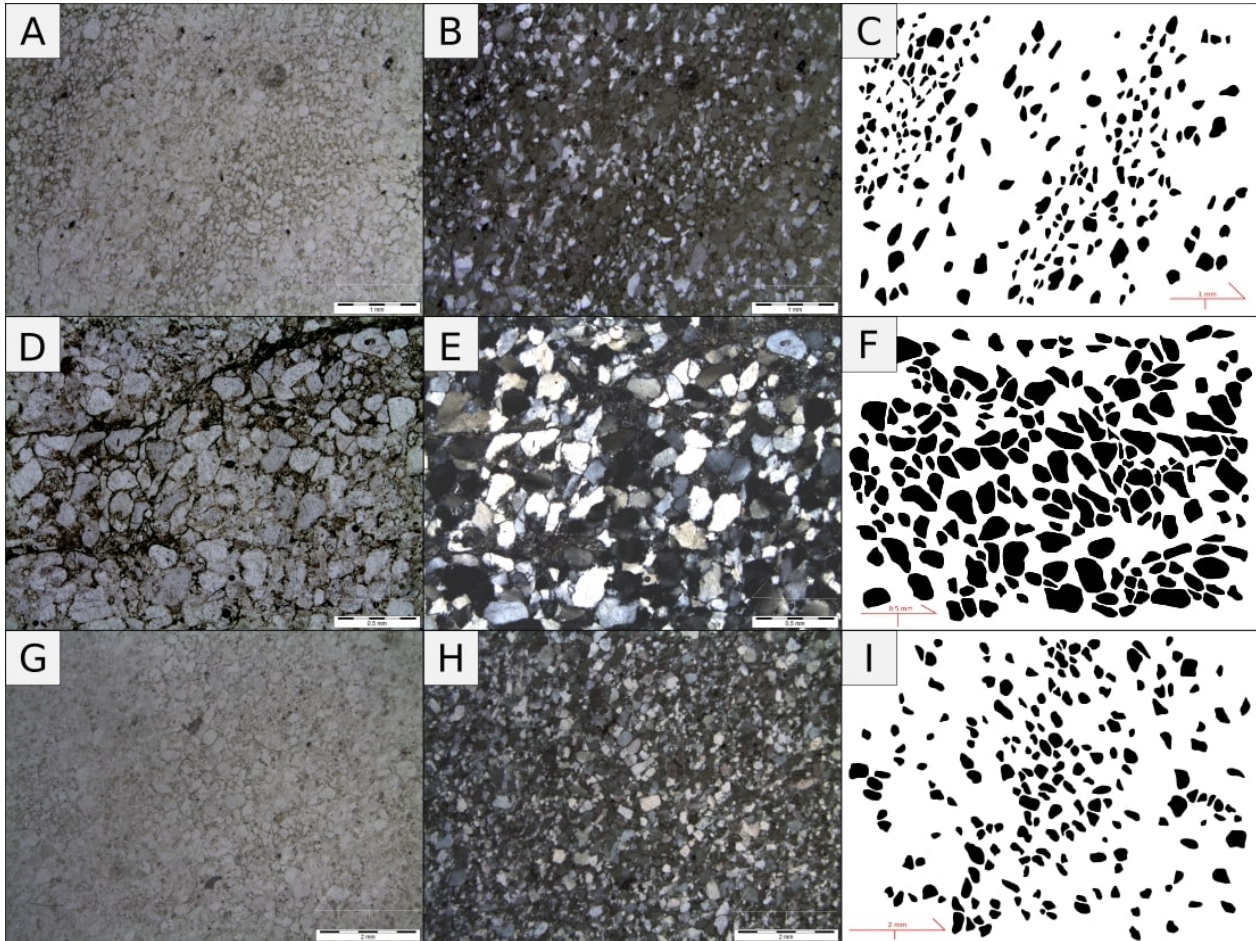

Figure 18: A,D,G: Polarized light microphotograph of the thin sections of planes AC, AB and BC of sample NER-53, respectively. **B, E, H:** Cross-Polarized light microphotograph of the thin sections of planes AC, AB and BC from sample NER-53, respectively. **C, F, I:** Single quartz grain digitized for SPO analysis of planes AC, AB and BC from sample NER-53.

CD-53-A   CD-53-B   CD-53-C

n = 400; R = 1.077   n = 307; R = 1.456   n = 300; R = 1.318
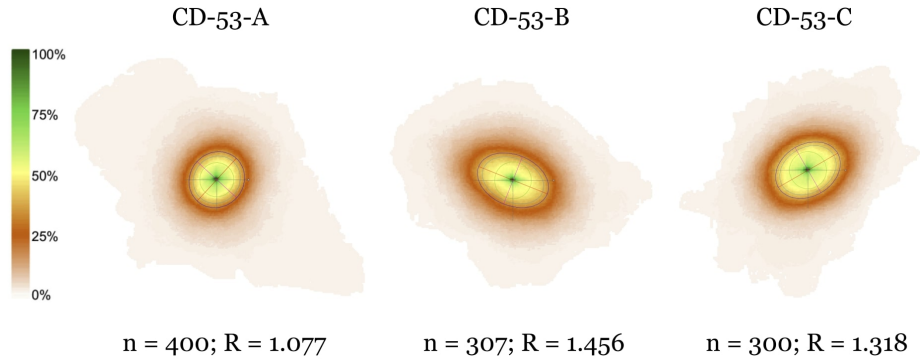
Figure 19: Shape preferred orientation ellipse of sample NER-53.
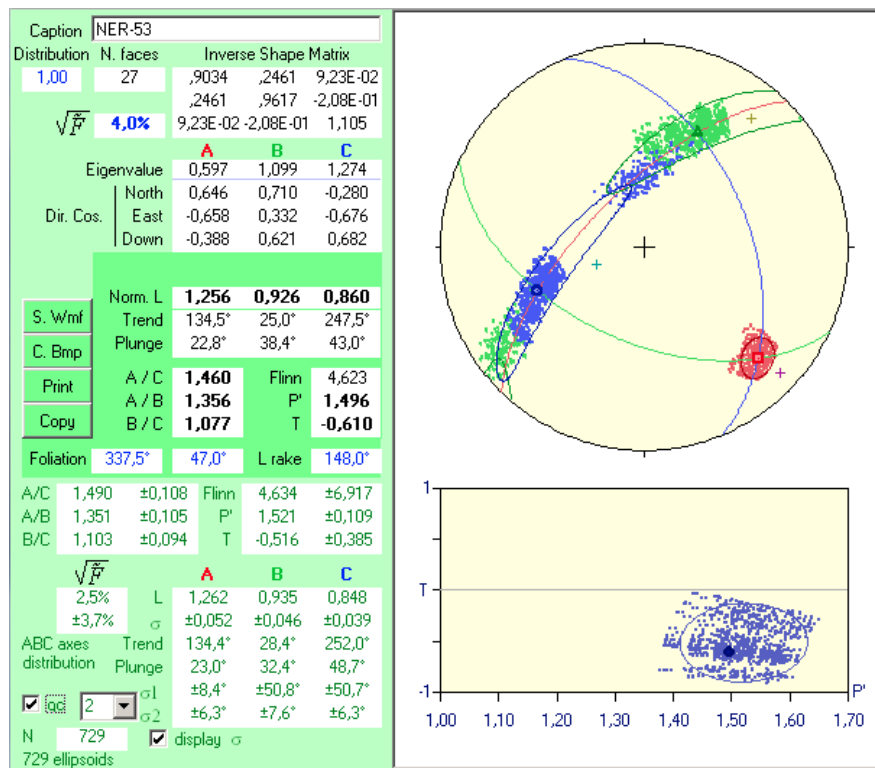
Figure 20: Best-fit ellipsoid parameters from sample NER-53. Results direct from the program ELLIPSOID screen.

Sample NER-56 is an inequigranular, poorly sorted metaquartzarenite with fine to medium grains and an arkosic matrix.

Figure 21: A,D,G: Polarized light microphotograph of the thin sections of planes AC, AB and BC of sample NER-56, respectively. **B, E, H:** Cross-Polarized light microphotograph of the thin sections of planes AC, AB and BC from sample NER-56, respectively. **C, F, I:** Single quartz grain digitized for SPO analysis of planes AC, AB and BC from sample NER-56.

CD-56-A	CD-56-B	CD-56-C
n = 322; R = 1.293	n = 330; R = 1.450	n = 284; R = 1.408
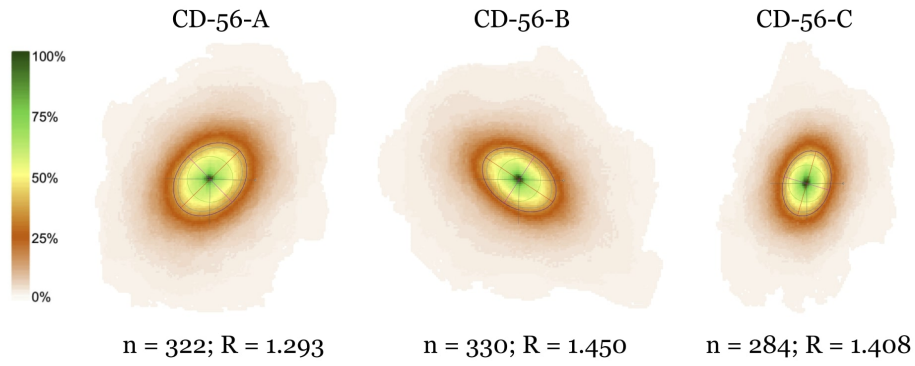
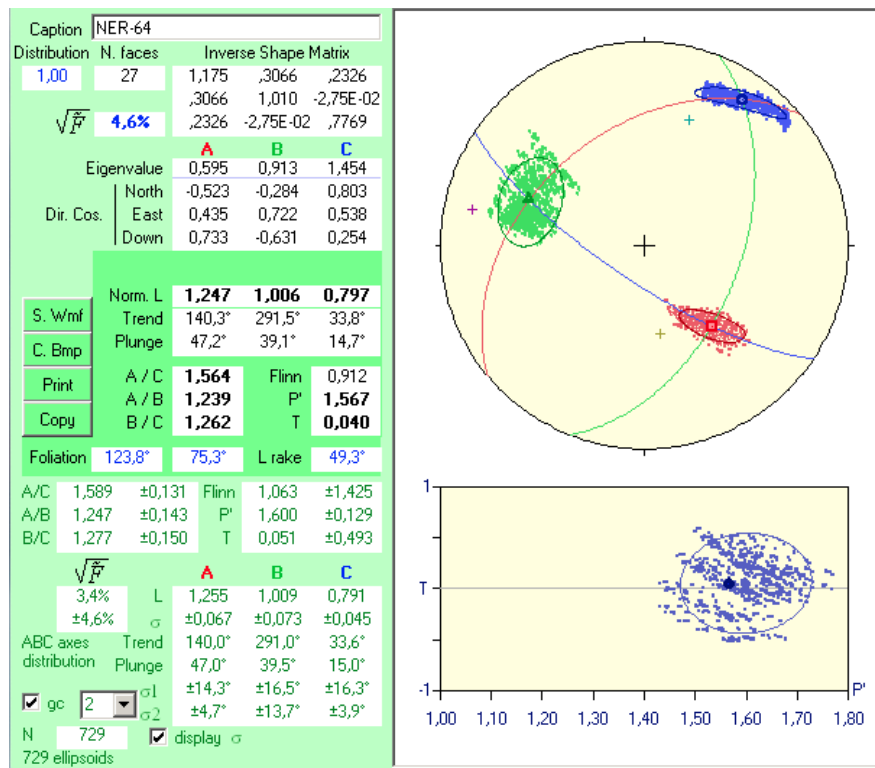**Figure 22:** Shape preferred orientation ellipse of sample NER-56.
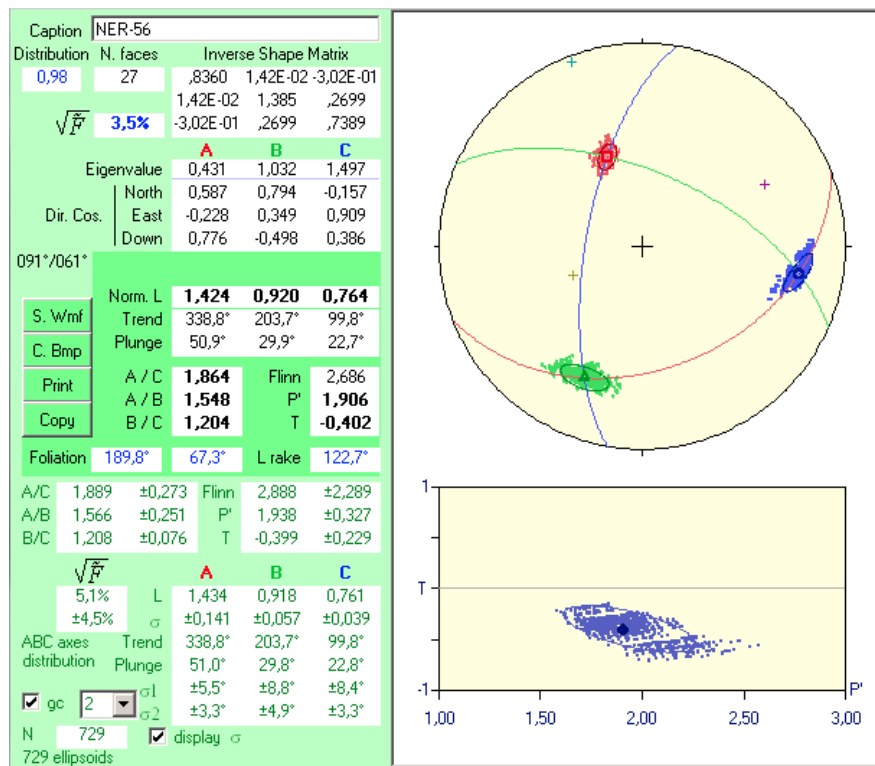
Figure 23: Best-fit ellipsoid parameters from sample NER-56. Results direct from the program ELLIPSOID screen.

Sample NER-57 is a medium- to coarse-grained, inequigranular metaquartzarenite with quartz grains larger than 2mm. The rock is generally poorly sorted and becomes finer in some levels. It contains kaolin in portions of altered matrix.
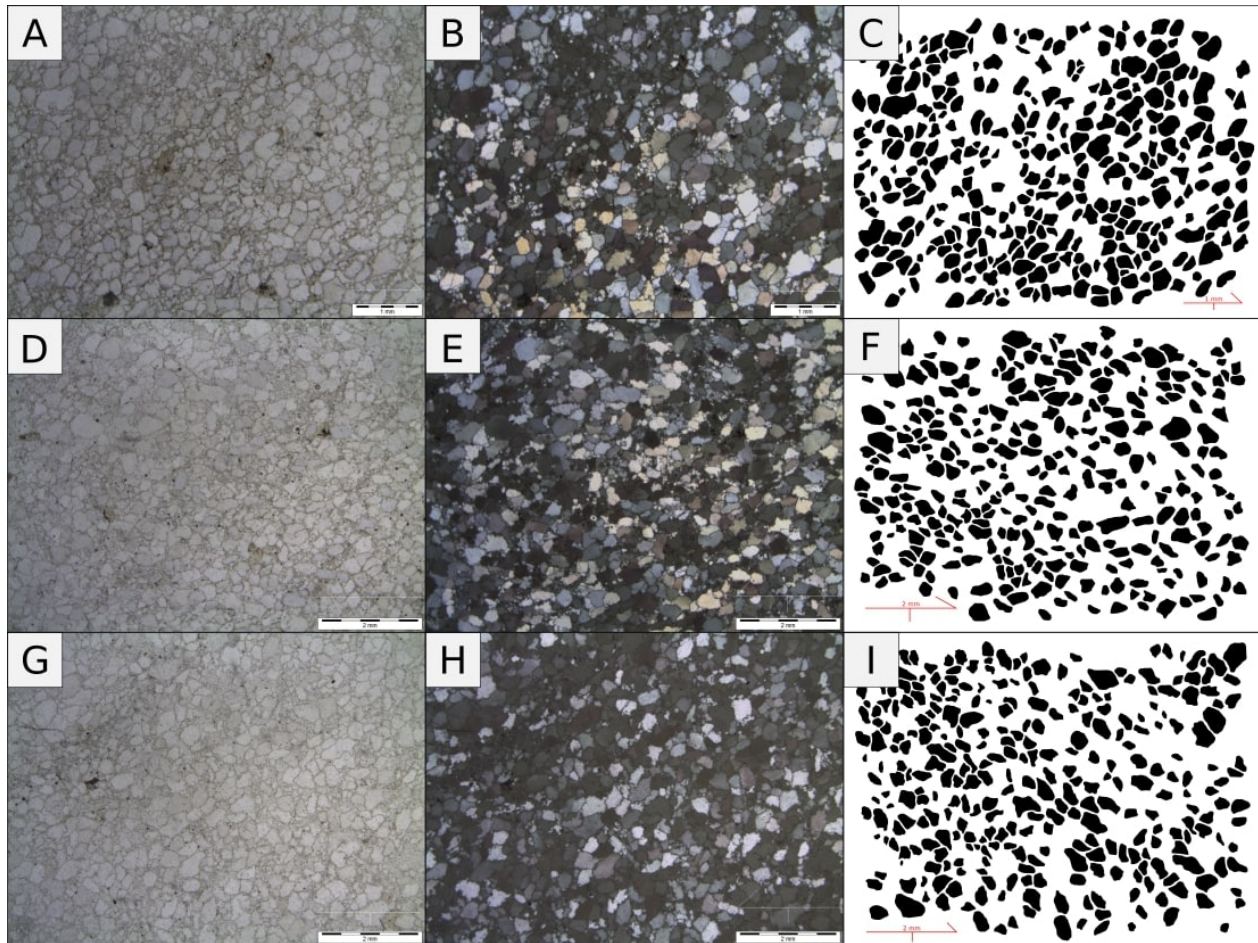

Figure 24: A,D,G: Polarized light microphotograph of the thin sections of planes AC, AB and BC of sample NER-57, respectively. **B, E, H:** Cross-Polarized light microphotograph of the thin sections of planes AC, AB and BC from sample NER-57, respectively. **C, F, I:** Single quartz grain digitized for SPO analysis of planes AC, AB and BC from sample NER-57.

	CD-57-A	CD-57-B	CD-57-C
	n = 371; R = 1.244	n = 415; R = 1.226	n = 309; R = 1.142
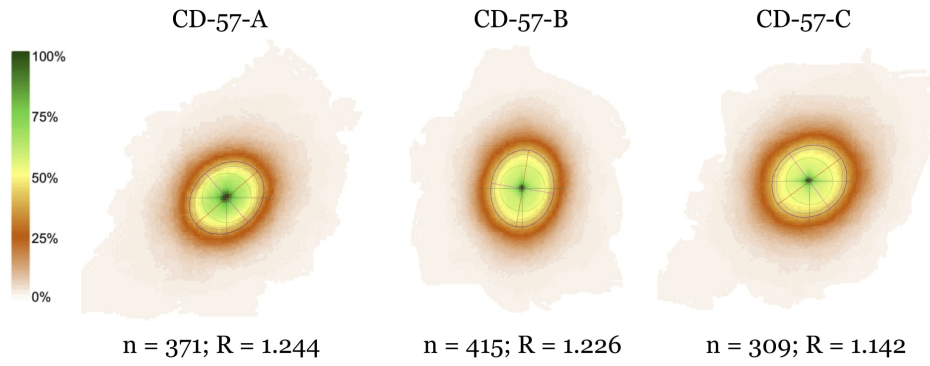
Figure 25: Shape preferred orientation ellipse of sample NER-57.
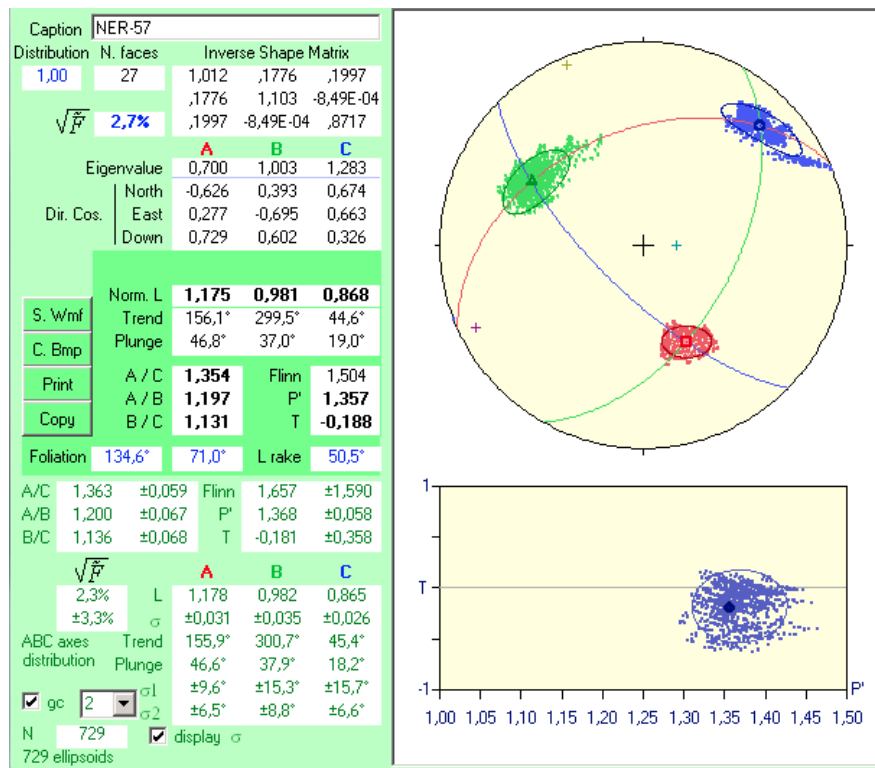
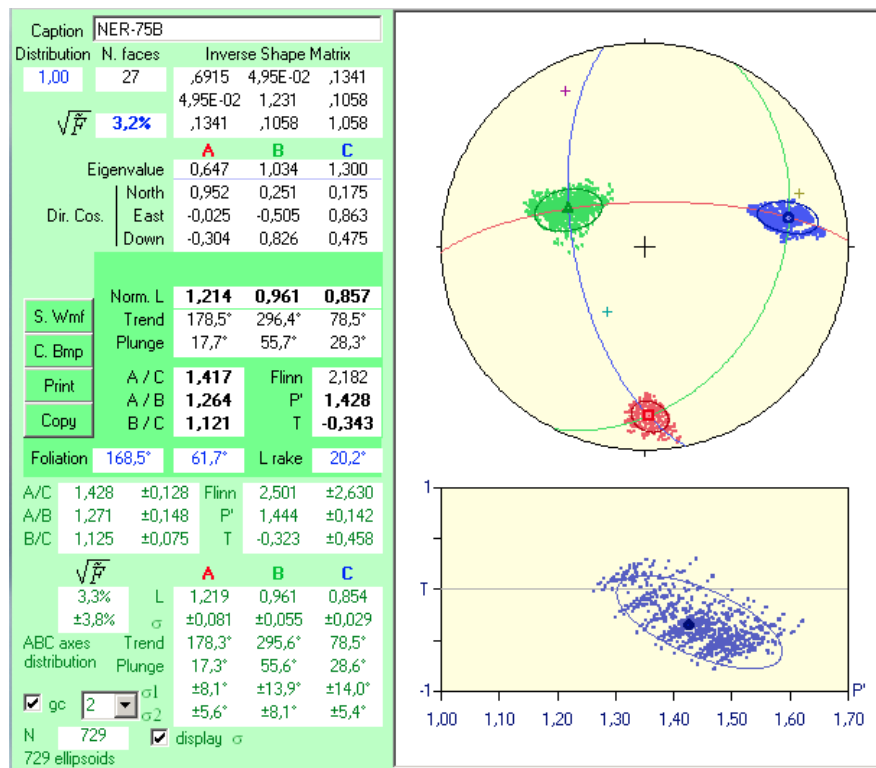**Figure 26:** Best-fit ellipsoid parameters from sample NER-57. Results direct from the program ELLIPSOID screen.

Sample NER-60 is an inequigranular metaquartzarenite ranging from fine to very coarse, with sub-angular quartz grains.
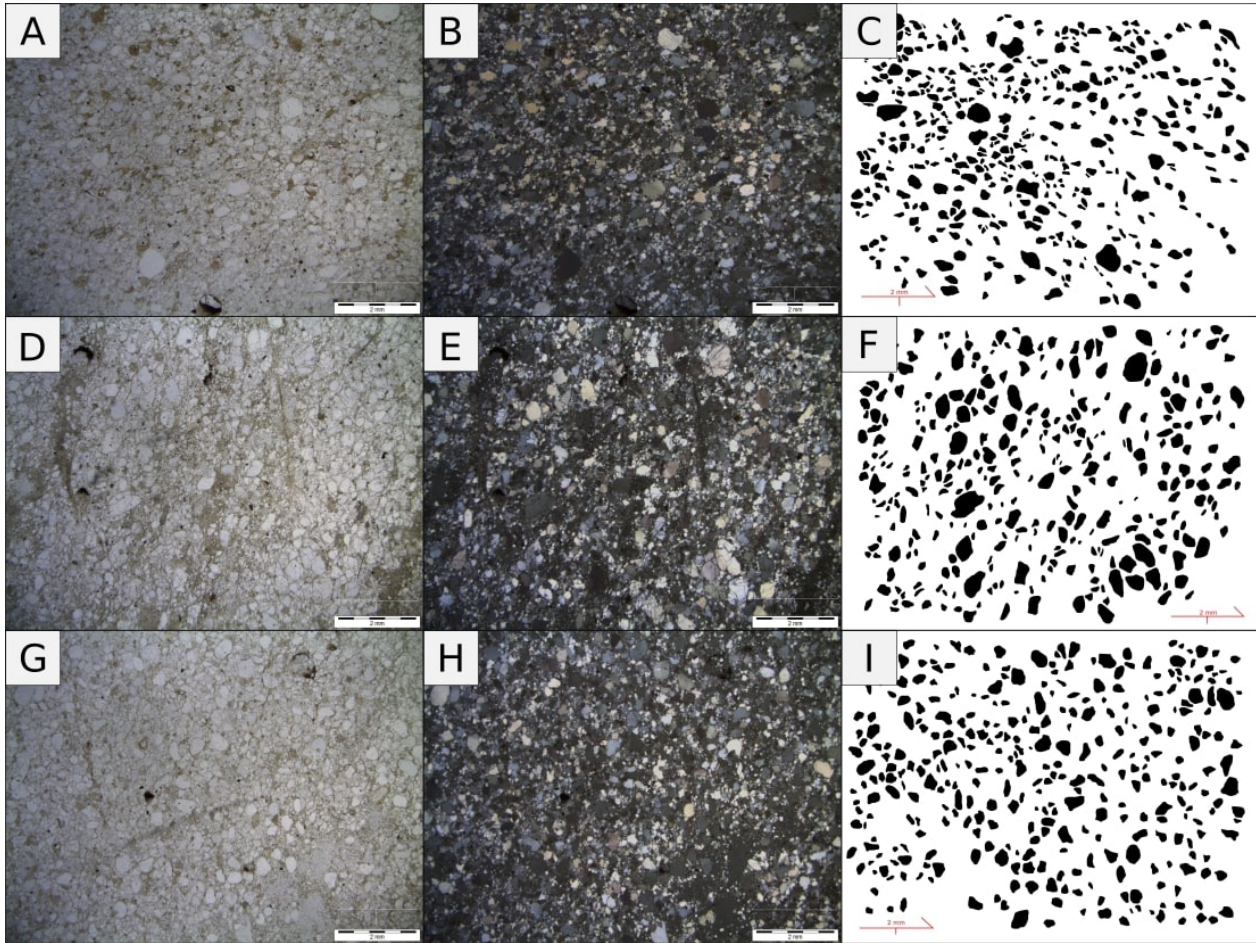

Figure 27: A,D,G: Polarized light microphotograph of the thin sections of planes AC, AB and BC of sample NER-60, respectively. **B, E, H:** Cross-Polarized light microphotograph of the thin sections of planes AC, AB and BC from sample NER-60, respectively. **C, F, I:** Single quartz grain digitized for SPO analysis of planes AC, AB and BC from sample NER-60.
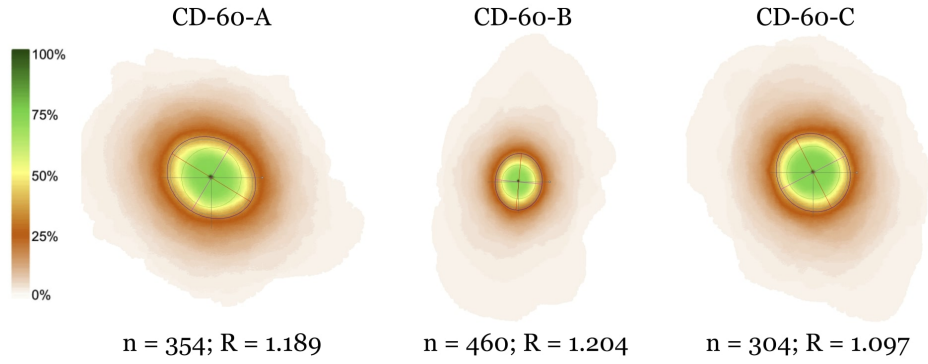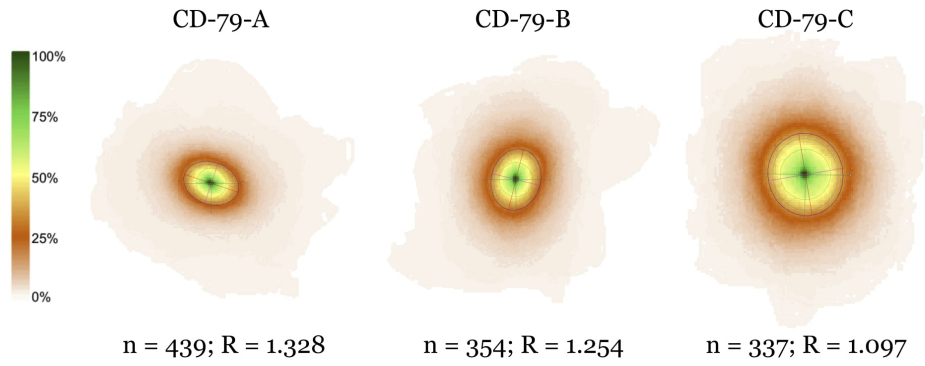
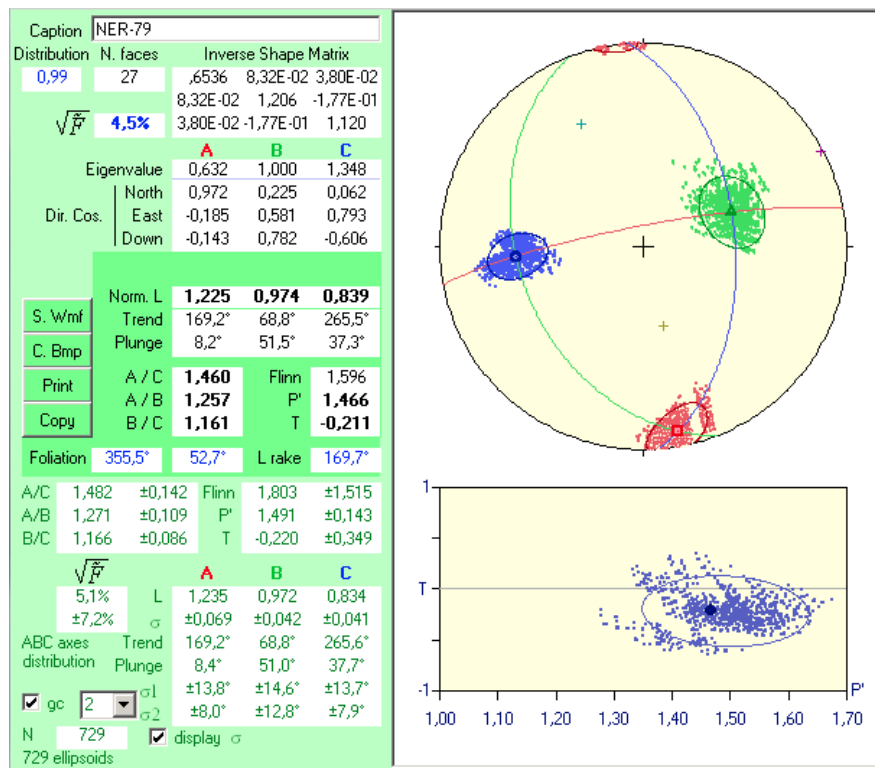**Figure 28:** Shape preferred orientation ellipse of sample NER-60.

Figure 29: Best-fit ellipsoid parameters from sample NER-60. Results direct from the program ELLIPSOID screen.

NER-62

Sample NER-62 is the same inequigranular metaquartzarenite ranging from fine to very coarse, with sub-angular quartz grains, as seen in sample NER-60.

Figure 30: A,D,G: Polarized light microphotograph of the thin sections of planes AC, AB and BC of sample NER-62, respectively. **B, E, H:** Cross-Polarized light microphotograph of the thin sections of planes AC, AB and BC from sample NER-62, respectively. **C, F, I:** Single quartz grain digitized for SPO analysis of planes AC, AB and BC from sample NER-62.

CD-62-A CD-62-B CD-62-C

n = 441; R = 1.089   n = 377; R = 1.045   n = 366; R = 1.282
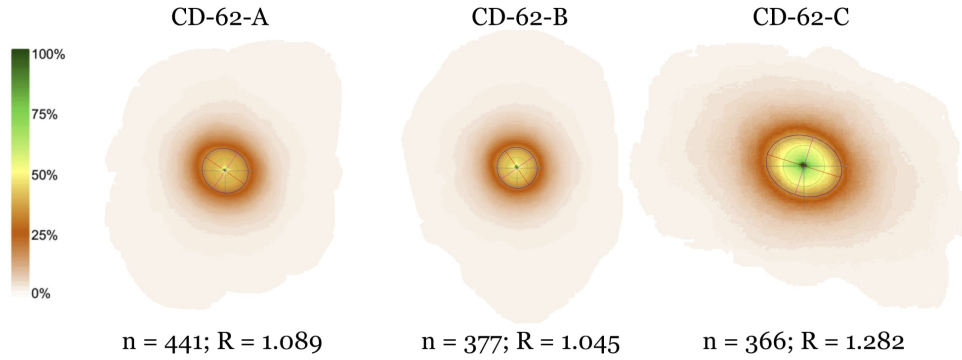
Figure 31: Shape preferred orientation ellipse of sample NER-62.

Figure 32: Best-fit ellipsoid parameters from sample NER-62. Results direct from the program ELLIPSOID screen.

Sample NER-64 displays a centimeter-scale intercalation, approximately 15cm thick, of quartz-rich siltstone and well lithified fine-grained quartzite with dark brown-colored layers.

Figure 33: A,D,G: Polarized light microphotograph of the thin sections of planes AC, AB and BC of sample NER-64, respectively. **B, E, H:** Cross-Polarized light microphotograph of the thin sections of planes AC, AB and BC from sample NER-64, respectively. **C, F, I:** Single quartz grain digitized for SPO analysis of planes AC, AB and BC from sample NER-64.
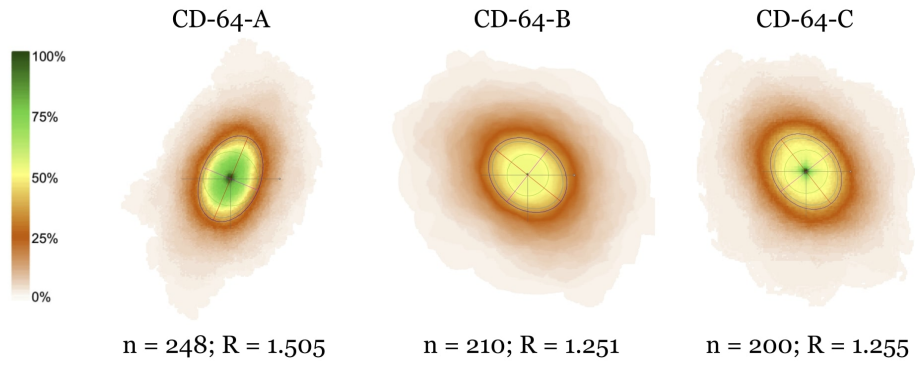
Figure 34: Shape preferred orientation ellipse of sample NER-64.

Figure 35: Best-fit ellipsoid parameters from sample NER-64. Results direct from the program ELLIPSOID screen.

NER-75B

Sample NER-75B is a medium- to coarse-grained quartz-rich meta-arenite, poorly sorted, with subangular to subrounded grains.
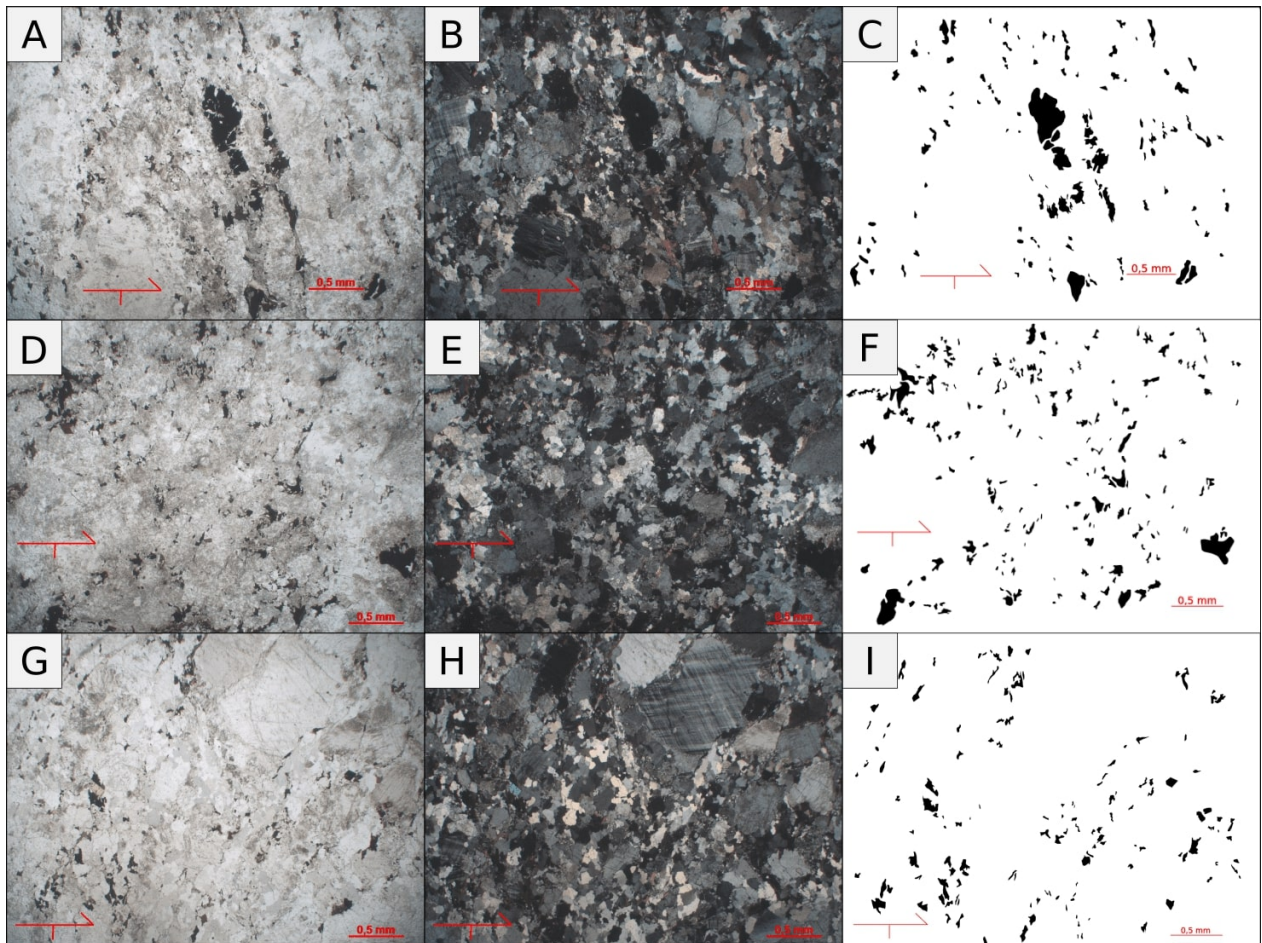

Figure 36: A,D,G: Polarized light microphotograph of the thin sections of planes AC, AB and BC of sample NER-75B, respectively. **B, E, H:** Cross-Polarized light microphotograph of the thin sections of planes AC, AB and BC from sample NER-75B, respectively. **C, F, I:** Single quartz grain digitized for SPO analysis of planes AC, AB and BC from sample NER-75B.

CD-75B-A   CD-75B-B   CD-75B-C

n = 312; R = 1.265   n = 305; R = 1.261   n = 304; R = 1.212
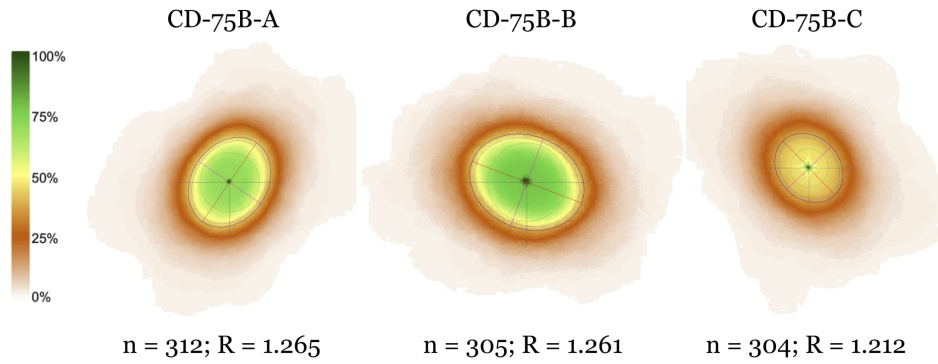
Figure 37: Shape preferred orientation ellipse of sample NER-75B.

Figure 38: Best-fit ellipsoid parameters from sample NER-75B. Results direct from the program ELLIPSOID screen.

Sample NER-79 is a fine- to medium-grained inequigranular quartzite with grains that still preserve the original sedimentary texture, poorly sorted, and with subangular to subrounded grains.

Figure 39: A,D,G: Polarized light microphotograph of the thin sections of planes AC, AB and BC of sample NER-79, respectively. **B, E, H:** Cross-Polarized light microphotograph of the thin sections of planes AC, AB and BC from sample NER-79, respectively. **C, F, I:** Single quartz grain digitized for SPO analysis of planes AC, AB and BC from sample NER-79.

CD-79-A   CD-79-B   CD-79-C

n = 439; R = 1.328   n = 354; R = 1.254   n = 337; R = 1.097

Figure 40: Shape preferred orientation ellipse of sample NER-79.

Figure 41: Best-fit ellipsoid parameters from sample NER-79. Results direct from the program ELLIPSOID screen.

8.4 *Finite Strain data - Western Chapada Diamantina*

For the supplementary data of 2D strain analysis, we present the Shape Preferred Orientation ellipses of each sample regarding the Western Chapada Diamantina Domain (Silva Neto et al., 2022). The results obtained by the Inertia Tensor method (Launeau & Cruden, 1998) were later used to compute the best fit ellipsoid using the using the software *ELLIPSOID* (Robin, 2002; Launeau & Robin, 2005). Finally, Table 4 summarizes the 2D strain data obtained for all samples used in this study followed by all microphotographs and computed shape preferred ellipses for all samples.

Table 4: Two Dimensional (2D) Strain Data - Shape preferred orientation ellipses for all planes used to compute best fit ellipsoids.

Sample Code	AC Plane				AB Plane				BC Plane			
	n	R_s	ϕ (°)	Strike/Dip	n	R_s	ϕ (°)	Strike/Dip	n	R_s	ϕ (°)	Strike/Dip
CD-01B	89	1.675	080.03	090/34	69	1.164	112.03	348/84	120	1.448	100.2	254/56
CD-03A	176	1.650	029.02	266/05	121	1.260	53.04	359/89	152	1.459	60.04	091/88
CD-06A	211	1.408	178.00	354/49	135	1.022	146.91	176/35	202	1.492	134.64	078/89
CD-11	237	1.350	037.47	240/80	208	1.088	132.39	159/41	176	1.214	175.4	344/48
CD-16	82	1.915	141.63	018/15	156	1.346	96.47	174/80	99	2.207	73.34	272/86
CD-23	164	1.219	123.67	242/04	405	1.218	128.14	318/88	364	1.125	112.37	046/86
CD-28	184	1.143	087.46	034/74	245	1.103	67.17	274/24	236	1.067	53.57	130/70
CD-30A	209	1.248	070.19	231/62	200	1.155	98.53	041/35	198	1.052	15.94	138/85
CD-40	150	1.146	043.03	143/82	164	1.117	131.93	237/55	158	1.133	110.67	039/40

* n is the number of quartz grains analyzed in each thin section to compute the Shape Preferred Orientation ellipse.

** Strike and Dip attitude follows the right hand rule convention (RHR) and represents the orientation of the thin section.
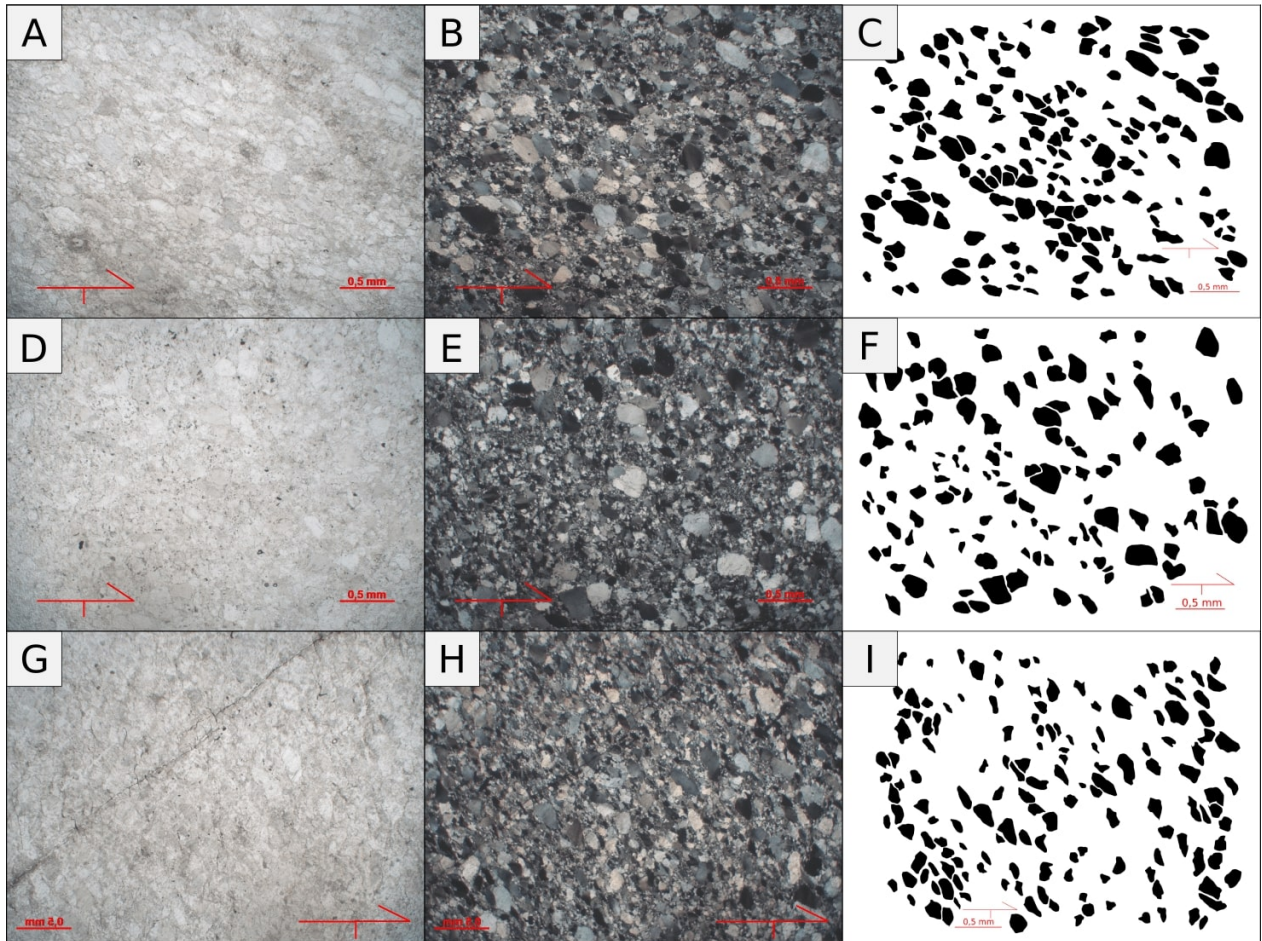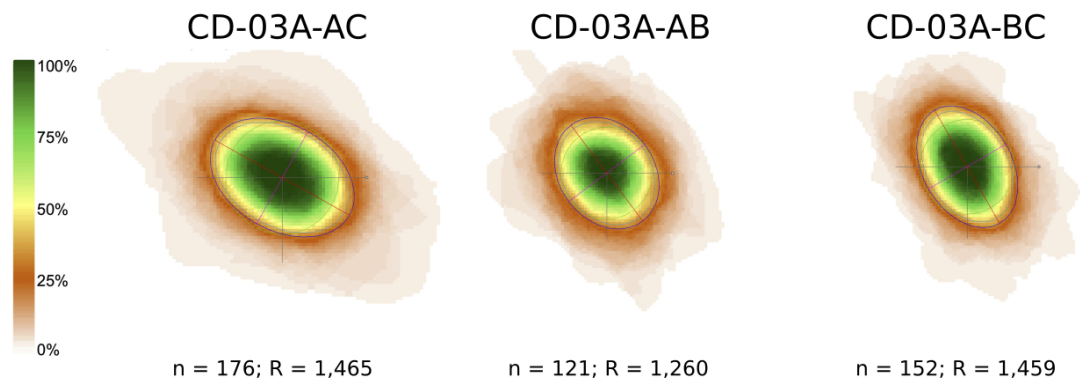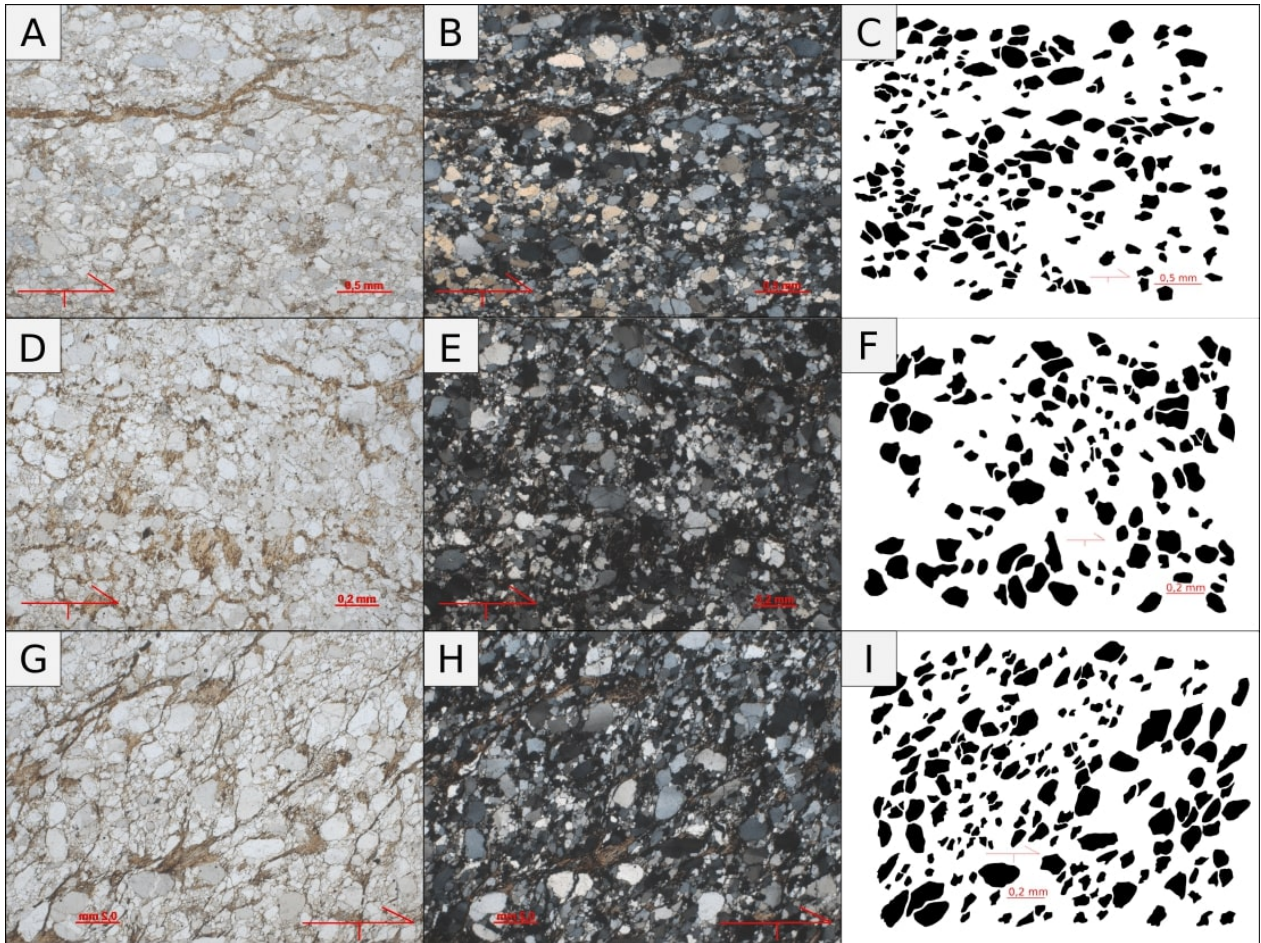
Figure 42: A,D,G: Polarized light microphotograph of the thin sections of planes AC, AB and BC of sample CD-01B, respectively. **B, E, H:** Cross-Polarized light microphotograph of the thin sections of planes AC, AB and BC from sample CD-01B, respectively. **C, F, I:** Single quartz grain digitized for SPO analysis of planes AC, AB and BC from sample CD-01B.

Sample CD-01B is a high grade metamorphic rock, composed basically by quartz, plagioclase and K-feldspar from the Gavião Complex. For this sample, opaque minerals, mainly ilmenite, were analyzed as strain markers. Sections AC and BC presented moderate to high shape ratios (R), while section AB, obtained a lower R, close to 1 Figure 43. Thin sections microphotographs used to calculate the SPO are displayed in Fig. 42. The parameters of the best-fit ellipsoid can be seen in Fig. 44.
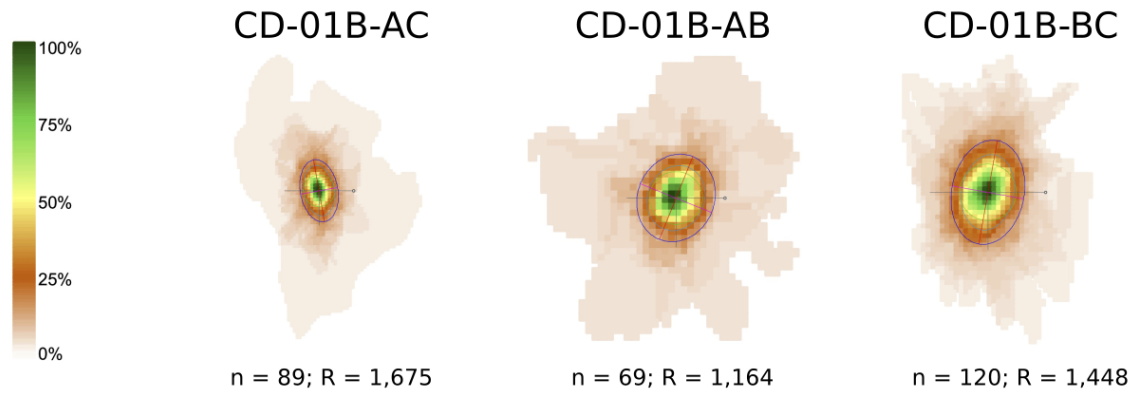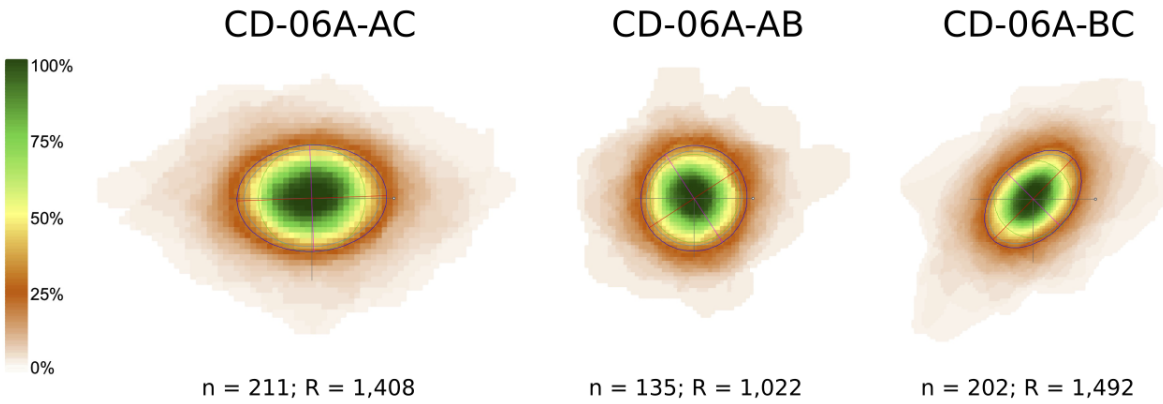
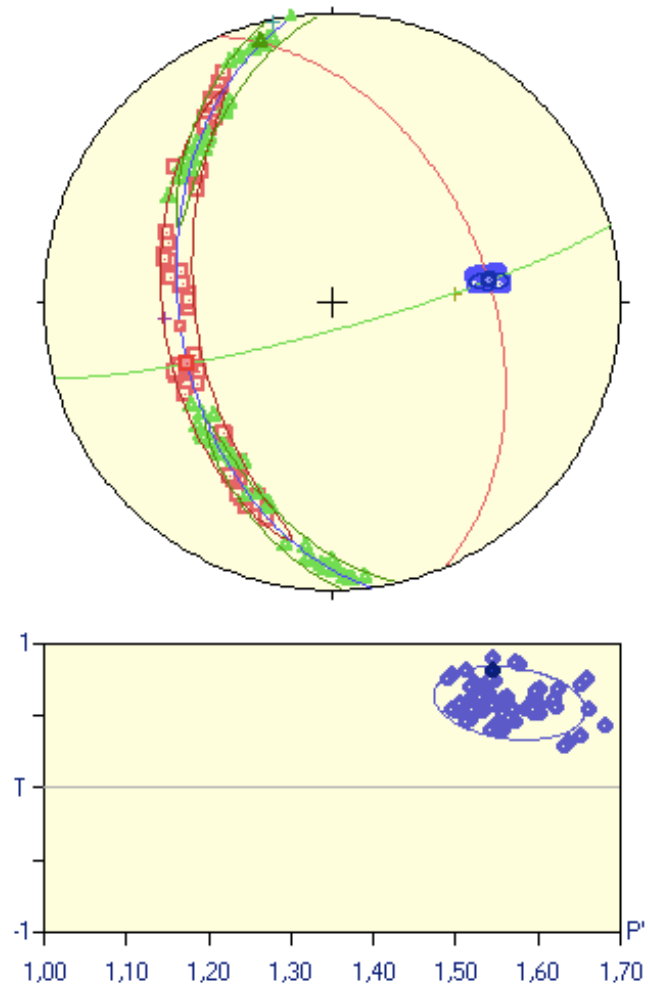**Figure 43:** Shape preferred orientation ellipse of Sample CD-01B.
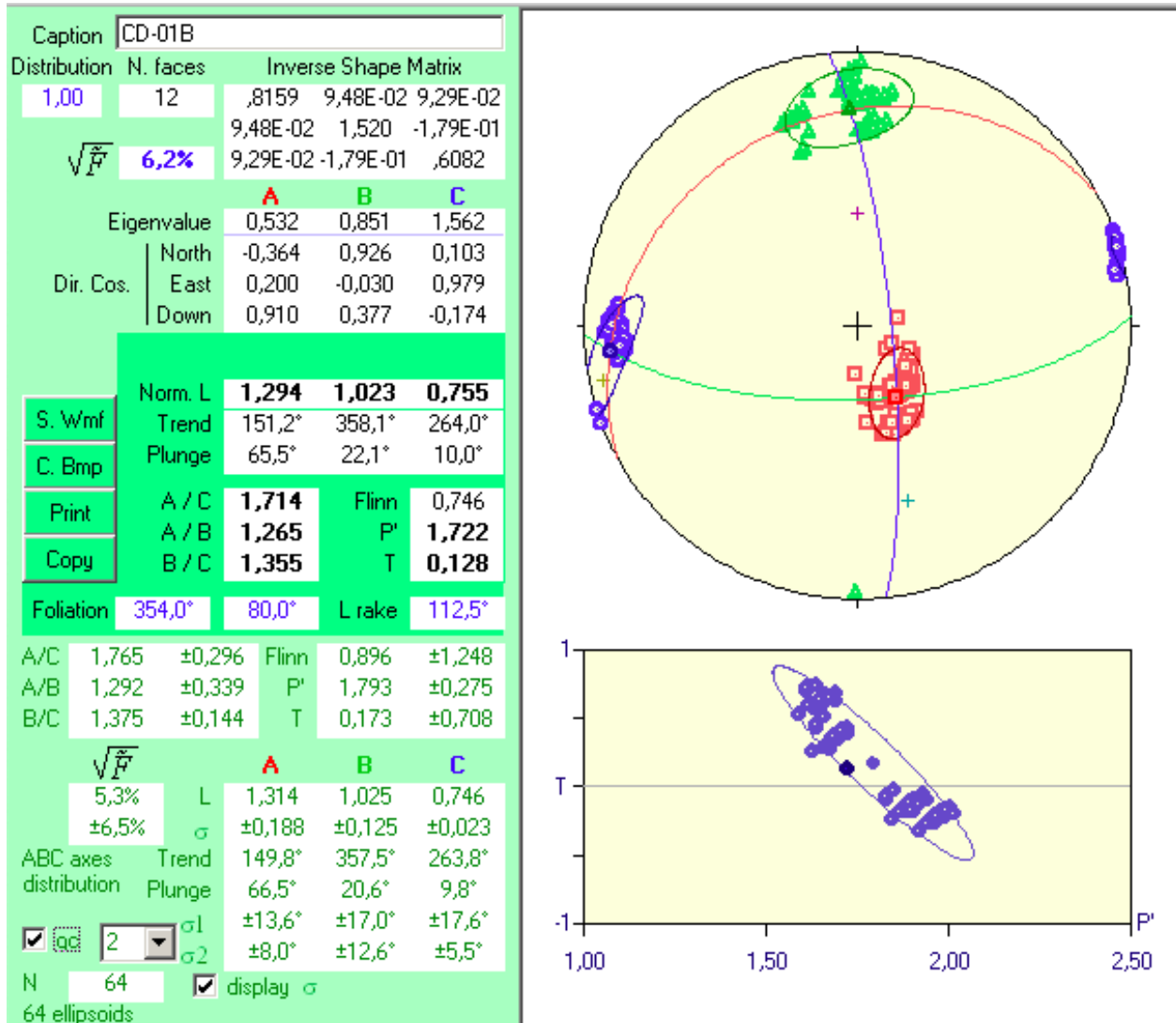
Figure 44: Best-fit ellipsoid parameters from Sample CD-01B. Results direct from the program ELLIPSOID screen.

Figure 45: A,D,G: Polarized light microphotograph of the thin sections of planes AC, AB and BC of sample CD-03A, respectively. **B, E, H:** Cross-Polarized light microphotograph of the thin sections of planes AC, AB and BC from sample CD-03A, respectively. **C, F, I:** Single quartz grain digitized for SPO analysis of planes AC, AB and BC from sample CD-03A.

The CD-03A sample is an extremely foliated metarenite, with deformation of detritic quartz grains subordinated to the main foliation from the Novo Horizonte Formation. This sample lies close to the contact between the Basement and the above mentioned Formation, marked by major thrust faults. Sections present low to intermediate shape ratio values, ranging from 1.2 to 1.4 Figure 46. The thin sections microphotographs used to calculate the SPO are displayed in Fig. 45. The parameters of the best-fit ellipsoid can be seen in Fig. 47.

Figure 46: Shape preferred orientation ellipse of sample CD-03A.
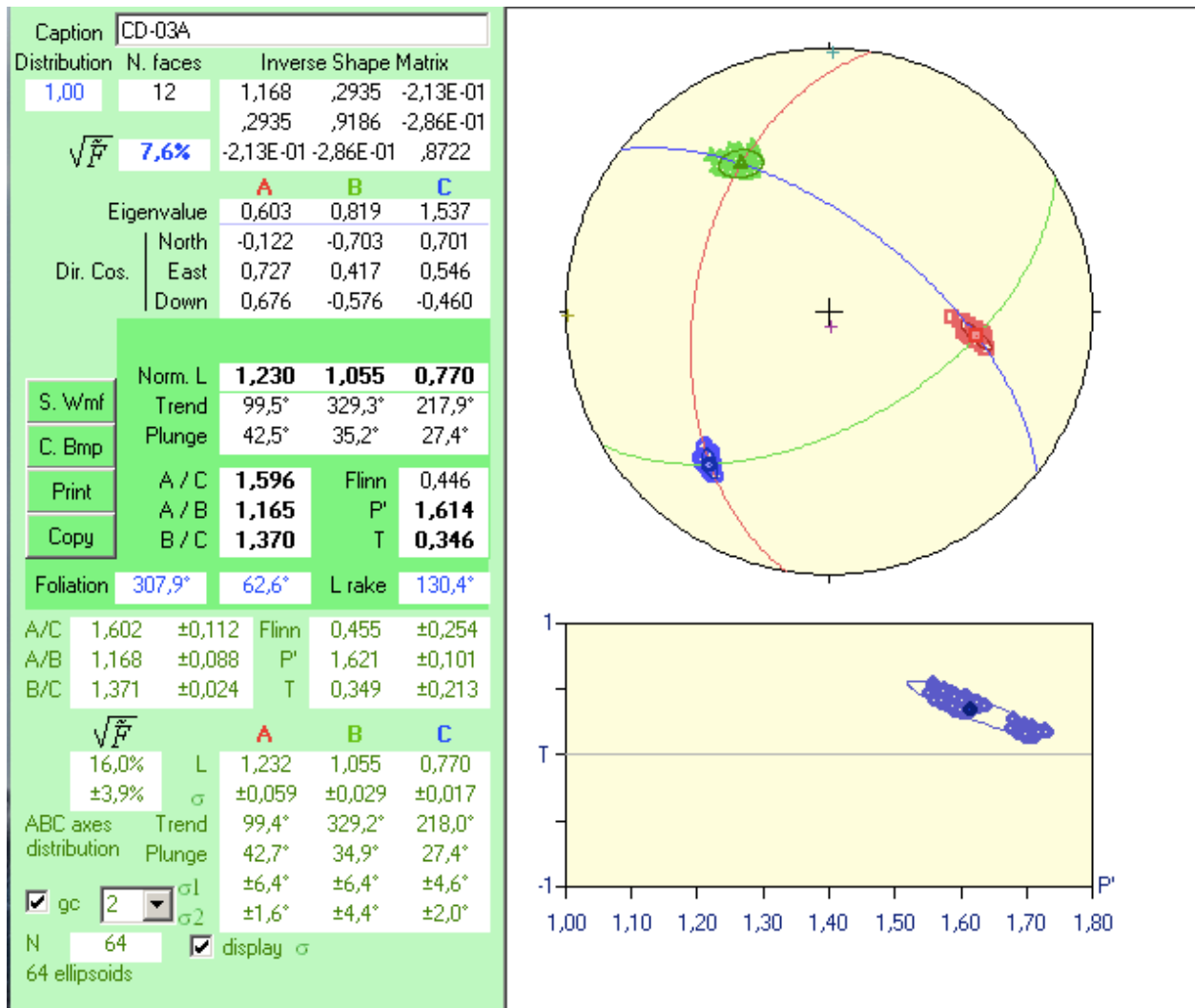
Figure 47: Best-fit ellipsoid parameters from Sample CD-03A. Results direct from the program ELLIPSOID screen.
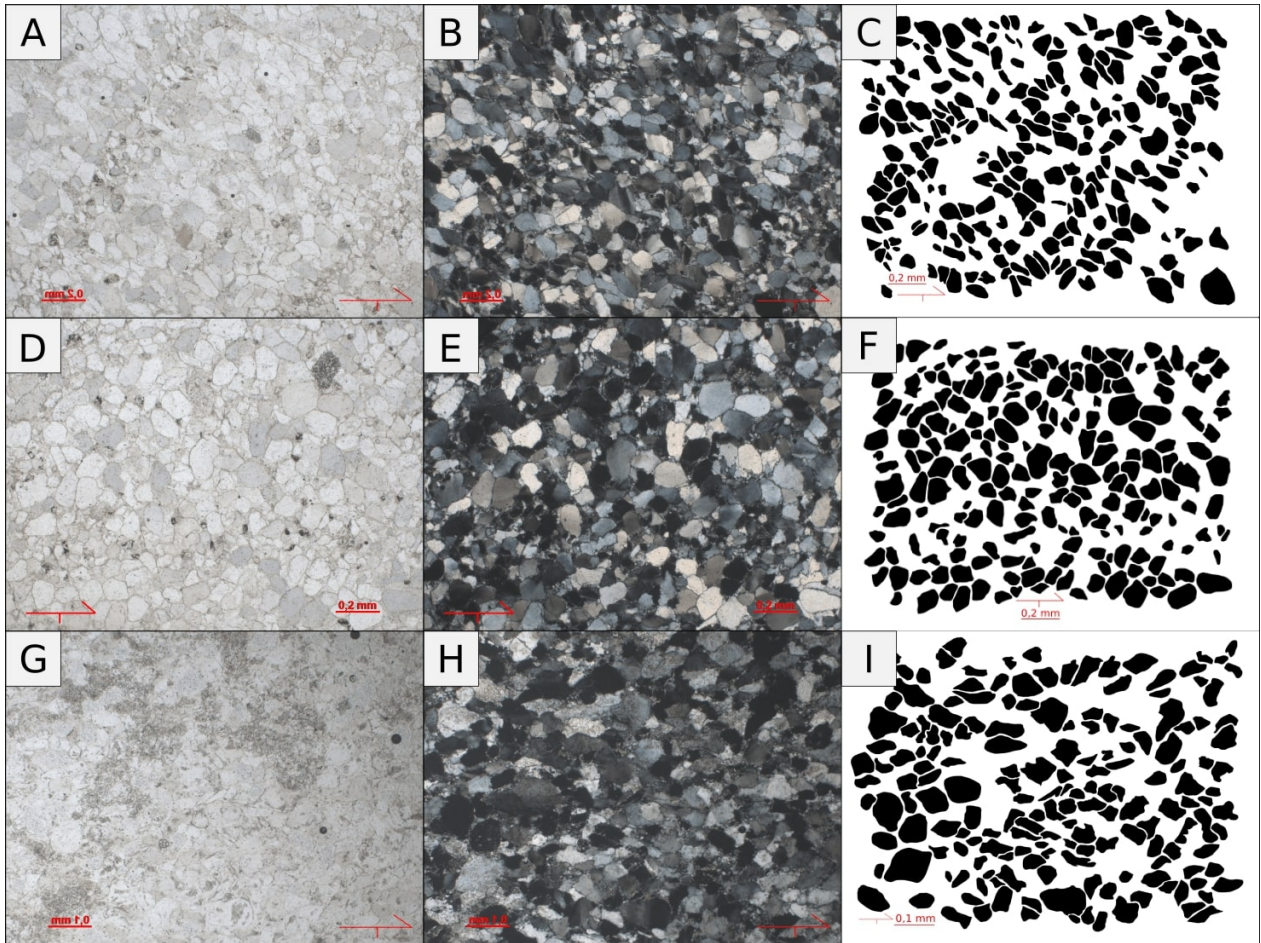
Figure 48: A,D,G: Polarized light microphotograph of the thin sections of planes AC, AB and BC of sample CD-06A, respectively. **B, E, H:** Cross-Polarized light microphotograph of the thin sections of planes AC, AB and BC from sample CD-06A, respectively. **C, F, I:** Single quartz grain digitized for SPO analysis of planes AC, AB and BC from sample CD-06A.

The CD-06A sample is a poorly sorted impure metarenite, from the Ouricuri do Ouro, with sub-angular to sub-round quartz grains, oriented preferably, parallel to the preferred slaty cleavage. As well as CD-03A, sample CD-06A lies close to the contact between the Basement and the above mentioned Formation, marked by major thrust faults. Sections AC and BC have a moderate shape ratio ranging from 1.4 to 1.5, while section AB has a low *R*, equals to 1.02 Figure 49. Thin sections microphotographs used to calculate the SPO are displayed in Fig. 48. The parameters of the best-fit ellipsoid can be seen in Fig. 50.
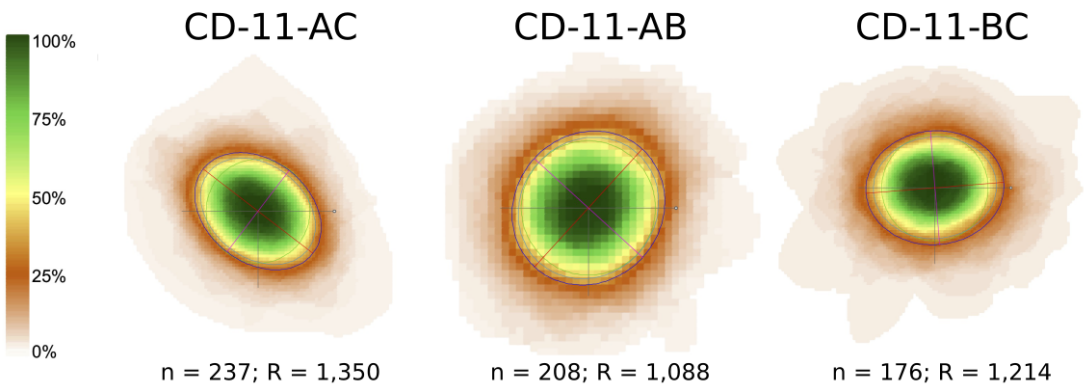
Figure 49: Shape preferred orientation ellipses of sample CD-06A.

CD-06A-AC   CD-06A-AB   CD-06A-BC

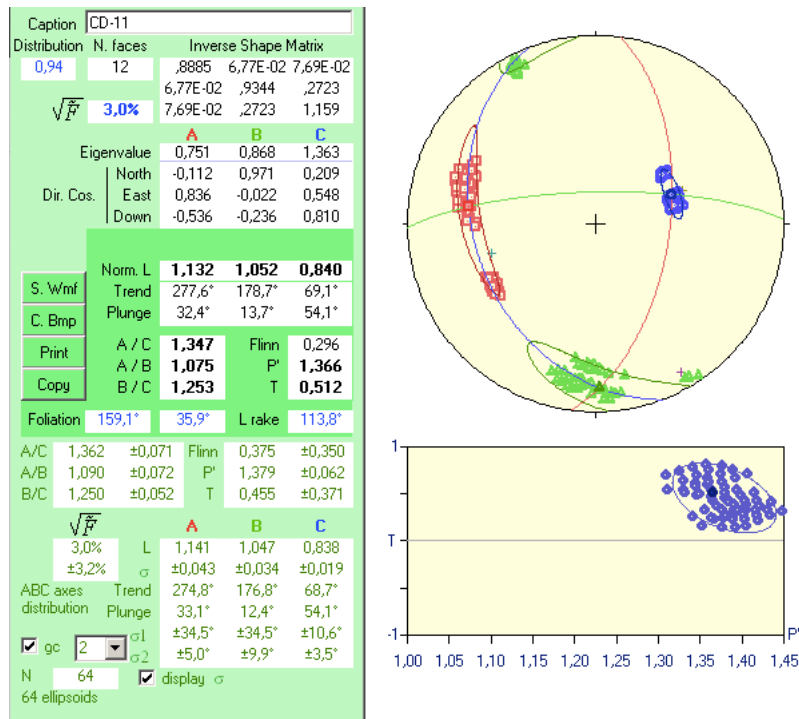n = 211; R = 1,408   n = 135; R = 1,022   n = 202; R = 1,492

**Figure 50:** Best-fit ellipsoid parameters from Sample CD-06A. Results direct from the program ELLIPSOID screen.

Figure 51: A,D,G: Polarized light microphotograph of the thin sections of planes AC, AB and BC of sample CD-11, respectively. **B, E, H:** Cross-Polarized light microphotograph of the thin sections of planes AC, AB and BC from sample CD-11, respectively. **C, F, I:** Single quartz grain digitized for SPO analysis of planes AC, AB and BC from sample CD-11.

The CD-11 sample is a well sorted metarenite, with sub-angular to sub-rounded quartz grains, from the Açuruá Formation. The sample is at the western limb of the Piatã Brachysincline, in the northern part of this major structure. Slaty cleavage is well marked and in section A, bedding is preserved and arranged perpendicularly to the cleavage. Sections AC and BC, present low to intermediate shape ratios, between 1.2 and 1.35, while section AB, presents a *R* close to 1.0 Figure 52. Thin sections microphotographs used to calculate the SPO are displayed in Fig. 51. The parameters of the best-fit ellipsoid can be seen in Fig. 53.
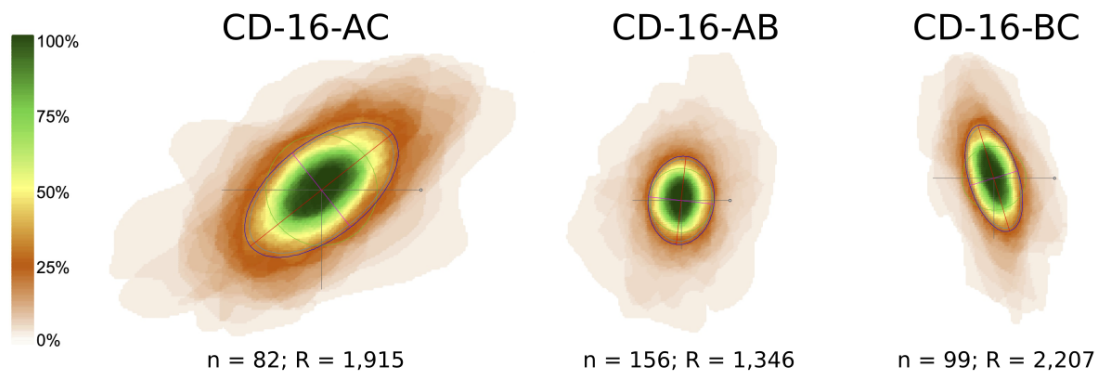
Figure 52: Shape preferred orientation ellipse of sample CD-11.

Figure 53: Best-fit ellipsoid parameters from Sample CD-11. Results direct from the program ELLIPSOID screen.
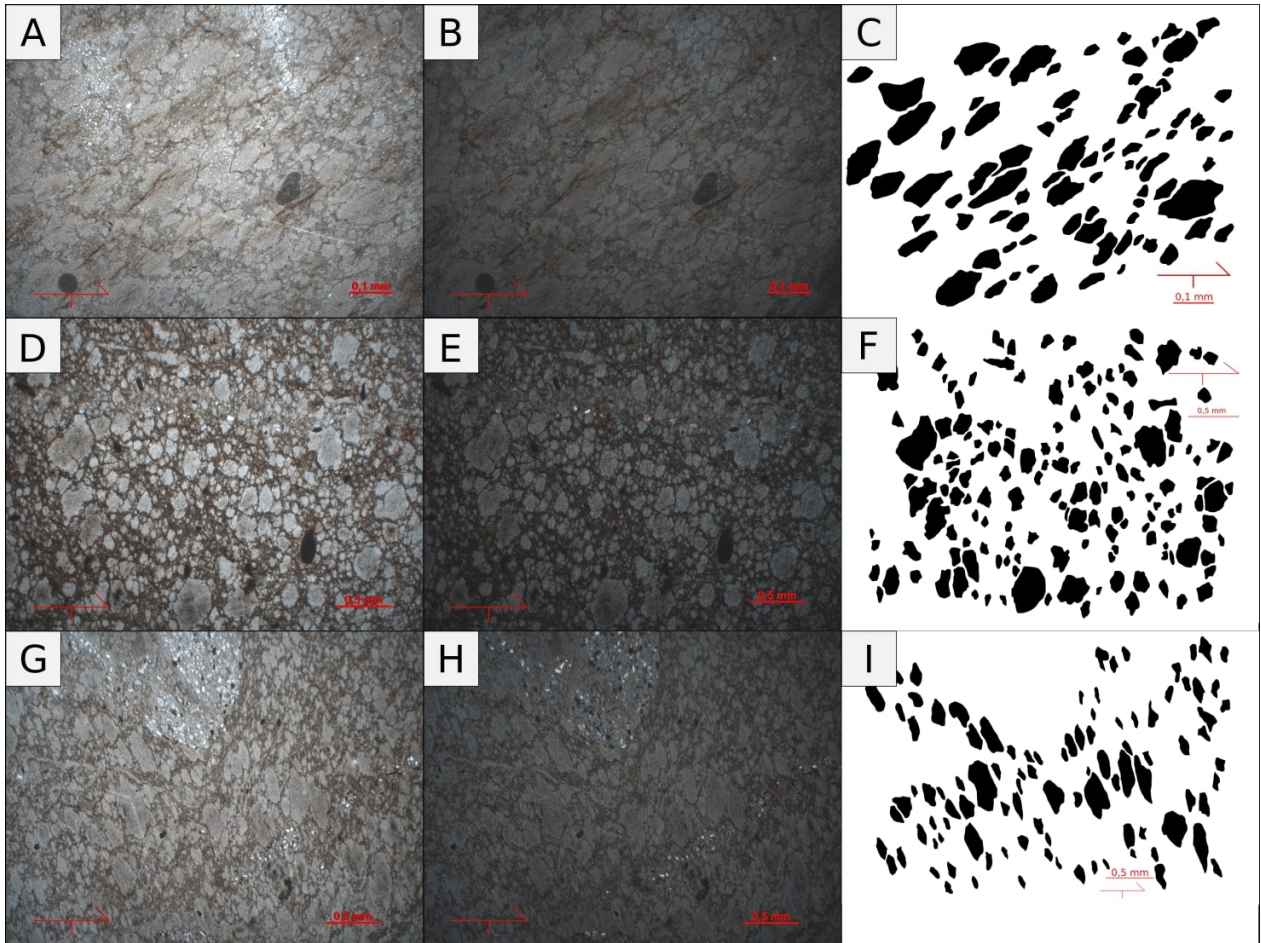
CD-16

Figure 54: A,D,G: Polarized light microphotograph of the thin sections of planes AC, AB and BC of sample CD-16, respectively. **B, E, H:** Cross-Polarized light microphotograph of the thin sections of planes AC, AB and BC from sample CD-16, respectively. **C, F, I:** Single quartz grain digitized for SPO analysis of planes AC, AB and BC from sample CD-16.

The CD-16 sample is a very fine metasiltite, with a very well-defined slaty cleavage, from the Ouricuri do Ouro Formation lyng close to the axial plane trace of an anticline. For this sample, mud pellets were used as strain markers and, therefore, the rock's competence must be taken into account when evaluating the calculated deformation intensity. Sections AB and BC have a very high strain ratio, ranging from 1.9–2.2, while AB has a moderate *R* equals to 1.346 Figure 55. Thin sections microphotographs used to calculate the SPO are displayed in Fig. 54. The parameters of the best-fit ellipsoid can be seen in Fig.56.

CD-16-AC

CD-16-AB

CD-16-BC

n = 82; R = 1,915

n = 156; R = 1,346

n = 99; R = 2,207

Figure 55: Shape preferred orientation ellipse of sample CD-16.
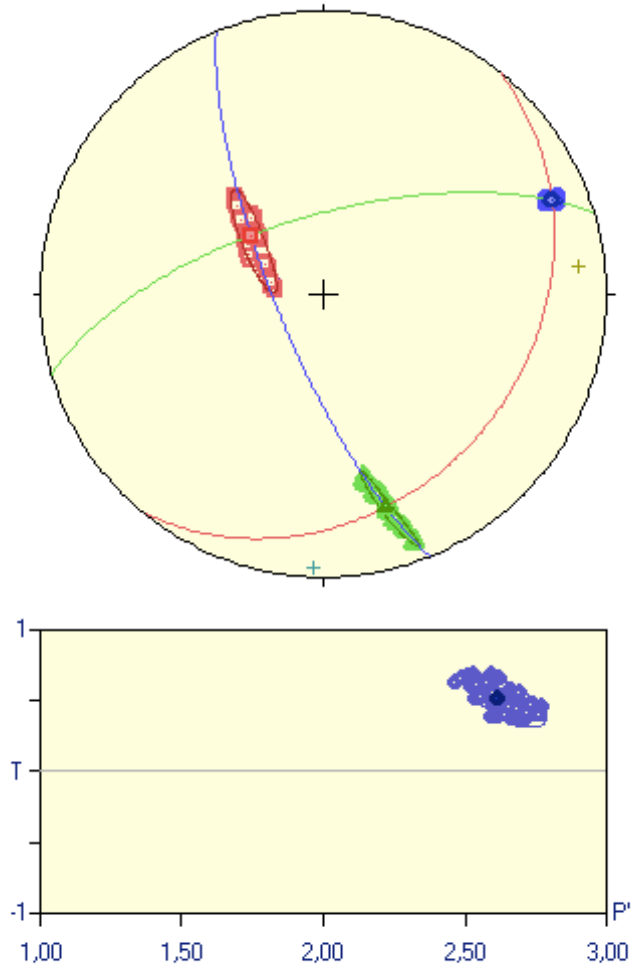

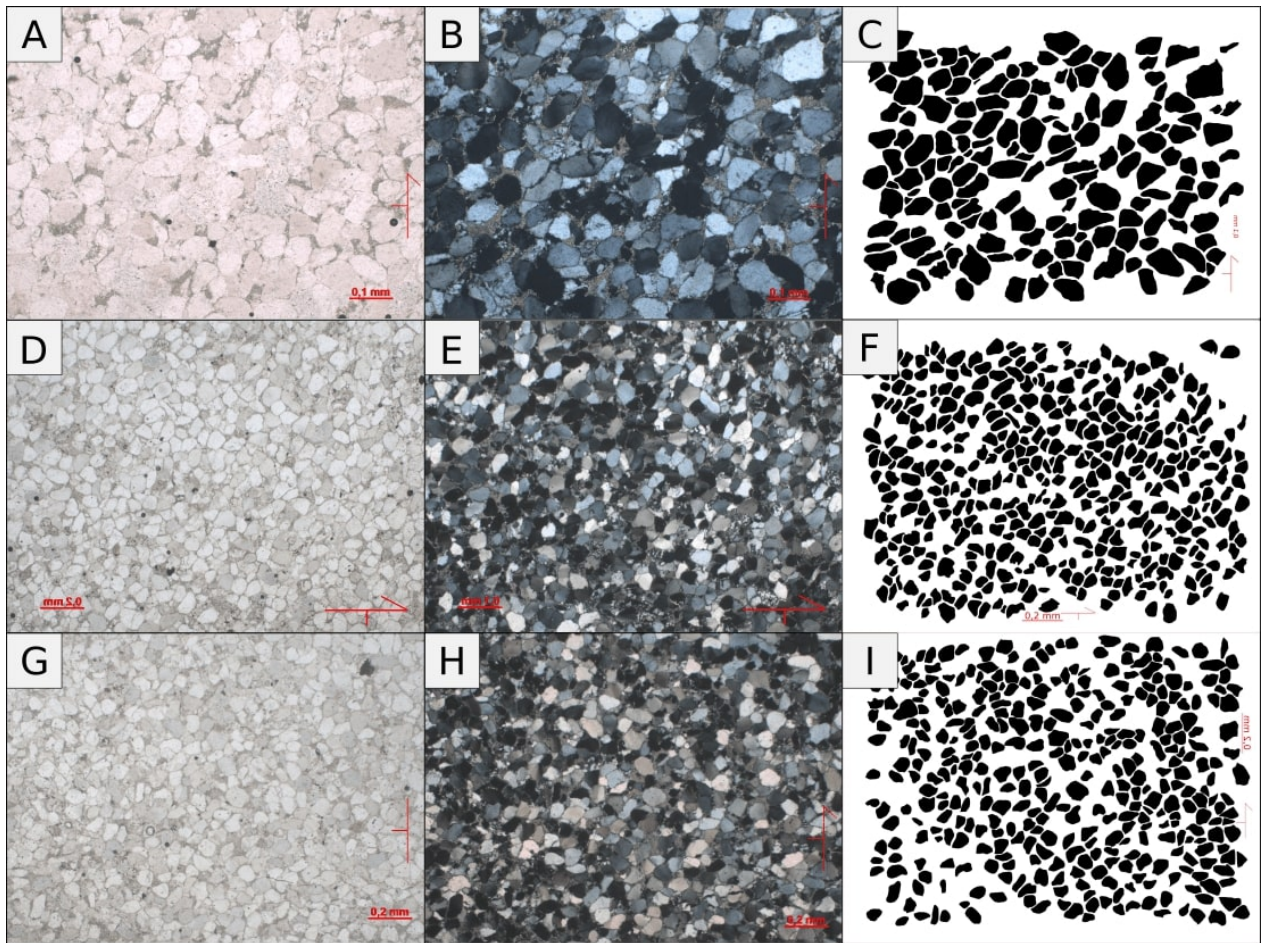**Figure 56:** Best-fit ellipsoid parameters from Sample CD-16. Results direct from the program ELLIPSOID screen.

Figure 57: A,D,G: Polarized light microphotograph of the thin sections of planes AC, AB and BC of sample CD-23, respectively. **B, E, H:** Cross-Polarized light microphotograph of the thin sections of planes AC, AB and BC from sample CD-23, respectively. **C, F, I:** Single quartz grain digitized for SPO analysis of planes AC, AB and BC from sample CD-23.

The CD-23 sample is a fine, well sorted metarenite, with sub-angular to sub-rounded single quartz grains, from the Açuruá Formation. It lies close to the axial plane trace of a major syncline in the central portion of the study area. For this sample, more than 900 grains were processed, and all sections yielded low shape ratios, ranging from 1.1 to 1.2 Figure 58. Thin sections microphotographs used to calculate the SPO are displayed in Fig. 57. The parameters of the best-fit ellipsoid can be seen in Fig. 59.
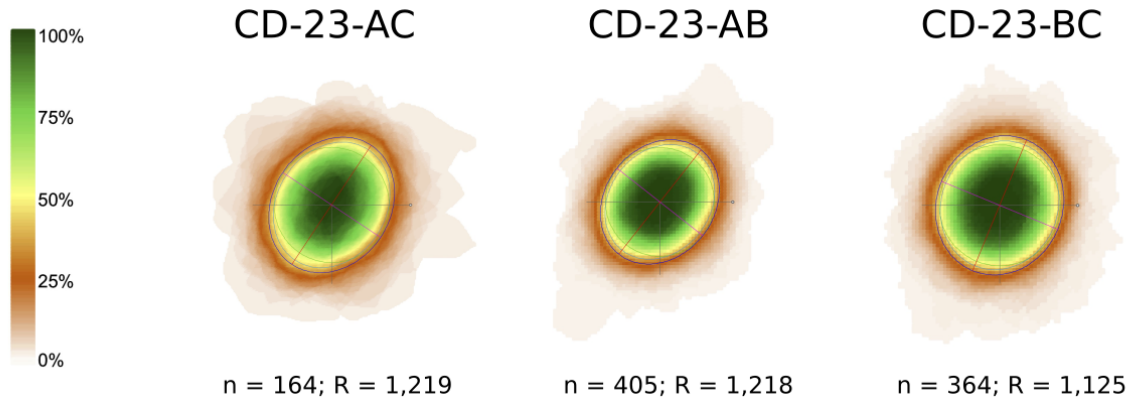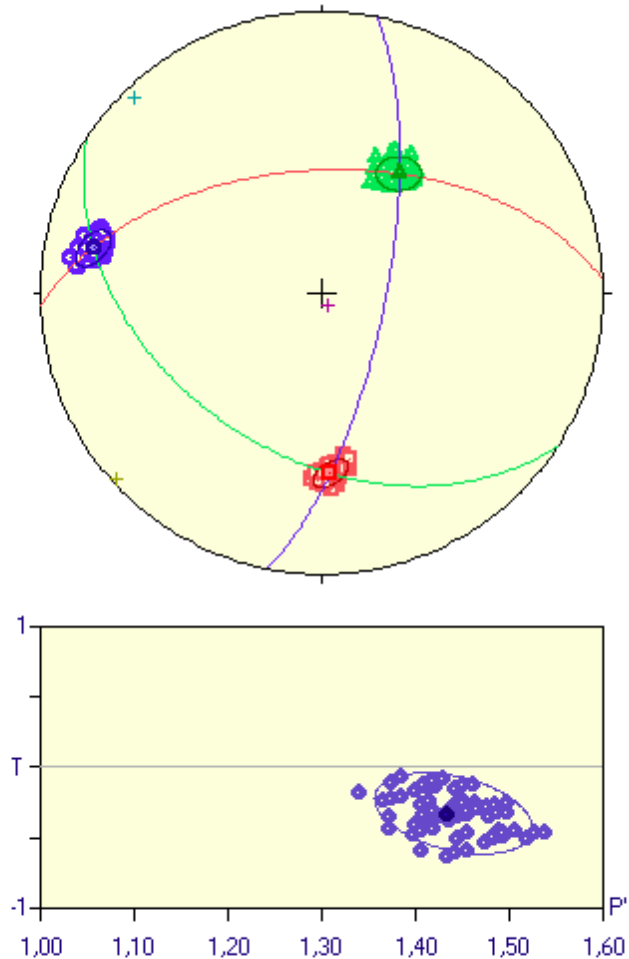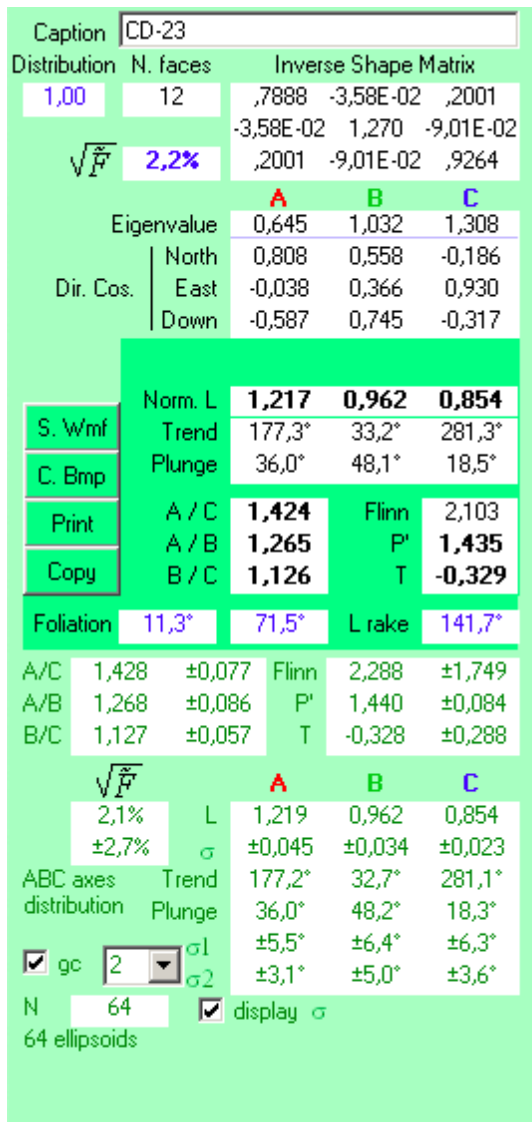
CD-23-AC   CD-23-AB   CD-23-BC

100%
75%
50%
25%
0%

n = 164; R = 1,219   n = 405; R = 1,218   n = 364; R = 1,125

Figure 58: Shape preferred orientation ellipse of sample CD-23.

Caption	CD-23		
Distribution	N. faces		Inverse Shape Matrix
1,00	12	,7888	-3,58E-02 ,2001
		-3,58E-02	1,270 -9,01E-02
$\sqrt{\tilde{F}}$ 2,2%		,2001	-9,01E-02 ,9264

		A	B	C
Eigenvalue		0,645	1,032	1,308
	North	0,808	0,558	-0,186
Dir. Cos.	East	-0,038	0,366	0,930
	Down	-0,587	0,745	-0,317

	Norm. L	1,217	0,962	0,854
S. Wmf	Trend	177,3°	33,2°	281,3°
C. Bmp	Plunge	36,0°	48,1°	18,5°
Print	A / C	1,424	Flinn	2,103
	A / B	1,265	P'	1,435
Copy	B / C	1,126	T	-0,329
Foliation	11,3°	71,5°	L rake	141,7°

A/C	1,428	±0,077	Flinn	2,288	±1,749
A/B	1,268	±0,086	P'	1,440	±0,084
B/C	1,127	±0,057	T	-0,328	±0,288

$\sqrt{\tilde{F}}$		A	B	C
2,1%	L	1,219	0,962	0,854
±2,7%	σ	±0,045	±0,034	±0,023
ABC axes	Trend	177,2°	32,7°	281,1°
distribution	Plunge	36,0°	48,2°	18,3°
	σ1	±5,5°	±6,4°	±6,3°
☑ gc 2 ▼	σ2	±3,1°	±5,0°	±3,6°
N 64	☑ display σ			
64 ellipsoids				

1
T
-1
1,00 1,10 1,20 1,30 1,40 1,50 1,60   P'

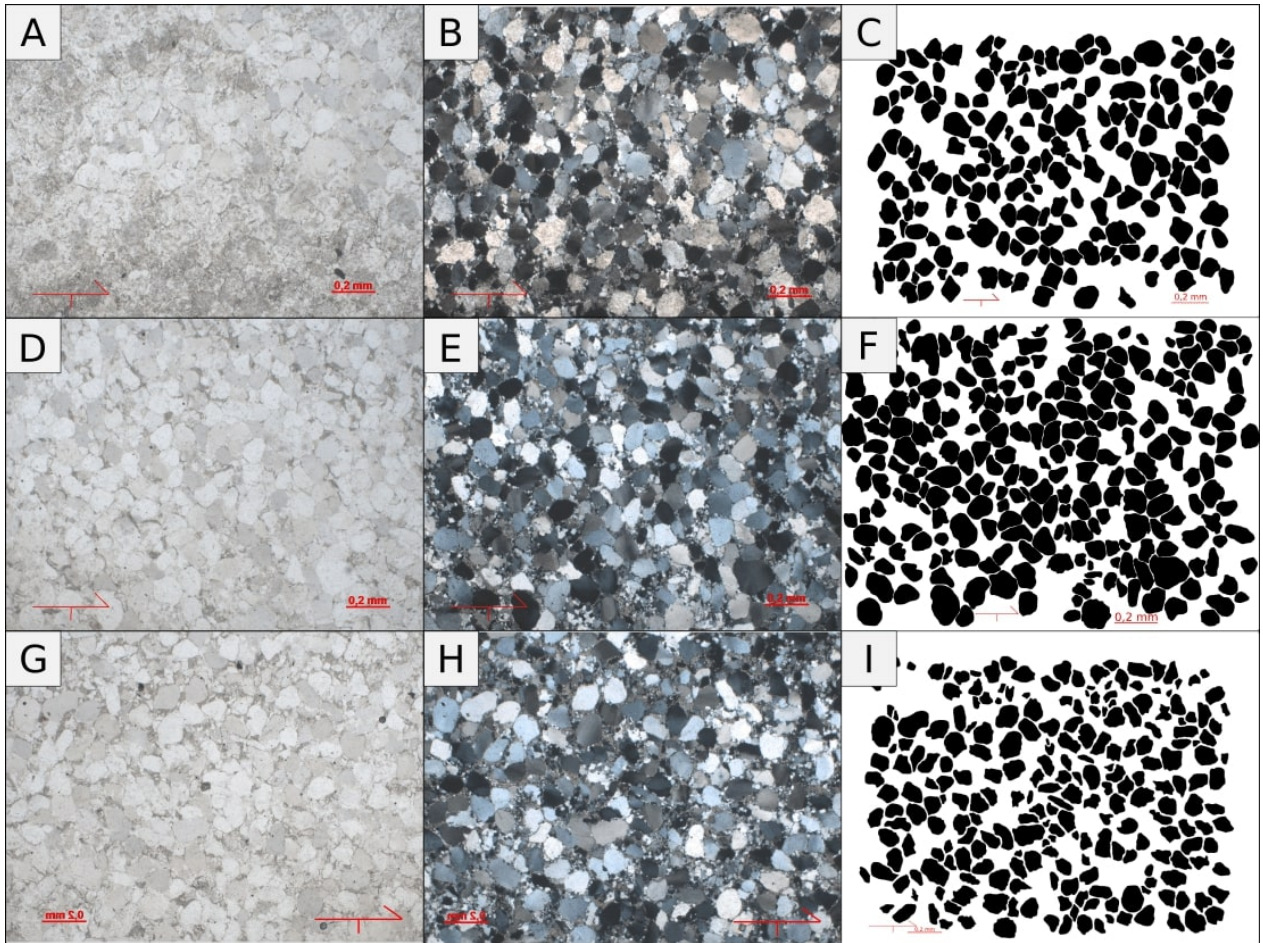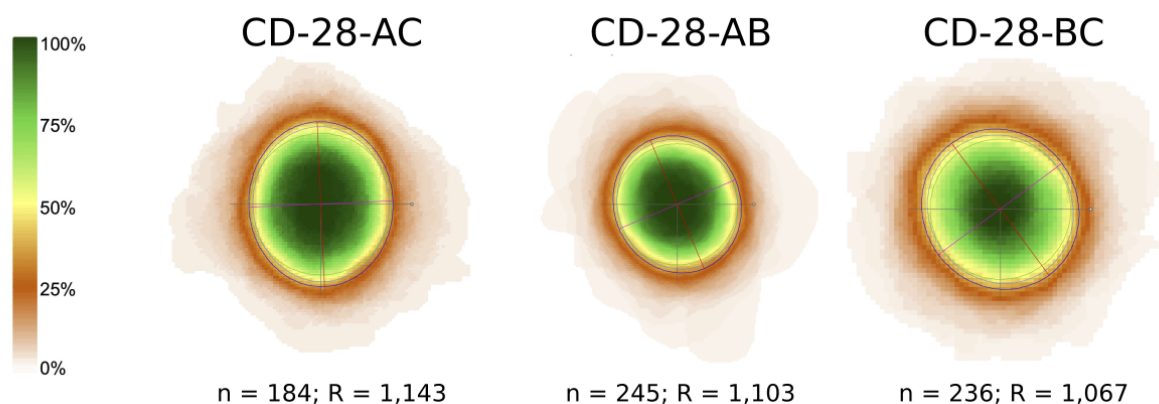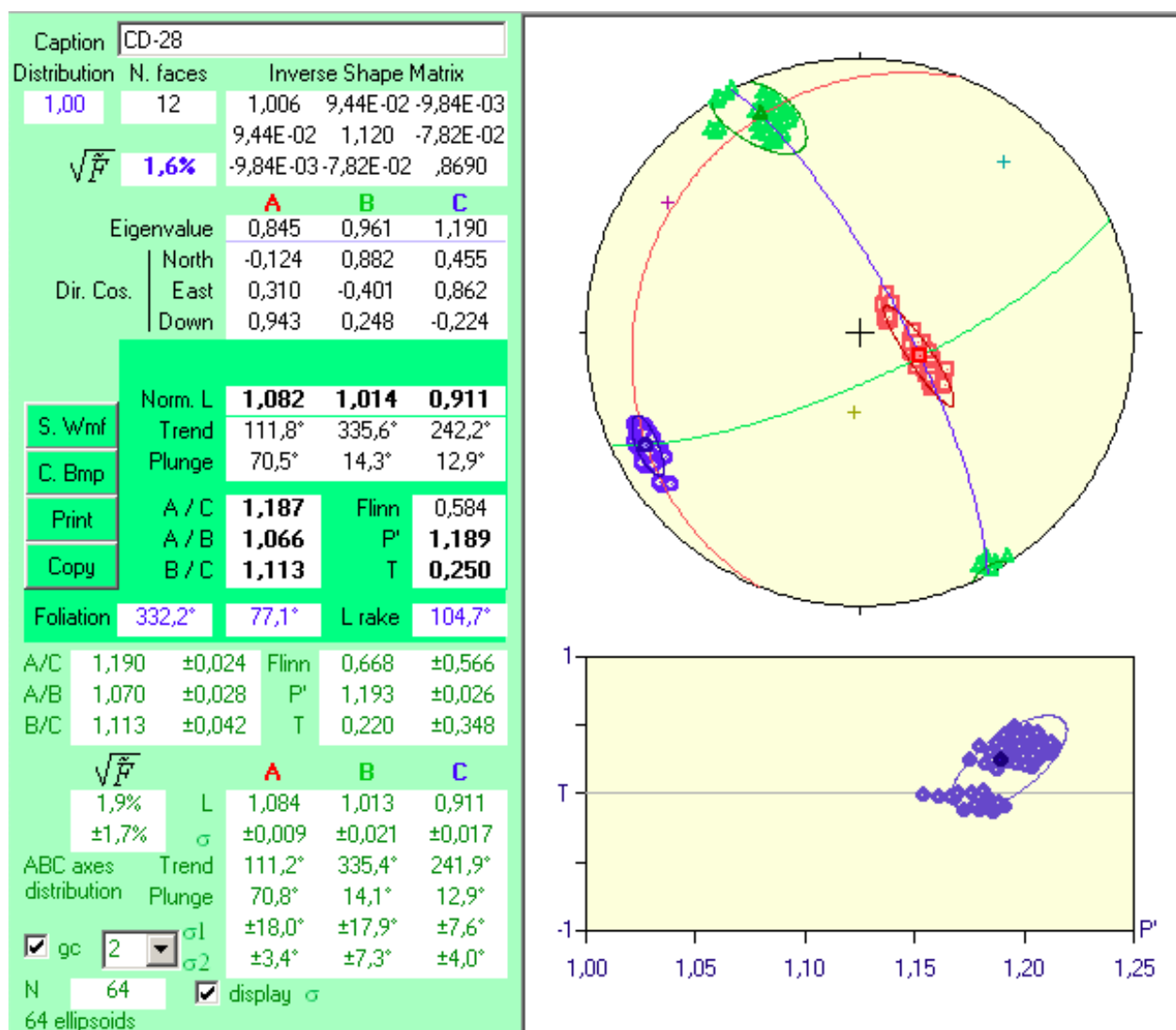**Figure 59:** Best-fit ellipsoid parameters from Sample CD-23. Results direct from the program ELLIPSOID screen.

Figure 60: A,D,G: Polarized light microphotograph of the thin sections of planes AC, AB and BC of sample CD-28, respectively. **B, E, H:** Cross-Polarized light microphotograph of the thin sections of planes AC, AB and BC from sample CD-28, respectively. **C, F, I:** Single quartz grain digitized for SPO analysis of planes AC, AB and BC from sample CD-28.

The CD-28 sample is a fine, well sorted, mature quartz-metarenite from the Açuruá Formation in the southwestern region of the study area. It lies at the eastern limb of the Érico Cardoso inverted brachysincline, close to the geological contact defined by a thrust fault, separating a minor anticline structure to east and the fold structure mentioned above. All the analyzed sections yielded low shape ratio ranging from 1.07 to 1.14 Figure 61. Thin sections microphotographs used to calculate the SPO are displayed in Fig. 60. The parameters of the best-fit ellipsoid can be seen in Fig.59.

Figure 61: Shape preferrred orientation ellipses of sample CD-28.

Figure 62: Best-fit ellipsoid parameters from Sample CD-28. Results direct from the program ELLIPSOID screen.
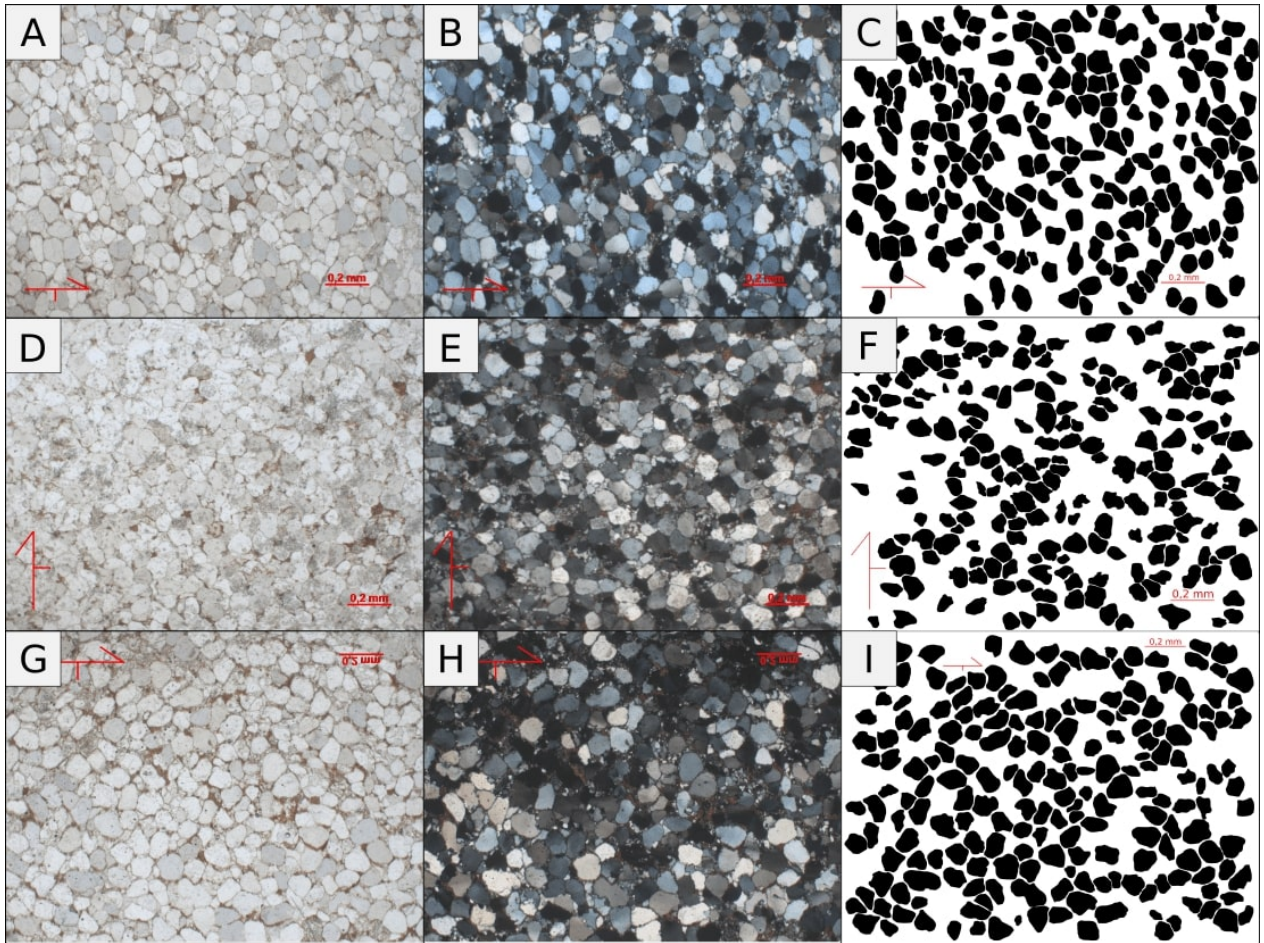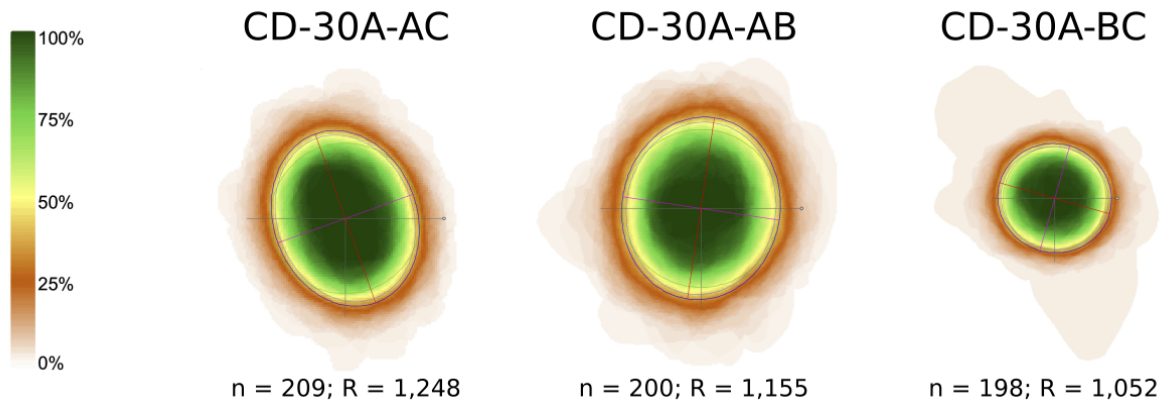
Figure 63: A,D,G: Polarized light microphotograph of the thin sections of planes AC, AB and BC of sample CD-30A, respectively. **B, E, H:** Cross-Polarized light microphotograph of the thin sections of planes AC, AB and BC from sample CD-30A, respectively. **C, F, I:** Single quartz grain digitized for SPO analysis of planes AC, AB and BC from sample CD-30A.

The CD-30A sample is a fine, well sorted quartz-metarenite from the Ouricuri do Ouro Formation. Just like CD-28, this sample lies close to a tectonic geological contact defined by a major thrust fault. More than 600 quartz grains were analyzed, with sections AB and BC showing low shape ratios values, between 1.05 and 1.15, while section AC presents an intermediate *R*, close to 1.25 Figure 64. Thin sections microphotographs used to calculate the SPO are displayed in Fig. 63. The parameters of the best-fit ellipsoid can be seen in Fig.65.

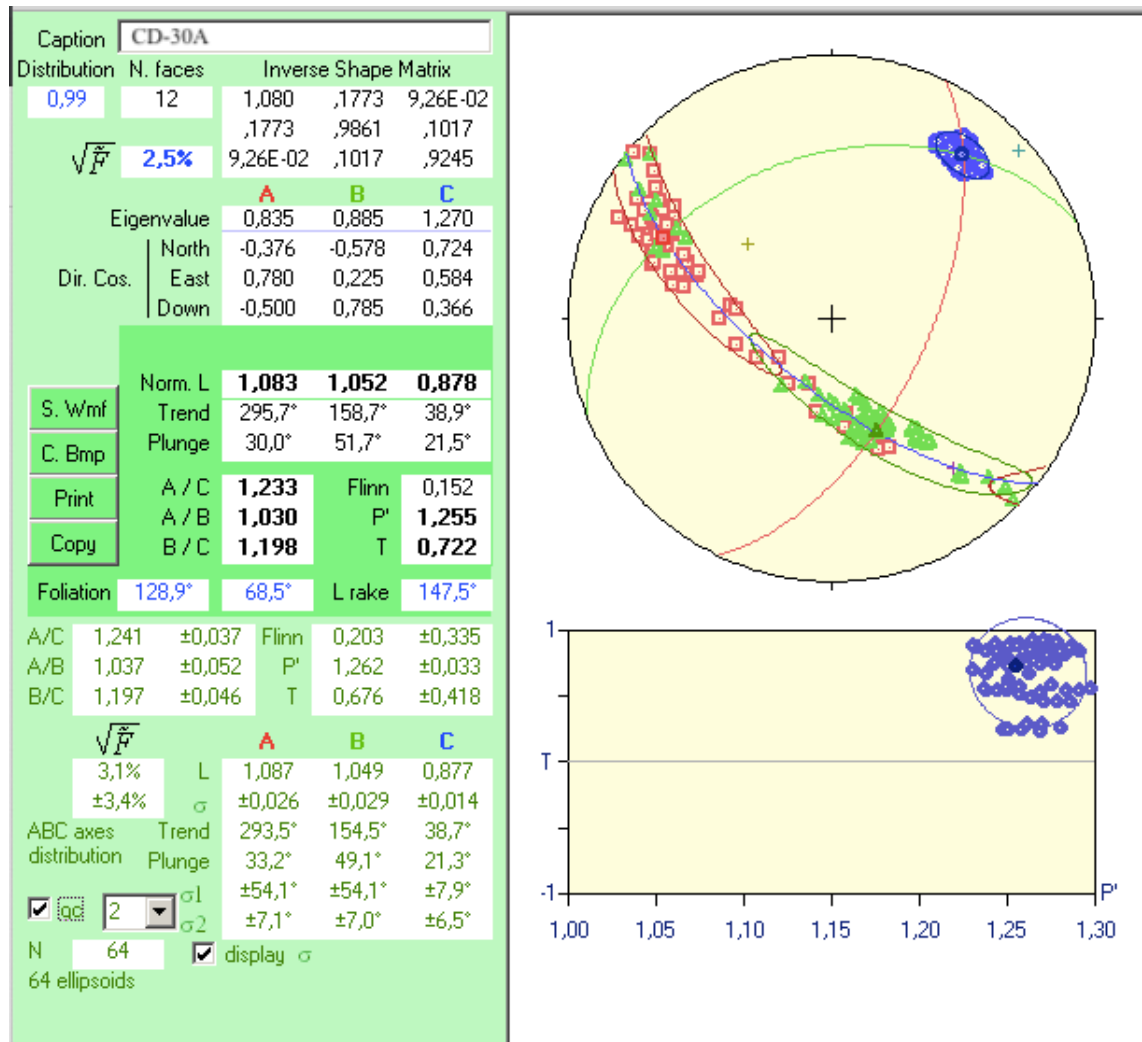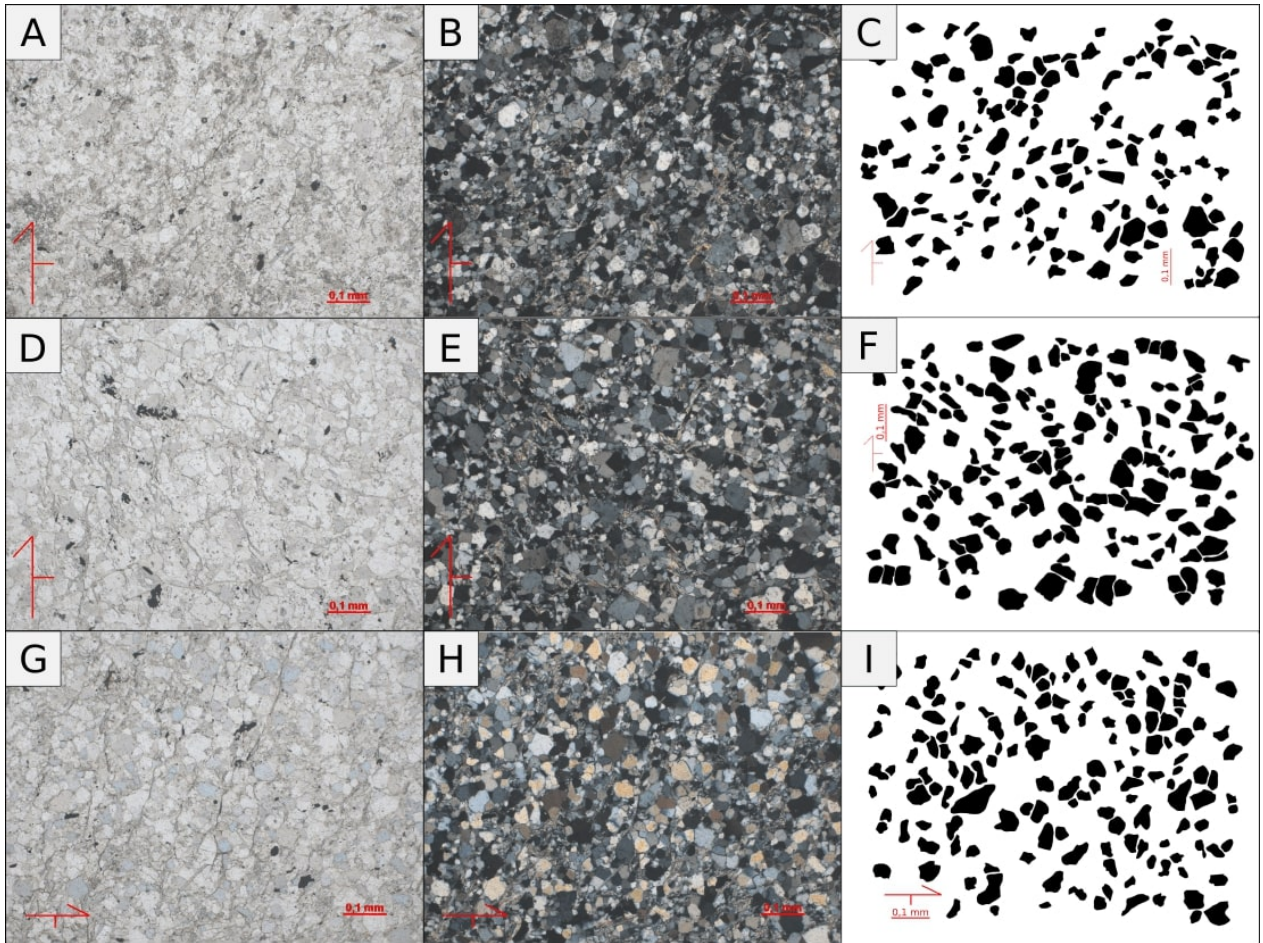**Figure 64:** Shape preferred orientation ellipses from sample CD-30A.

Figure 65: Best-fit ellipsoid parameters from Sample CD-30A. Results direct from the program ELLIPSOID screen.

Figure 66: A,D,G: Polarized light microphotograph of the thin sections of planes AC, AB and BC of sample CD-40, respectively. **B, E, H:** Cross-Polarized light microphotograph of the thin sections of planes AC, AB and BC from sample CD-40, respectively. **C, F, I:** Single quartz grain digitized for SPO analysis of planes AC, AB and BC from sample CD-40.

The CD-40 sample is a well-sorted metarenite, with lepid-granoblastic texture, from the Serra da Gameleira Formation, interpreted as pre-rift phase sedimentation. This sample lies near a major thrust fault system, which thrusts the basement units on top of the sedimentary cover in a northeastern direction. More than 500 grains of single quartz grains were analyzed, and all sections show low shape ratio values ranging from 1.11–1.14 Figure 67. Thin sections microphotographs used to calculate the SPO are displayed in Fig. 66. The parameters of the best-fit ellipsoid can be seen in Fig.65.
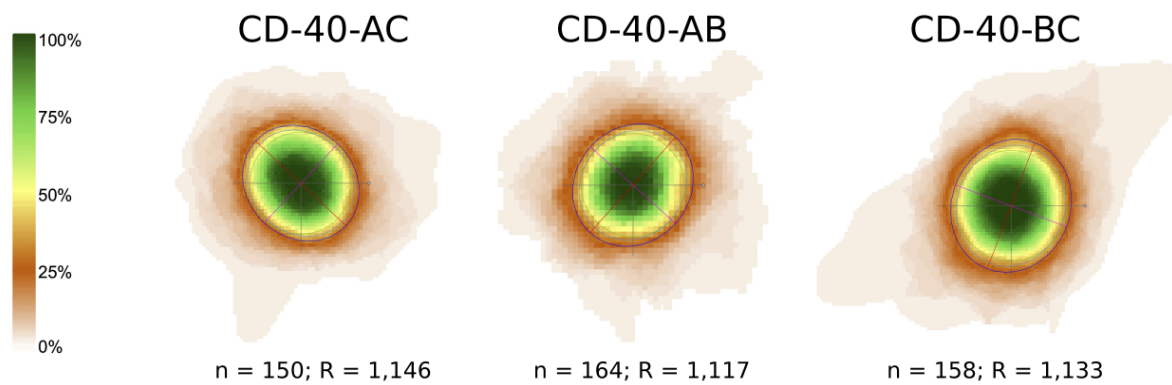
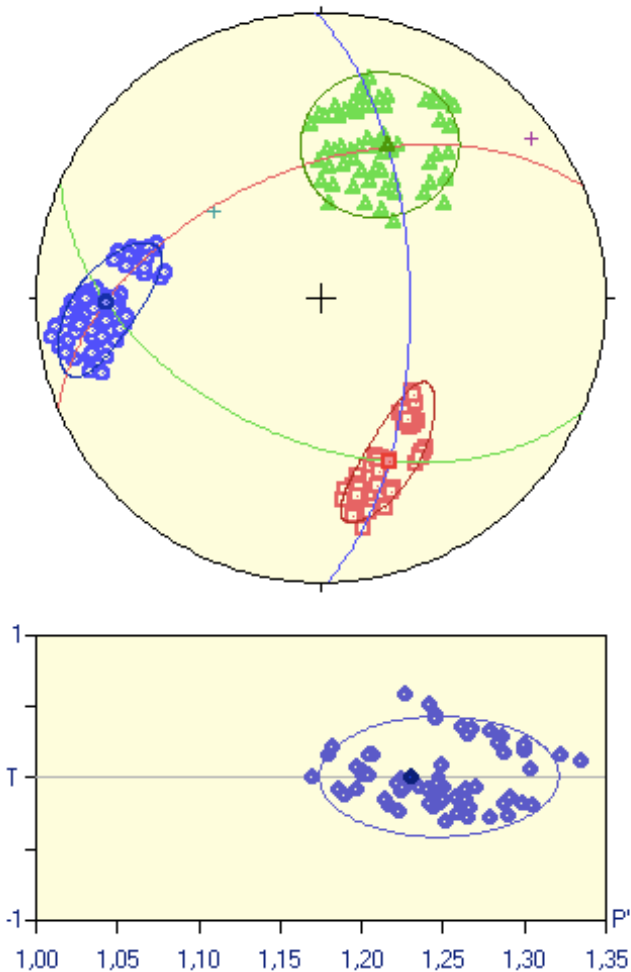**Figure 67:** Shape preferred orientation ellipses from sample CD-40.

Figure 68: Best-fit ellipsoid parameters from Sample CD-40. Results direct from the program ELLIPSOID screen.

8.5 *Sample field data - Western Chapada Diamantina*

This section presents field data from outcrops where the samples, regarding the Western Chapada Diamantina domain, used in this presented work were collected. All data is shown in Table 5.

Table 5: Attitude geological data from the sample outcrops. Both bedding and foliation are represented using the Right Hand Rule (RHR) convention, whereas lineation data follows the trend/plunge system.

Sample Code	Location		Map Unit	Lithology	Attitude Data		
	Longitude	Latitude			Sedimentary Bedding	Foliation	Intersect Lineation
CD-01B	41º 40' 09.2" S	13º 16' 11.7" W	Gavião Complex	Orthogneisse	-	352/85	-
CD-03A	41º 35' 33.3" S	13º 16' 11.7" W	Novo Horizonte Fm.	Meta-sandstone	-	355/80	-
CD-06A	41º 43' 05.1" S	13º 16' 36.0" W	Ouricuri do Ouro Fm.	Meta-sandstone	165/86	-	-
CD-11	41º 56' 12.5" S	13º 05' 21.6" W	Açuruá Fm.	Meta-sandstone	336/33	150/35	336/01
CD-16	42º 02' 13.4" S	13º 06' 54.6" W	Ouricuri do Ouro Fm.	Meta-siltstone	323/14	167/75	350/06
CD-23	42º 00' 58.9" S	13º 18' 41.4" W	Açuruá Fm.	Meta-sandstone	019/25	118/86	127/20
CD-28	42º 03' 37.5" S	13º 25' 30.8" W	Açuruá Fm.	Meta-sandstone	148/20	338/67	150/05
CD-30A	42º 03' 28.3" S	13º 25' 15.6" W	Ouricuri do Ouro Fm.	Meta-sandstone	308/25	149/75	321/07
CD-40	42º 12' 55.5" S	13º 26' 13.7" W	Serra da Gameleira Fm.	Meta-sandstone	-	-	-